Comprehensive evaluations of diurnal NO_2 measurements during DISCOVER-AQ 2011: Effects of resolution dependent representation of NO_x emissions

Jianfeng Li[1, a], Yuhang Wang[1*], Ruixiong Zhang[1], Charles Smeltzer[1], Andrew Weinheimer[2], Jay Herman[3], K. Folkert Boersma[4, 5], Edward A. Celarier[6, 7, b], Russell W. Long[8], James J. Szykman[8], Ruben Delgado[3], Anne M. Thompson[6], Travis N. Knepp[9, 10], Lok N. Lamsal[6], Scott J. Janz[6], Matthew G. Kowalewski[6], Xiong Liu[11], Caroline R. Nowlan[11]

[1]School of Earth and Atmospheric Sciences, Georgia Institute of Technology, Atlanta, Georgia, USA
[2]National Center for Atmospheric Research, Boulder, Colorado, USA
[3]University of Maryland Baltimore County JCET, Baltimore, Maryland, USA
[4]Royal Netherlands Meteorological Institute, De Bilt, the Netherlands
[5]Wageningen University, Meteorology and Air Quality Group, Wageningen, the Netherlands
[6]NASA Goddard Space Flight Center, Greenbelt, Maryland, USA
[7]Universities Space Research Association, Columbia, Maryland, USA
[8]National Exposure Research Laboratory, Office of Research and Development, U.S. Environmental Protection Agency, Research Triangle Park, NC, USA
[9]NASA Langley Research Center, Virginia, USA
[10]Science Systems and Applications, Inc., Hampton, Virginia, USA
[11]Harvard-Smithsonian Center for Astrophysics, Cambridge, Massachusetts, USA

[a]now at: Atmospheric Sciences and Global Change Division, Pacific Northwest National Laboratory, Richland, Washington, USA
[b]now at: Digital Spec, Tyson's Corner, VA, USA

[*] *Correspondence to* Yuhang Wang (yuhang.wang@eas.gatech.edu)

Abstract

Nitrogen oxides (NO_x = NO + NO_2) play a crucial role in the formation of ozone and secondary inorganic and organic aerosols, thus affecting human health, global radiation budget, and climate. The diurnal and spatial variations of NO_2 are functions of emissions, advection, deposition, vertical mixing, and chemistry. Their observations, therefore, provide useful constraints in our understanding of these factors. We employ a Regional chEmical and trAnsport model (REAM) to analyze the observed temporal (diurnal cycles) and spatial distributions of NO_2 concentrations and tropospheric vertical column densities (TVCDs) using aircraft in situ measurements, surface EPA Air Quality System (AQS) observations, as well as the measurements of TVCDs by satellite instruments (OMI: the Ozone Monitoring Instrument; and GOME-2A: Global Ozone Monitoring Experiment – 2A), ground-based Pandora, and the Airborne Compact Atmospheric Mapper (ACAM) instrument, in July 2011 during the DISCOVER-AQ campaign over the Baltimore-Washington region. The model simulations at 36- and 4-km resolutions are in reasonably good agreement with the regional mean temporospatial NO_2 observations in the daytime. However, we find significant overestimations (underestimations) of model simulated NO_2 (O_3) surface concentrations during nighttime, which can be mitigated by enhancing nocturnal vertical mixing in the model ~~needs to be enhanced to reproduce the observed NO_2 diurnal cycle in the model~~. Another discrepancy is that Pandora measured NO_2 TVCDs show much less variation in the late afternoon than simulated in the model. The higher resolution 4-km simulations tend to show larger biases compared to the observations due largely to the larger spatial variations of NO_x emissions in the model when the model spatial resolution is increased from 36 to 4 km. OMI, GOME-2A, and the high-resolution aircraft ACAM observations show a more dispersed distribution of NO_2 vertical column densities (VCDs) and lower VCDs in urban regions than corresponding 36- and 4-km model simulations, reflecting likely the spatial distribution bias of NO_x emissions in the National Emissions Inventory (NEI) 2011.

1 Introduction

Nitrogen oxides (NO_x = NO + NO_2) are among the most important trace gases in the atmosphere due to their crucial role in the formation of ozone (O_3), secondary aerosols, and their role in the chemical transformation of other atmospheric species, such as carbon monoxide (CO) and volatile organic compounds (VOCs) (Cheng et al., 2017; Cheng et al., 2018; Fisher et al., 2016; Li et al., 2019; Liu et al., 2012; Ng et al., 2017; Peng et al., 2016; Zhang and Wang, 2016). NO_x is emitted by both anthropogenic activities and natural sources. Anthropogenic sources account for about 77% of the global NO_x emissions, and fossil fuel combustion and industrial processes are the primary anthropogenic sources, which contribute to about 75% of the anthropogenic emissions (Seinfeld and Pandis, 2016). Other important anthropogenic sources include agriculture and biomass and biofuel burning. Soils and lightning are two major natural sources. Most NO_x is emitted as NO, which is then oxidized to NO_2 by oxidants, such as O_3, the hydroperoxyl radical (HO_2), and organic peroxy radicals (RO_2).

The diurnal variations of NO_2 controlled by physical and chemical processes reflect the temporal patterns of these underlying controlling factors, such as NO_x emissions, chemistry, deposition, advection, diffusion, and convection. Therefore, the observations of NO_2 diurnal cycles can be used to evaluate our understanding of NO_x related emission, chemistry, and physical processes (Frey et al., 2013; Jones et al., 2000; Judd et al., 2018). For example, Brown et al. (2004) analyzed the diurnal patterns of surface NO, NO_2, NO_3, N_2O_5, HNO_3, OH, and O_3 concentrations along the East Coast of the United States (U.S.) during the New England Air Quality Study (NEAQS) campaign in the summer of 2002 and found that the predominant nighttime sink of NO_x through the hydrolysis of N_2O_5 had an efficiency on par with daytime photochemical loss over the ocean surface off the New England coast. Van Stratum et al. (2012) investigated the contribution of boundary layer dynamics to chemistry evolution during the DOMINO (Diel Oxidant Mechanisms in relation to Nitrogen Oxides) campaign in 2008 in Spain and found that entrainment and boundary layer growth in daytime influenced mixed-layer NO and NO_2

diurnal cycles on the same order of chemical transformations. David and Nair (2011) found that the diurnal patterns of surface NO, NO_2, and O_3 concentrations at a tropical coastal station in India from November 2007 to May 2009 were closely associated with sea breeze and land breeze which affected the availability of NO_x through transport. They also thought that monsoon-associated synoptic wind patterns could strongly influence the magnitudes of NO, NO_2, and O_3 diurnal cycles. The monsoon effect on surface NO, NO_2, and O_3 diurnal cycles was also observed in China by Tu et al. (2007) on the basis of continuous measurements of NO, NO_2, and O_3 at an urban site in Nanjing from January 2000 – February 2003.

In addition to surface NO_2 diurnal cycles, the daily variations of NO_2 vertical column densities (VCDs) were also investigated in previous studies. For example, Boersma et al. (2008) compared NO_2 tropospheric VCDs (TVCDs) retrieved from OMI (the Ozone Monitoring Instrument) and SCIAMACHY (SCanning Imaging Absorption SpectroMeter for Atmospheric CHartography) in August 2006 around the world. They found that the diurnal patterns of different types of NO_x emissions could strongly affect the NO_2 TVCD variations between OMI and SCIAMACHY and that intense afternoon fire activity resulted in an increase of NO_2 TVCDs from 10:00 LT (local time) to 13:30 LT over tropical biomass burning regions. Boersma et al. (2009) further investigated the NO_2 TVCD change from SCIAMACHY to OMI in different seasons of 2006 in Israeli cities and found that there was a slight increase of NO_2 TVCDs from SCIAMACHY to OMI in winter due to increased NO_x emissions from 10:00 LT to 13:30 LT and a sufficiently weak photochemical sink and that the TVCDs from OMI were lower than SCIAMACHY in summer due to a strong photochemical sink of NO_x.

All these above researches, however, exploited only NO_2 surface or satellite VCD measurements. Due to the availability of ground-based NO_2 VCD observations, some recent studies tried to investigate the diurnal relationships between NO_2 surface concentrations and NO_2 VCDs (Kollonige et al., 2018; Thompson et al., 2019). For example, Zhao et al. (2019) converted Pandora direct-sun and zenith-sky NO_2 VCDs to NO_2 surface

92 concentrations using concentration-to-partial-column ratios and found that the derived concentrations well
93 captured the observed NO_2 surface diurnal and seasonal variations. Knepp et al. (2015) related the daytime
94 variations of NO_2 TVCD measurements by ground-based Pandora instruments to the variations of coincident NO_2
95 surface concentrations using a planetary boundary layer height (PBLH) factor over the periods July 2011 –
96 October 2011 at the NASA Langley Research Center in Hampton, Virginia and July 2011 at Padonia and
97 Edgewood sites in Maryland for the DISCOVER-AQ experiment, showing the importance of boundary-layer
98 vertical mixing on NO_2 vertical distributions and the ability of NO_2 VCD measurements to infer hourly
99 boundary-layer NO_2 variations. DISCOVER-AQ, the Deriving Information on Surface conditions from Column
100 and Vertically Resolved Observations Relevant to Air Quality experiment (https://discover-aq.larc.nasa.gov/, last
101 access: April 6, 2019), was designed to better understand the relationship between boundary-layer pollutants and
102 satellite observations (Flynn et al., 2014; Reed et al., 2015). Figure 1 shows the sampling locations of the summer
103 DISCOVER-AQ 2011 campaign in the Baltimore-Washington metropolitan region. In this campaign, the NASA
104 P-3B aircraft flew spirals over six air quality monitoring sites (Aldino - rural/suburban, Edgewood -
105 coastal/urban, Beltsville - suburban, Essex - coastal/urban, Fairhill - rural, and Padonia - suburban) (Table S1)
106 and the Chesapeake Bay (Cheng et al., 2017; Lamsal et al., 2014), and measured 245 NO_2 profiles in 14 flight
107 days in July (Zhang et al., 2016). During the same period, the NASA UC-12 aircraft flew across the Baltimore-
108 Washington region at an altitude about 8 km above sea level (ASL), using the Airborne Compact Atmospheric
109 Mapper (ACAM) to map the distributions of NO_2 VCDs below the aircraft (Lamsal et al., 2017). Furthermore,
110 ground-based instruments were deployed to measure NO_2 surface concentrations, NO_2 VCDs, and other physical
111 properties of the atmosphere (Anderson et al., 2014; Reed et al., 2015; Sawamura et al., 2014). Satellite OMI and
112 GOME-2A (Global Ozone Monitoring Experiment – 2A) instruments provided NO_2 TVCD measurements over
113 the campaign region at 13:30 and 9:30 LT, respectively. These concurrent measurements of NO_2 VCDs, surface
114 NO_2, and vertically resolved distributions of NO_2 during the DISCOVER-AQ 2011 campaign, therefore, provide

a comprehensive dataset to evaluate NO_2 diurnal and spatial variabilities and processes affecting NO_2 concentrations.

Section 2 describes the measurement datasets in detail. The Regional chEmistry and trAnsport Model (REAM), also described in section 2, is applied to simulate the NO_2 observations during the DISCOVER-AQ campaign in July 2011. The evaluations of the simulated diurnal cycles of surface NO_2 concentrations, NO_2 vertical profiles, and NO_2 TVCDs are discussed in section 3 through comparisons with observations. In section 3, we also investigate the differences between NO_2 diurnal cycles on weekdays and weekends and their implications for NO_x emission characteristics. To corroborate our evaluation of NO_x emissions based on NO_2 diurnal cycles, we further compare observed NO_y (reactive nitrogen compounds) concentrations with REAM simulation results in section 3. Moreover, we assess the resolution dependence of REAM simulation results in light of the observations and discuss the potential distribution biases of NO_x emissions by comparing the 36- and 4-km REAM simulation results with OMI, GOME-2A, and high-resolution ACAM NO_2 VCDs. Finally, we summarize the study in section 4.

2 Datasets and model description

2.1 REAM

REAM has been widely applied in many studies (Cheng et al., 2017; Choi et al., 2008; Li et al., 2019; Zhang et al., 2018; Zhang et al., 2016; Zhao et al., 2009). The model has a horizontal resolution of 36 km and 30 vertical layers in the troposphere. Meteorology fields are from a Weather Research and Forecasting (WRF, version 3.6) model simulation with a horizontal resolution of 36 km. We summarize the physics parameterization schemes of the WRF simulation in Table S2. The WRF simulation is initialized and constrained by the NCEP coupled forecast system model version 2 (CFSv2) products (http://rda.ucar.edu/datasets/ds094.0/, last access: March 10,

2015) (Saha et al., 2011). The chemistry mechanism in REAM is based on GEOS-Chem v11.01 with updated aerosol uptake of isoprene nitrates (Fisher et al., 2016) and revised treatment of wet scavenging processes (Luo et al., 2019). A 2° × 2.5° GEOS-Chem simulation provides the chemical boundary and initial conditions.

Biogenic VOC emissions in REAM are from MEGAN v2.10 (Guenther et al., 2012). Anthropogenic emissions on weekdays are from the National Emission Inventory 2011 (NEI2011) (EPA, 2014) from the Pacific Northwest National Laboratory (PNNL), which has an initial resolution of 4 km and is re-gridded to REAM 36-km grid cells (Figure 2). Weekday emission diurnal profiles are from NEI2011. The weekday to weekend emission ratios and weekend emission diurnal profiles are based on previous studies (Beirle et al., 2003; Boersma et al., 2009; Choi et al., 2012; de Foy, 2018; DenBleyker et al., 2012; Herman et al., 2009; Judd et al., 2018; Kaynak et al., 2009; Kim et al., 2016). These studies suggested that weekend NO_x emissions were 20% - 50% lower than weekday emissions, and the weekend NO_x emission diurnal cycles were different from weekdays; therefore, we specify a weekend to weekday NO_x emission ratio of 2/3 in this study. The resulting diurnal variations of weekday and weekend NO_x emissions over the DISCOVER-AQ 2011 region are shown in Figure 3. The diurnal emission variation is lower on weekends than on weekdays.

To understand the effects of model resolutions on the temporospatial distributions of NO_2, we also conduct a REAM simulation with a horizontal resolution of 4 km during the DISCOVER-AQ campaign. A 36-km REAM simulation (discussed in section 3.2) provides the chemical initial and hourly boundary conditions. Meteorology fields are from a nested WRF simulation (36 km, 12 km, 4 km) with cumulus parameterization turned off in the 4-km domain (Table S2). Figure 1 shows a comparison of the 4-km and 36-km REAM grid cells with DISCOVER-AQ observations, and Figure 2 shows a comparison of NO_x emission distributions between the 4-km and 36-km REAM simulations. The comparison of NO_x emission diurnal variations over the DISCOVER-AQ 2011 region between the 4-km and 36-km REAM is shown in Figure 3.

2.2 NO_2 TVCD measurements by OMI and GOME-2A

The OMI instrument onboard the sun-synchronous NASA EOS Aura satellite with an equator-crossing time of around 13:30 LT was developed by the Finnish Meteorological Institute and the Netherlands Agency for Aerospace Programs to measure solar backscattering radiation in the visible and ultraviolet bands (Levelt et al., 2006; Russell et al., 2012). The radiance measurements are used to derive trace gas concentrations in the atmosphere, such as O_3, NO_2, HCHO, and SO_2 (Levelt et al., 2006). OMI has a nadir resolution of 13 km × 24 km and provides daily global coverage (Levelt et al., 2006).

Two widely-used archives of OMI NO_2 VCD products are available, NASA OMNO2 (v4.0) (https://disc.gsfc.nasa.gov/datasets/OMNO2_003/summary, last access: September 26, 2020) and KNMI DOMINO (v2.0) (http://www.temis.nl/airpollution/no2.html, last access: January 14, 2015). Although both use Differential Optical Absorption Spectroscopy (DOAS) algorithms to derive NO_2 slant column densities, they have differences in spectral fitting, stratospheric and tropospheric NO_2 slant column density (SCD) separation, a priori NO_2 vertical profiles, and air mass factor (AMF) calculation, etc. (Boersma et al., 2011; Bucsela et al., 2013; Chance, 2002; Krotkov et al., 2017; Lamsal et al., ~~2020~~2021; Marchenko et al., 2015; Oetjen et al., 2013; van der A et al., 2010; Van Geffen et al., 2015). Both OMNO2 and DOMINO have been extensively evaluated with field measurements and models (Boersma et al., 2009; Boersma et al., 2011; Choi et al., 2020; Hains et al., 2010; Huijnen et al., 2010; Ionov et al., 2008; Irie et al., 2008; Lamsal et al., 2014; Lamsal et al., ~~2020~~2021; Oetjen et al., 2013). The estimated uncertainty of DOMINO TVCD product includes an absolute component of 1.0×10^{15} molecules cm^{-2} and a relative AMF component of 25% (Boersma et al., 2011), while the uncertainty of OMNO2 TVCD product ranges from ~30% under clear-sky conditions to ~60% under cloudy conditions (Lamsal et al., 2014; Oetjen et al., 2013; Tong et al., 2015). In order to reduce uncertainties in this study, we only use TVCD data with effective cloud fractions < 0.2, solar zenith angle (SZA) < 80°, and albedo ≤ 0.3. Both positive

and negative TVCDs are considered in the calculation. The data affected by row anomaly are excluded (Boersma et al., 2018; Zhang et al., 2018).

For AMF calculation, DOMINO used daily TM4 model results with a resolution of 3° × 2° as a priori NO_2 vertical profiles (Boersma et al., 2007; Boersma et al., 2011), while OMNO2 v4.0 used monthly mean values from the Global Modeling Initiative (GMI) model with a resolution of 1° × 1.25°. The relatively coarse horizontal resolution of the a priori NO_2 profiles in the retrievals can introduce uncertainties in the spatial and temporal characteristics of NO_2 TVCDs at satellite pixel scales. For comparison purposes, we also use 36-km REAM simulation results as the a priori NO_2 profiles to compute the AMFs and NO_2 TVCDs with the DOMINO algorithm. The 36-km REAM NO_2 data are first regridded to OMI pixels to calculate the corresponding tropospheric AMFs, which are then applied to compute OMI NO_2 TVCDs by dividing the tropospheric SCDs from the DOMINO product by our updated AMFs.

The GOME-2 instrument onboard the polar-orbiting MetOp-A satellite (now referred to as GOME-2A) is an improved version of GOME-1 launched in 1995 and has an overpass time of 9:30 LT and a spatial resolution of 80 × 40 km^2 (Munro et al., 2006; Peters et al., 2012). GOME-2A measures backscattered solar radiation in the range from 240 nm to 790 nm, which is used for VCD retrievals of trace gases, such as O_3, NO_2, BrO, and SO_2 (Munro et al., 2006). We use the KNMI TM4NO2A v2.3 GOME-2A NO_2 VCD product archived on http://www.temis.nl/airpollution/no2col/no2colgome2_v2.php (last access: January 22, 2015) (Boersma et al., 2007; Boersma et al., 2011). GOME-2A derived NO_2 VCDs have been validated with SCIAMACHY and MAX-DOAS measurements (Irie et al., 2012; Peters et al., 2012; Richter et al., 2011). As in the case of OMI, we use the same criteria to filter the NO_2 TVCD data and recalculate the tropospheric AMF values and GOME-2A TVCDs using the daily 36-km REAM NO_2 profiles (9:00 LT – 10:00 LT).

2.3 Pandora ground-based NO_2 VCD measurements

Pandora is a small direct sun spectrometer, which measures sun and sky radiance from 270 to 530 nm with a 0.5 nm resolution and a 1.6° field of view (FOV) for the retrieval of the total VCDs of NO_2 with a precision of about 5.4×10^{14} molecules/cm^2 (2.7×10^{14} molecules/cm^2 for NO_2 SCD) and a nominal accuracy of 2.7×10^{15} molecules cm^{-2} under clear-sky conditions (Herman et al., 2009; Lamsal et al., 2014; Zhao et al., 2020). There were 12 Pandora sites operating in the DISCOVER-AQ campaign (Figure 1). Six of them are the same as the P-3B aircraft spiral locations (Aldino, Edgewood, Beltsville, Essex, Fairhill, and Padonia) (Table S1 and Figure 1). The other six sites are Naval Academy (Annapolis Maryland) (USNA – ocean), University of Maryland College Park (UMCP – urban), University of Maryland Baltimore County (UMBC – urban), Smithsonian Environmental Research Center (SERC – rural/coastal), Oldtown in Baltimore (Oldtown – urban), and Goddard Space Flight Center (GSFC – urban/suburban) (Table S1 and Figure 1). In this study, we exclude the USNA site as its measurements were conducted on a ship ("Pandora(w)" in Figure 1), and there were no other surface observations in the corresponding REAM grid cell. Including the data from the USNA site has a negligible effect on the comparisons of observed and simulated NO_2 TVCDs. In our analysis, we ignore Pandora measurements with SZA > 80° (Figure S1) and exclude the data when fewer than three valid measurements are available within an hour to reduce the uncertainties of the hourly averages due to the significant variations of Pandora observations (Figure S2).

Since Pandora measures total NO_2 VCDs, we need to subtract stratosphere NO_2 VCDs from the total VCDs to compute TVCDs. As shown in Figure S3, stratosphere NO_2 VCDs show a clear diurnal cycle with an increase during daytime due in part to the photolysis of reactive nitrogen reservoirs such as N_2O_5 and HNO_3 (Brohede et al., 2007; Dirksen et al., 2011; Peters et al., 2012; Sen et al., 1998; Spinei et al., 2014), which is consistent with the significant increase of stratospheric NO_2 VCDs from GOME-2A to OMI. In this study, we use the GMI model simulated stratospheric NO_2 VCDs in Figure S3 to calculate the Pandora NO_2 TVCDs. The small

discrepancies between the GMI stratospheric NO_2 VCDs and satellite products do not change the pattern of Pandora NO_2 TVCD diurnal variations or affect the conclusions in this study.

2.4 ACAM NO_2 VCD measurements

The ACAM instrument onboard the UC-12 aircraft consists of two thermally spectrometers in the ultraviolet/visible/near-infrared range. The spectrometer in the ultraviolet/visible band (304 nm – 520 nm) with a resolution of 0.8 nm and a sampling of 0.105 nm can be used to detect NO_2 in the atmosphere. The native ground resolution of UC-12 ACAM NO_2 measurements is 0.5 km × 0.75 km at a flight altitude of about 8 km ASL and a nominal ground speed of 100 m s^{-1} during the DISCOVER-AQ 2011 campaign (Lamsal et al., 2017), thus providing high-resolution NO_2 VCDs below the aircraft.

In this study, we mainly use the ACAM NO_2 VCD product described by Lamsal et al. (2017), which applied a pair-average co-adding scheme to produce NO_2 VCDs at a ground resolution of about 1.5 km (cross-track) × 1.1 km (along-track) to reduce noise impacts. In their retrieval of ACAM NO_2 VCDs, they first used the DOAS fitting method to generate differential NO_2 SCDs relative to the SCDs at an unpolluted reference location. Then they computed above/below-aircraft AMFs at both sampling and reference locations based on the vector linearized discrete ordinate radiative transfer code (VLIDORT) (Spurr, 2008). In the computation of AMFs, the a priori NO_2 vertical profiles were from a combination of a high-resolution (4-km) CMAQ (the Community Multiscale Air Quality Modeling System) model outputs in the boundary layer and a GMI simulation (2° × 2.5°) results elsewhere in the atmosphere. Finally, the below-aircraft NO_2 VCDs at the sampling locations were generated by dividing below-aircraft NO_2 SCDs at the sampling locations by the corresponding below-aircraft AMFs. The below-aircraft NO_2 SCDs were the differences between the total and above-aircraft NO_2 SCDs. The total NO_2 SCDs were the sum of DOAS fitting generated differential NO_2 SCDs and NO_2 SCDs at the reference location, and the above-aircraft NO_2 SCDs were derived based on above-aircraft AMFs, GMI NO_2 profiles, and

246 OMNO2 stratospheric NO_2 VCDs (Lamsal et al., 2017). The ACAM NO_2 VCD product had been evaluated via
247 comparisons with other independent observations during the DISCOVER-AQ 2011 campaign, such as P-3B
248 aircraft, Pandora, and OMNO2, and the uncertainty of individual below-aircraft NO_2 VCD is about 30% (Lamsal
249 et al., 2017). To keep the consistency of ACAM NO_2 VCDs, we exclude NO_2 VCDs measured at altitudes < 8 km
250 ASL, which accounts for about 6.8% of the total available ACAM NO_2 VCD data. We regrid the 1.5 km × 1.1
251 km ACAM NO_2 VCDs to the 4-km REAM grid cells (Figure 1), which are then used to evaluate the distribution
252 of NO_2 VCDs in the 4-km REAM simulation. As a supplement in section 3.7, we also assess the 4-km REAM
253 simulation by using the UC-12 ACAM NO_2 VCDs produced by the Smithsonian Astrophysical Observatory
254 (SAO) algorithms, archived on https://www-air.larc.nasa.gov/cgi-bin/ArcView/discover-aq.dc-
255 2011?UC12=1#LIU.XIONG/ (last access: December 31, 2019) (Liu et al., 2015a; Liu et al., 2015b). This product
256 is an early version of the SAO algorithm used to produce the Geostationary Trace gas and Aerosol Sensor
257 Optimization (GeoTASO) and the GEOstationary Coastal and Air Pollution Events (GEO-CAPE) Airborne
258 Simulator (GCAS) airborne observations in later airborne campaigns (Nowlan et al., 2016; Nowlan et al., 2018).

259 2.5 Surface NO_2 and O_3 measurements

260 The measurement of NO_x is based on the chemiluminescence of electronically excited NO_2^*, produced from
261 the reaction of NO with O_3, and the strength of the chemiluminescence from the decay of NO_2^* to NO_2 is
262 proportional to the number of NO molecules present (Reed et al., 2016). NO_2 concentrations can be measured
263 with this method by converting NO_2 to NO first through catalytic reactions (typically on the surface of heated
264 molybdenum oxide (MoO_x) substrate) or photolytic processes (Lamsal et al., 2015; Reed et al., 2016). However,
265 for the catalytic method, reactive nitrogen compounds other than NO_x (NO_z), such as HNO_3, peroxyacetyl nitrate
266 (PAN), and other organic nitrates, can also be reduced to NO on the heated surface, thus causing an
267 overestimation of NO_2. The magnitude of the overestimation depends on the concentrations and the reduction

efficiencies of interference species, both of which are uncertain. The photolytic approach, which employs broadband photolysis of ambient NO_2, offers more accurate NO_2 measurements (Lamsal et al., 2015).

There were 11 NO_x monitoring sites operating in the DISCOVER-AQ region during the campaign (Figure 1), including those from the EPA Air Quality System (AQS) monitoring network and those deployed for the DISCOVER-AQ campaign. Nine of them measured NO_2 concentrations by a catalytic converter. The other two sites (Edgewood and Padonia) had NO_2 measurements from both catalytic and photolytic methods. Different stationary catalytic instruments were used during the campaign: Thermo Electron 42C-Y NO_y analyzer, Thermo Model 42C NO_x analyzer, Thermo Model 42I-Y NO_y analyzer, and Ecotech Model 9843/9841 T-NO_y analyzers. In addition, a mobile platform — NATIVE (Nittany Atmospheric Trailer and Integrated Validation Experiment) with a Thermo Electron 42C-Y NO_y analyzer installed, was also deployed in the Edgewood site. The photolytic measurements of NO_2 in Edgewood and Padonia were from Teledyne API model 200eup photolytic NO_x analyzers. We scale catalytic NO_2 measurements using the diurnal ratios of NO_2 photolytic measurements to NO_2 from the corresponding catalytic analyzers (Figure 4). Figure 4 shows the lowest photolytic/catalytic ratios in the afternoon, which reflects the production of nitrates and other reactive nitrogen compounds from NO_x in the daytime. When photolytic measurements are available, we only use the photolytic observations in this study; otherwise, we use the scaled catalytic measurements.

Nineteen surface O_3 monitoring sites were operating in the DISCOVER-AQ region during the campaign (Figure 1). They measured O_3 concentrations by using a Federal Equivalent Method (FEM) based on the UV absorption of O_3 (https://www.arb.ca.gov/aaqm/qa/qa-manual/vol4/chapter6o3.pdf, last access: April 6, 2019) with an uncertainty of 5 ppb.

2.6 Aircraft measurements of NO_2 vertical profiles

In this study, we mainly use the NO_2 concentrations measured by the National Center for Atmospheric Research (NCAR) 4-channel chemiluminescence instrument (P-CL) onboard the P-3B aircraft for the evaluation of REAM simulated NO_2 vertical profiles. The instrument has a NO_2 measurement uncertainty of 10% – 15% and a 1-second, 1-sigma detection limit of 30 pptv.

NO_2 measurements from aircraft spirals provide us with NO_2 vertical profiles. Figure 1 shows the locations of the aircraft spirals during the DISCOVER-AQ campaign, except for the Chesapeake Bay spirals over the ocean. There were only six spirals available over the Chesapeake Bay, which have ignorable impacts on the following analyses. Therefore, we do not use them in this study. The rest 239 spirals in the daytime for July 2011 are used to compute the average profiles of NO_2 for the six inland sites (Figure 1).

The aircraft measurements were generally sampled from about a height of 300 m AGL in the boundary layer to 3.63 km AGL in the free troposphere. We bin these measurements to REAM vertical levels. In order to make up the missing observations between the surface and 300 m, we apply quadratic polynomial regressions by using aircraft data below 1 km and coincident NO_2 surface measurements.

In addition to using NO_2 concentrations from the NCAR 4-channel instrument to evaluate REAM simulated NO_2 vertical profiles, we also use P-3B NO, NO_2, and NO_y concentrations measured by the NCAR 4-channel instrument and NO_2, total peroxyacyl nitrates ($\sum$PNs), total alkyl nitrates ($\sum$ANs) (include alkyl nitrates and hydroxyalkyl nitrates), and HNO_3 concentrations measured by the thermal dissociation-laser induced fluorescence (TD-LIF) technique (Day et al., 2002; Thornton et al., 2000; Wooldridge et al., 2010) to evaluate the concentrations of NO_y from REAM (Table 1). All these P-3B measurements are vertically binned to REAM grid cells for comparisons with REAM results. In addition, below the P-3B spirals, four NO_y observation sites at

Padonia, Edgewood, Beltsville, and Aldino were operating to provide continuous hourly NO_y surface concentrations during the campaign, which we also use to evaluate REAM simulated NO_y surface concentrations in this study. We summarize the information of available observations at the 11 inland Pandora sites in Table S1.

3 Results and discussion

3.1 Evaluation of WRF simulated meteorological fields

We evaluate the performances of the 36-km and nested 4-km WRF simulations using temperature, potential temperature, relative humidity (RH), and wind measurements from the P-3B spirals (Figure 1) and precipitation data from the NCEP (National Centers for Environmental Prediction) Stage IV precipitation dataset. Generally, P-3B spirals range from ~300 m to ~3.63 km in height above the ground level (AGL). As shown in Figure S4, both the 36-km and nested 4-km WRF simulations simulate temperature well with $R^2 = 0.98$. Both WRF simulations show good agreement with P-3B measurements in U-wind (36-km: $R^2 = 0.77$; 4-km: $R^2 = 0.76$), V-wind (36-km: $R^2 = 0.79$; 4-km: $R^2 = 0.78$), wind speed (36-km: $R^2 = 0.67$; 4-km: $R^2 = 0.67$), and wind direction ~~(36-km: $R^2 = 0.46$; 4-km: $R^2 = 0.52$)~~ (Figures S4 and S5). We further compare the temporal evolutions of vertical profiles for temperature, potential temperature, RH, U-wind, and V-wind below 3 km from the P-3B observations with those from the 36-km and nested 4-km WRF simulations in Figure S6. Both WRF simulations well capture the temporospatial variations of P-3B observed vertical profiles except that RH below 1.5 km is significantly underestimated during 9:00 – 17:00 LT in both WRF simulations. The evaluations above suggest that WRF simulated wind fields are good and comparable at 4-km and 36-km resolutions, but potential dry biases exist in both WRF simulations.

The NCEP Stage IV precipitation dataset provides hourly precipitation across the contiguous United States (CONUS) with a resolution of ~4 km based on the merging of rain gauge data and radar observations (Lin and

Mitchell, 2005; Nelson et al., 2016). The Stage IV dataset is useful for evaluating model simulations, satellite precipitation estimates, and radar precipitation estimates (Davis et al., 2006; Gourley et al., 2011; Kalinga and Gan, 2010; Lopez, 2011; Yuan et al., 2008). We obtain the Stage IV precipitation data for July 2011 from the NCAR/UCAR Research Data Archive (https://rda.ucar.edu/datasets/ds507.5/, last access: December 28, 2019). As shown in Figures S7 and S8, generally, both the 36-km and nested 4-km WRF simulations generally predict much less precipitation (in precipitation amount and duration) compared to the Stage-IV data in July 2011 around the DISCOVER-AQ campaign region, especially for the nested 4-km WRF simulation, consistent with the aforementioned underestimated RH and dry bias in WRF simulations. The precipitation biases in the WRF model will affect REAM simulations of trace gases, leading to high biases of soluble species due to underestimated wet scavenging. Clouds interfere with satellite observations. Therefore, the precipitation bias does not affect model evaluations with satellite measurements of NO_2. Aircraft measurements were also taken in non-precipitating days.

3.2 Effect of boundary layer vertical mixing on the diurnal variations of surface NO_2 concentrations

3.2.1 36-km model simulation in comparison to the surface observations

Figures 5a and 5b show the observed and 36-km REAM simulated diurnal cycles of surface NO_2 and O_3 concentrations on weekdays in July 2011 in the DISCOVER-AQ region. REAM with WRF-YSU simulated vertical diffusion coefficient (k_{zz}) values significantly overestimates NO_2 concentrations and underestimates O_3 concentrations at night, although it captures the patterns of the diurnal cycles of surface NO_2 and O_3: an O_3 peak and a NO_2 minimum around noontime. Here, YSU denotes the Yonsei University planetary boundary layer (PBL) scheme (Shin and Hong, 2011) used by our WRF simulations (Table S2). At night, the reaction of $O_3 + NO \rightarrow O_2 + NO_2$ produces NO_2 but removes O_3. Since most NO_x emissions are in the form of NO, the model biases of low O_3 and high NO_2 occur at the same time. Since there are no significant chemical sources of O_3 at night, mixing of O_3 rich air above the surface is the main source of O_3 supply near the surface. Therefore, the nighttime model

biases with WRF-YSU simulated k_{zz} data in Figure 5 indicate that vertical mixing may be underestimated at night.

During the DISCOVER-AQ campaign, WRF simulated vertical wind velocities are very low at night and have little impact on vertical mixing (Figure S9a). The nighttime vertical mixing is mainly attributed to turbulent mixing. ~~In the YSU scheme, boundary layer k_{zz} is correlated to PBLH.~~ However, ~~Breuer et al. (2014) and~~ Hu et al. (2012) found that the YSU scheme underestimated nighttime ~~PBLHs~~PBL vertical turbulent mixing in WRF, which is consistent with Figure 6 showing that WRF-YSU k_{zz}-determined ~~PBLHs~~ mixed-layer heights (MLHs) are significantly lower than lidar observations in the late afternoon and at night at the UMBC site during the DISCOVER-AQ campaign (Knepp et al., 2017). Here, the k_{zz}-determined ~~PBLH~~ MLH refers to the mixing height derived by comparing k_{zz} to its background values (Hong et al., 2006) but not the PBLH outputs from WRF. UMBC is an urban site (Table S1), surrounded by a mixture of constructed materials and vegetation. The UMBC lidar ~~mixing depth~~MLH data were derived from the Elastic Lidar Facility (ELF) attenuated backscatter signals by using the covariance wavelet transform (CWT) method and had been validated against radiosonde measurements (N (Number of data points) = 24; R^2 = 0.89; bias (ELF – radiosonde) = 0.03 ± 0.23 km), Radar wind profiler observations (N = 659; R^2 = 0.78; bias = -0.21 ± 0.36 km), and Sigma Space mini-micropulse lidar data (N = 8122; R^2 = 0.85; bias = 0.02 ± 0.22 km) from the Howard University Beltsville Research Campus (HUBRC) in Beltsville, Maryland (38.058° N, 76.888° W) in the daytime during the DISCOVER-AQ campaign (Compton et al., 2013). It is noteworthy that although CWT is not designed to detect the nocturnal boundary layer (NBL), it does consider the residue layer (RL) and distinguish it from MLH in the early morning after sunrise, which is similar to nighttime conditions. Therefore, CWT can detect nighttime MLHs, although with large uncertainties due to the hard-coded assumption of RL = 1 km in the algorithm and insufficient vertical resolution of the technique. In addition, the sunrise and sunset time in July 2011 is about 5:00 LT and 19:30 LT (https://gml.noaa.gov/grad/solcalc/sunrise.html, last access: May 27, 2021), respectively. Figure 6 shows that

WRF-YSU k_{zz}-determined MLHs are significantly lower than ELF observations after sunrise at 5:00 – 8:00 LT and before sunset at 18:00 – 20:00 LT. Even if we do not consider MLHs at night (19:30 – 5:00 LT), we can still conclude that WRF-YSU underestimates vertical mixing in the early morning after sunrise and the late afternoon before sunset, enabling a reasonable assumption that WRF-YSU also underestimates nighttime vertical mixing. Moreover, the nighttime MLHs in Figure 6 are comparable to those measured by the Vaisala CL51 ceilometer at the Chemistry And Physics of the Atmospheric Boundary Layer Experiment (CAPABLE) site in Hampton, Virginia (Knepp et al., 2017). Finally, we want to emphasize that different definitions of NBL can result in significantly different NBL heights (Breuer et al., 2014). In this study, we follow Knepp et al. (2017) to use MLHs derived from aerosol backscatter signals as the measure of vertical pollutant mixing within the boundary layer, which is simulated by k_{zz} in REAM.

To improve nighttime ~~PBLHs and~~ PBL vertical turbulent mixing in REAM, we increase k_{zz} below 500 m during 18:00 – 5:00 LT to 5 m s^{-2} if the WRF-YSU computed k_{zz} < 5 m s^{-2}, which significantly increases the k_{zz}-determined ~~PBLHs~~ MLHs at night (Figure 6), leading to the decreases of simulated surface NO_2 and the increases of surface O_3 concentrations at night (Figure 5). The assigned value of 5 m s^{-2} is arbitrary. Changing this value to 2 or 10 m s^{-2} can also alleviate the biases of model simulated nighttime surface NO_2 and O_3 concentrations (Figure S10). Considering the potential uncertainties of nighttime NO_x emissions, a~~A~~n alternative solution to correct the model nighttime simulation biases is to reduce NO_x emissions, which can decrease the consumption of O_3 through the process of NO_x titration mentioned above ($O_3 + NO \rightarrow O_2 + NO_2$). Our sensitivity tests (not shown) indicate that it is necessary to reduce NO_x emissions by 50-67% to eliminate the model nighttime simulation biases, but we cannot find good reasons to justify this level of NO_x emission reduction only at night.

The updated REAM simulation of surface NO_2 diurnal pattern in Figure 5a is in good agreement with previous studies (Anderson et al., 2014; David and Nair, 2011; Gaur et al., 2014; Reddy et al., 2012; Zhao et al.,

2019). Daytime surface NO_2 concentrations are much lower compared to nighttime, and NO_2 concentrations reach a minimum around noontime. As shown in Figure S11, under the influence of vertical turbulent mixing, the surface-layer NO_x emission diurnal pattern is similar to the surface NO_2 diurnal cycle in Figure 5a, emphasizing the importance of turbulent mixing on modulating surface NO_2 diurnal variations. The highest boundary layer (Figure 6) due to solar radiation leads to the lowest surface-layer NO_x emissions (Figure S11) and, therefore, the smallest surface NO_2 concentrations occur around noontime (Figure 5a). Transport, which is mainly attributed to advection and turbulent mixing, is another critical factor affecting surface NO_2 diurnal variations (Figure S11). The magnitudes of transport fluxes (Figure S11) are proportional to horizontal and vertical gradients of NO_x concentrations and are therefore generally positively correlated to surface NO_2 concentrations. However, some exceptions exist, reflecting different strengths of advection (U, V, and W) and turbulent mixing (k_{zz}) at different times. For example, in the early morning, NO_2 surface concentrations peak at 5:00 – 6:00 LT (Figure 5a), while transport fluxes peak at 7:00 – 8:00 LT (Figure S11). The delay of the peak is mainly due to lower turbulent mixing at 5:00 – 6:00 LT than other daytime hours in the model (Figure 6). Chemistry also contributes to surface NO_2 diurnal variations mainly through photochemical sinks in the daytime and N_2O_5 hydrolysis at nighttime. Chemistry fluxes in Figure S11 are not only correlated to the strength of photochemical reactions and N_2O_5 hydrolysis (chemistry fluxes per unit NO_x) but are also proportional to NO_x surface concentrations. Therefore, chemistry fluxes in Figure S11 cannot directly reflect the impact of solar radiation on photochemical reactions. It can, however, still be identified by comparing afternoon chemistry contributions: from 13:00 to 15:00 LT, surface-layer NO_x emissions and NO_2 concentrations are increasing (Figures S11 and 5a); however, chemistry losses are decreasing as a result of the reduction of photochemical sinks with weakening solar radiation. The contributions of vertical mixing and photochemical sinks to NO_2 concentrations can be further corroborated by daytime variations of NO_2 vertical profiles and TVCDs discussed in sections 3.3 and 3.4.

Figure 5c shows the diurnal variation on weekends is also simulated well in the improved 36-km model. The diurnal variation of surface NO_2 concentrations (REAM: 1.5 – 10.2 ppb; observations: 2.1 – 9.8 ppb) is lower than on weekdays (REAM: 2.4 – 12.2 ppb; observations: 3.3 – 14.5 ppb), reflecting lower magnitude and variation of NO_x emissions on weekends (Figure 3). Figure 5d also shows an improved simulation of surface O_3 concentrations at nighttime due to the improved ~~PBLH~~ MLH simulation (Figure 6).

3.2.2 4-km model simulation in comparison to the surface observations

The results of 4-km REAM simulations with original WRF-YSU k_{zz} (not shown) are very similar to Figure 5 since WRF simulated nocturnal vertical mixing is insensitive to the model horizontal resolution. Applying the modified nocturnal mixing in the previous section also greatly reduced the nighttime NO_2 overestimate and O_3 underestimate in the 4-km REAM simulations. All the following analyses are based on REAM simulations with improved nocturnal mixing. Figure 7 shows that mean surface NO_2 concentrations simulated in the 4-km model are higher than the 36-km results over Padonia, Oldtown, Essex, Edgewood, Beltsville, and Aldino (Table S1), leading to generally higher biases compared to the observations in the daytime. A major cause is that the observation sites are located in regions of high NO_x emissions (Figure 2). At a higher resolution of 4 km, the high emissions around the surface sites are apparent compared to rural regions. At the coarser 36-km resolution, spatial averaging greatly reduces the emissions around the surface sites. On average, NO_x emissions (molecules km^{-2} s^{-1}) around the six surface NO_2 observations sites are 67% higher in the 4-km than the 36-km REAM simulations (Table S1). The resolution dependence of model results will be further discussed in the model evaluations using the other in situ and remote sensing measurements.

438 3.3 Diurnal variations of NO_2 vertical profiles

439 Figures 8a and 8c show the temporal variations of P-3B observed and 36-km REAM simulated NO_2 vertical
440 profiles in the daytime on weekdays during the DISCOVER-AQ campaign. 36-km REAM reproduces well the
441 observed characteristics of NO_2 vertical profiles in the daytime (R^2 = 0.89), which are strongly affected by
442 vertical mixing and photochemistry (Zhang et al., 2016). When vertical mixing is weak in the early morning
443 (6:00 – 8:00 LT), NO_2, released mainly from surface NO_x sources, is concentrated in the surface layer, and the
444 vertical gradient is large. As vertical mixing becomes stronger after 8:00 LT, NO_2 concentrations below 500 m
445 decrease significantly, while those over 500 m increase from 6:00 – 8:00 LT to 12:00 – 14:00 LT. It is
446 noteworthy that ~~PBLHs~~ MLHs and NO_x emissions are comparable between 12:00 – 14:00 LT and 15:00 – 17:00
447 LT (Figures 3 and 6); however, NO_2 concentrations at 15:00 – 17:00 LT are significantly higher than at 12:00 –
448 14:00 LT in the whole boundary layer, reflecting the impact of the decreased photochemical loss of NO_x in the
449 late afternoon. In fact, photochemical losses affect all the daytime NO_2 vertical profiles, which can be easily
450 identified by NO_2 TVCD process diagnostics discussed in section 3.4 (Figure 9).

451 Figures 8b and 8d also show the observed and 36-km REAM simulated vertical profiles on weekends.
452 Similar to Figures 5 and 7, observed and simulated concentrations of NO_2 are lower on weekends than on
453 weekdays. Some of the variations from weekend profiles are due to a lower number of observations (47 spirals)
454 on weekends. The overall agreement between the observed vertical profiles and 36-km model results is good on
455 weekends (R^2 = 0.87). At 15:00 – 17:00 LT, the model simulates a larger gradient than what the combination of
456 aircraft and surface measurements indicates. It may be related to the somewhat underestimated ~~PBLHs~~ MLHs in
457 the late afternoon in the model (Figure 6).

458 On weekdays, most simulated vertical profiles at the 4-km resolution (Figure 8e) are similar to 36-km results
459 in part because the average NO_x emissions over the six P-3B spiral sites are about the same, 4% lower in the 4-

km than the 36-km REAM simulations (Table S1). A clear exception is the 4-km REAM simulated vertical profile at 15:00 – 17:00 LT when the model greatly overestimates boundary layer NO_x mixing and concentrations. The main reason is that WRF simulated vertical velocities (w) in the late afternoon are much larger in the 4-km simulation than the 36-km simulation (Figure S9), which can explain the simulated fully mixed boundary layer at 15:00 – 17:00 LT. Since it is not designed to run at the 4-km resolution and it is commonly assumed that convection can be resolved explicitly at high resolutions, the Kain-Fritsch (new Eta) convection scheme is not used in the nested 4-km WRF simulation (Table S2); it may be related to the large vertical velocities in the late afternoon when thermal instability is the strongest. Appropriate convection parameterization is likely still necessary for 4-km simulations (Zheng et al., 2016), which may also help alleviate the underestimation of precipitation in the nested 4-km WRF simulation as discussed in section 3.1.

The same rapid boundary-layer mixing due to vertical transport is present in the 4-km REAM simulated weekend vertical profile (Figure 8f), although the mixing height is lower. Fewer spirals (47) and distinct transport effect due to different NO_2 horizontal gradients between the 4-km and 36-km REAM simulations (discussed in detail in Section 3.6) may cause the overestimation of weekend profiles in the 4-km REAM simulation.

3.4 Daytime variation of NO_2 TVCDs

We compare satellite, P-3B aircraft, and model-simulated TVCDs with Pandora measurements, which provide continuous daytime observations. The locations of Pandora sites are shown in Table S1 and Figure 1. Among the Pandora sites, four sites are located significantly above the ground level: UMCP (~20 m), UMBC (~30 m), SERC (~40 m), and GSFC (~30 m). The other sites are 1.5 m AGL. To properly compare Pandora to other measurements and model simulations, we calculate the missing TVCDs between the Pandora site heights and ground surface by multiplying the Pandora TVCDs with model-simulated TVCD fractions of the corresponding columns. The resulting correction is 2-21% ($\frac{1}{1-missing\ TVCD\ percentage}$) for the four sites

significantly above the ground surface, but the effect on the averaged daytime TVCD variation of all Pandora sites is small (Figure S12). In the following analysis, we use the updated Pandora TVCD data.

The weekday diurnal variations of NO_2 TVCDs from satellites, Pandora, 4- and 36-km REAM, and the P-3B aircraft are shown in Figure 10a. We calculate aircraft derived TVCDs by using equation (1):

$$TVCD_{aircraft}(t) = \frac{\sum c_{aircraft}(t) \times \rho_{REAM}(t) \times V_{REAM}(t)}{A_{REAM}} \quad (1),$$

where t is time; $c_{aircraft}$ (v/v) denotes aircraft NO_2 concentrations (mixing ratios) at each level at time t; ρ_{REAM} ($molecules / cm^3$) is the density of air from 36-km REAM at the corresponding level; V_{REAM} (cm^3) is the volume of the corresponding 36-km REAM grid cell; A_{REAM} (cm^2) is the surface area (36×36 km^2). In the calculation, we only use NO_2 concentrations below 3.63 km AGL because few aircraft measurements were available above this height in the campaign. Missing tropospheric NO_2 above 3.63 km AGL in the aircraft TVCD calculation has little impact on our analyses, as 36-km REAM model simulation shows that 85% ± 7% of tropospheric NO_2 are located below 3.63 km AGL during 6:00 – 17:00 LT in the DISCOVER-AQ region, which is roughly consistent with the GMI model results with 85% - 90% tropospheric NO_2 concentrated below 5 km (Lamsal et al., 2014). It should be noted that only six P-3B spirals are available during the campaign, less than the samplings of 11 inland Pandora sites.

The 4-km REAM simulated NO_2 TVCDs are mostly higher than the 36-km results and the observations in daytime on weekdays (Figure 10a). However, since the standard deviations of the data are much larger than the model difference, the 4- and 36-km model results generally show similar characteristics relative to the observations. REAM simulation results are in reasonable agreement with Pandora, P-3B aircraft, and satellite daytime NO_2 TVCDs, except that NASA-derived OMI (OMNO2) TVCDs are somewhat lower than other datasets, which may be partly due to biased a priori vertical profiles from the GMI model in the NASA retrieval

in the campaign (Lamsal et al., 2014; Lamsal et al., ~~2020~~2021). TVCDs derived by using the DOMINO algorithm and 36-km REAM NO_2 vertical profiles are in agreement with those from KNMI, which indicates that the TM4 model from KNMI provides reasonable estimates of a priori NO_2 vertical profiles on weekdays in the DISCOVER-AQ region in summer.

We find evident decreases of NO_2 TVCDs from GOME-2A to OMI in Figure 10a, which is consistent with Pandora, REAM results, and previous studies that showed decreasing NO_2 TVCDs from SCIAMACHY to OMI due to photochemical losses in summer (Boersma et al., 2008; Boersma et al., 2009). P-3B aircraft TVCDs also show this decrease feature but have large variations due in part to the limited aircraft sampling data.

Pandora NO_2 TVCD data have different characteristics from REAM simulated and P-3B aircraft measured TVCDs at 5:00 – 7:00 LT and 14:00 – 18:00 LT (Figure 10a). At 5:00 – 7:00 LT, Pandora data show a significant increase of NO_2 TVCDs, but REAM and aircraft TVCDs generally decrease except for 4-km REAM TVCDs with a slight increase from 6:00 – 7:00 LT on weekdays. At 14:00 LT – 18:00 LT, Pandora TVCDs have little variations, but REAM and aircraft TVCDs increase significantly. The relatively flat Pandora TVCDs in the late afternoon compared to REAM and P-3B aircraft measurements are consistent with Lamsal et al. (2017), which found ~~the significant underestimation (26% – 30%) of~~ that Pandora VCDs were 26% - 30% lower than ~~compared to~~ UC-12 ACAM measurements from 16:00 LT to 18:00 LT during the DISCOVER-AQ campaign. We show the simulated effects of emission, chemistry, transport, and dry deposition on NO_x TVCDs in Figure 9. The simulated early morning slight decrease of NO_2 TVCDs is mainly due to the chemical transformation between NO_2 and NO favoring the accumulation of NO under low-O_3 and low-HO_2/RO_2 conditions, thus NO TVCDs increase significantly, but NO_2 TVCDs continue decreasing slowly during the period. The increase in the late afternoon is primarily due to the decrease of photochemistry-related sinks. The reasons for the discrepancies of NO_2 TVCDs between Pandora and REAM results during the above two periods are unclear. Large SZAs in the early morning

and the late afternoon (Figure S1) lead to the higher uncertainties of Pandora measurements (Herman et al., 2009), although we have excluded Pandora measurements with SZA > 80°. In addition, Pandora is a sun-tracking instrument with a small effective FOV and is sensitive to local conditions within a narrow spatial range which may differ significantly from the average properties of 36- and 4-km grid cells depending upon the time of the day (Figure S13) (Herman et al., 2009; Herman et al., 2018; Herman et al., 2019; Judd et al., 2018; Judd et al., 2019; Judd et al., 2020; Lamsal et al., 2017; Reed et al., 2015). As we mentioned above, ~85% tropospheric NO_2 are located below 3.63 km in the DISCOVER-AQ 2011 region based on the 36-km REAM simulation results. The Pandora FOV of 1.6° is approximately equivalent to a nadir horizontal extension of only 0.1 km ($2 \times 3.63\ km \times tan\frac{1.6}{2} = 0.1$ km) at 3.63 km AGL and 30 m at 1.0 km AGL. Therefore, Pandora measures different air columns of NO_2 at different times of the day, especially in the morning and afternoon when SZA is large, as shown in Figure S13. Considering the potential spatial heterogeneity of boundary-layer NO_2, it is possible that the morning (east), noontime (nadir), afternoon (west) NO_2 VCDs are significantly different from each other. Unlike Pandora, satellites and aircraft are far from the ground surface and cover large areas; therefore, the impact of SZA on their NO_2 VCD measurements is insignificant compared to Pandora measurements. Another possible reason is that Pandora instruments had few observations in the early morning, and the resulting average may not be representative (Figure S2).

To further understand the daytime variation of NO_2 TVCDs, we examine P-3B aircraft data derived and REAM simulated NO_2 VCD variations for different height bins (Figure 11). NO_2 VCDs below 3.63 km AGL display a "U"-shaped pattern from 5:00 LT to 17:00 LT. In the morning, as vertical mixing becomes stronger after sunrise, high-NO_x air in the lower layer is mixed with low-NO_x air in the upper layer. The increase of NO_x vertical mixing above 300 m is sufficient to counter the increase of photochemical loss in the morning. Conversely, the NO_2 VCDs below 300 m decrease remarkably from sunrise (about 6:00 LT) to around noontime

due to both vertical mixing and the increase of photochemical strength. From 13:00 LT to 16:00 LT, NO_2 VCDs increase slowly, reflecting a relative balance among emissions, transport, chemistry, and dry depositions. The sharp jump of the VCDs from 16:00 LT to 17:00 LT is mainly due to dramatically reduced chemical loss. And 4-km REAM simulated NO_2 VCDs at 0.30-3.63 km at 16:00-17:00 LT are much higher than 36-km results partly because of the rapid vertical mixing in the 4-km REAM simulation (Figures 8 and S9).

Similar to NO_2 surface concentrations and vertical profiles in Figures 7 and 8, the NO_2 TVCD variation is also smaller on weekends than on weekdays, but the day-night pattern is similar (Figure 10). Although the 4-km REAM NO_2 TVCDs are generally higher than the 36-km results and observations in the daytime, considering their large standard deviations, NO_2 TVCDs from both simulations are comparable to satellite products, Pandora, and P-3B aircraft observations most of the time on weekends. The exception is that Pandora TVCDs have different variation patterns in the early morning and late afternoon from REAM simulations, similar to those found on weekdays.

3.5 Model comparisons with NO_y measurements

NO_y is longer-lived than NO_x, and NO_y concentrations are not affected by chemistry as much as NO_x. We obtain two types of NO_y concentrations from the P-3B aircraft in the DISCOVER-AQ campaign: one is NO_y concentrations directly measured by the NCAR 4-channel instrument, corresponding to the sum of NO, NO_2, $\sum$PNs, $\sum$ANs, HNO_3, N_2O_5, HNO_4, HONO, and the other reactive nitrogenic species in REAM (all the other species are described in Table 1); the other one, which we name as "derived-NO_y", is the sum of NO from the NCAR 4-channel instrument and NO_2 (NO_2_LIF), $\sum$PNs, $\sum$ANs, and HNO_3 measured by the TD-LIF technique, corresponding to NO, NO_2, $\sum$PNs, $\sum$ANs, and HNO_3 in REAM (Table 1). On average, P-3B derived-NO_y concentrations (2.88 ± 2.24 ppb) are 17% higher than coincident P-3B NO_y concentrations (2.46 ± 2.06 ppb) with $R^2 = 0.75$, generally reflecting consistency between these two types of measurements. As shown in Table 1, on

weekdays, the 36-km REAM NO_y concentrations are 45% larger than P-3B with $R^2 = 0.33$, and the 36-km REAM derived-NO_y concentrations are 8% larger than P-3B with $R^2 = 0.41$. 4-km REAM show similar results, suggesting that REAM simulations generally reproduce the observed NO_y and derived-NO_y concentrations within the uncertainties, although the average values from REAM are somewhat larger than the observations due in part to the underestimate of precipitation in the WRF model simulations resulting in underestimated wet scavenging of HNO_3 in REAM. The concentrations of weekday NO, NO_2, and ∑PNs from REAM simulations are also comparable to the observations. However, weekday ∑ANs concentrations are 68% lower in the 36-km REAM than observations, suggesting that the chemistry mechanism in REAM may need further improvement to better represent isoprene nitrates. It is noteworthy that, since ∑ANs only account for a small fraction (~11%) in observed derived-NO_y, the absolute difference between REAM simulated and P-3B observed ∑ANs concentrations is still small compared to HNO_3. Weekday HNO_3 concentrations are significantly higher in REAM simulations (36-km: 57%, 0.65 ppb; 4-km: 74%, 0.86 ppb) than P-3B observations, which is the main reason for the somewhat larger NO_y and derived-NO_y concentrations in REAM compared to P-3B observations. The higher HNO_3 concentrations in REAM may be related to the underestimation of precipitation in the corresponding WRF simulations, as discussed in section 3.1 (Figures S7 and S8), leading to the underestimated wet scavenging of HNO_3, especially for the 4-km REAM simulation.

We also examine the weekday diurnal variations of derived-NO_y vertical profiles from P-3B and REAM simulations in Figure S14. Generally, both 36- and 4-km REAM simulations capture the variation characteristics of observed vertical profiles, which are similar to those for NO_2 in Figure 8. REAM derived-NO_y concentrations are comparable to P-3B observations at most vertical levels on weekdays. Some larger derived-NO_y concentrations in the model results can be partially explained by larger HNO_3 concentrations in REAM, such as those below 1 km at 9:00 – 11:00 LT for the 36-km REAM and those below 2.0 km at 12:00 – 17:00 LT for the 4-km REAM (Figure S15).

Figure 12 shows the comparison of the diurnal cycles of surface NO_y concentrations observed at Padonia, Edgewood, Beltsville, and Aldino during the DISCOVER-AQ campaign with those from the REAM simulations. Generally, the REAM simulations reproduce the observed surface NO_y diurnal cycles except for the spikes around 17:00 – 20:00 LT due to still underestimated ~~PBLHs~~ MLHs (Figure 6). 4-km simulation results have a higher bias than 36-km results relative to the observations in the daytime, similar to the comparisons of NO_2 surface concentrations and TVCDs in Figures 7 and 10 due to higher emissions around the observation sites in 4- than 36-km simulations (Table S1 and Figure 2).

3.6 Resolution dependence of NO_x emission distribution

We show previously that the 4-km REAM simulated NO_2 and NO_y surface concentrations and NO_2 TVCDs are higher than observations in the daytime in comparison to the corresponding 36-km REAM results (Figures 7, 10, and 12). An examination of monthly mean NO_2 surface concentrations and TVCDs for July 2011 also shows that 4-km simulation results are significantly higher than the 36-km results over the 11 inland Pandora sites in the daytime (Figure 13). The process-level diagnostics in Figure 9 indicate that the mean contribution of NO_x emissions to NO_x ΔTVCDs in the 4-km simulation is 1.32×10^{15} molecules cm^{-2} h^{-1} larger than that in the 36-km simulation between 9:00 LT and 16:00 LT, while the absolute mean contributions of chemistry and transport (they are negative in Figure 9, so we use absolute values here) in the 4-km simulation are 0.26×10^{15} and 0.87×10^{15} molecules cm^{-2} h^{-1} larger than the 36-km simulation, respectively. The contributions of dry deposition to NO_x ΔTVCDs are negligible compared to other factors in both simulations (Figure 9). Therefore, the 34% higher NO_x emissions over the 11 inland Pandora sites (Table S1 and Figure 3) is the main reason for the larger daytime NO_2 surface concentrations and TVCDs in the 4-km than the 36-km REAM simulations (Figure 13). The significantly different contribution changes between NO_x emissions (1.32×10^{15} molecules cm^{-2} h^{-1} or about one third) and chemistry (0.26×10^{15} molecules cm^{-2} h^{-1} or about 8%) reflect potential chemical nonlinearity (Li et al., 2019; Silvern et al., 2019; Valin et al., 2011) and transport effect. Different transport contributions between the 4-

615 km and the 36-km REAM are mainly caused by their different NO_x horizontal gradients (Figures 2, 14, and 15),
616 while the impact of wind fields is small since we do not find significant differences in horizontal wind
617 components between the two simulations except for some lower wind speeds below 1000 m for the 36-km WRF
618 simulation compared to the nested 4-km WRF simulation (Figure S16). Our sensitivity tests with the WRF
619 Single-Moment 3-class (WSM3) simple ice scheme (not shown) can improve the wind speed comparison below
620 1000 m between the 36-km and nested 4-km WRF simulations but still produce similar NO_x simulation results as
621 WSM6 shown here. Therefore, the somewhat lower wind speeds below 1000 m in the 36-km WRF simulation are
622 not the reason for the difference between the 4-km and 36-km REAM simulations. The impact of transport on the
623 two REAM simulations can be further verified by the comparison of NO_2 TVCDs over the six P-3B spiral sites
624 between the two simulations (Figure S17). Mean NO_x emissions over the six P-3B spiral sites are close (relative
625 difference < 4%) between the two simulations (Table S1 and Figure S17). From 9:00 to 12:00 LT, the
626 contributions of NO_x emissions to NO_x ΔTVCDs are 2.50×10^{15} and 2.49×10^{15} molecules cm^{-2} h^{-1} for the 36-km
627 and 4-km REAM simulations, respectively, and the contributions of chemistry are also close between the two
628 simulations (36-km: -2.62×10^{15} molecules cm^{-2} h^{-1}; 4-km: -2.69×10^{15} molecules cm^{-2} h^{-1}). However, the
629 contributions of transport are -0.39×10^{15} and 0.03×10^{15} molecules cm^{-2} h^{-1} for the 36-km and 4-km REAM
630 simulations, respectively, leading to larger NO_2 TVCDs in the 4-km REAM simulation than the 36-km REAM
631 from 9:00 – 12:00 LT (Figure S17c). Since horizontal wind fields over the six P-3B spiral sites are comparable
632 between two simulations (Figures S4, S5, S6, and S16) and larger NO_x horizontal gradients are found near the P-
633 3B spiral sites for the 4-km REAM (Figure 2), we attribute the different transport contributions between the two
634 simulations to a much larger NO_x emission gradient around the measurement locations in 4-km than 36-km
635 emission distributions.

636 We re-grid the 4-km REAM results into the grid cells of the 36-km REAM, which can significantly reduce
637 the impact of different NO_x emission distributions and associated transport on the two simulations. Compared to

638 the original 4-km REAM results, the re-gridded surface NO_2 concentrations and TVCDs over the 11 inland
639 Pandora sites are much closer to the 36-km REAM results (Figure 13). After re-gridding the 4-km REAM results
640 into 36-km REAM grid cells, we also find more comparable NO_y surface concentrations between the re-gridded
641 4-km results and the 36-km REAM results (Figure S18). The remaining discrepancies between the re-gridded
642 results and the 36-km REAM results may be due to chemical nonlinearity and other meteorological effects, such
643 as larger vertical wind in the 4-km REAM (Figure S9) and their different k_{zz} values in the PBL. Although other
644 factors, such as chemical nonlinearity and vertical diffusion, may affect the 36-km and 4-km REAM simulations
645 differently, the difference between 4- and 36-km simulations of reactive nitrogen is largely due to that of NO_x
646 emissions.

647 The 4- and 36-km simulation difference depends on the location of the observations. In some regions, the
648 NO_x emission difference between 4- and 36-km simulations is small. The comparison of NO_y measurements from
649 P-3B spirals with coincident REAM results in Table 1 suggests that the 4-km and 36-km REAM simulations
650 produce similar NO_y (relative difference ~4%) and derived-NO_y (relative difference ~6%) concentrations on
651 weekdays, and both simulation results are comparable to the observations. The NO_y similarity over the P-3B
652 spiral sites between the 36-km and 4-km REAM simulations is consistent with the comparable NO_x emissions
653 over (relative difference < 4%) the six P-3B spiral sites between the two simulations (Table S1). The differences
654 between the 4-km model simulation results and P3-B observations are larger on weekends than on weekdays
655 (Table 1) due to the limited weekend sampling since model simulated monthly mean values show similar
656 differences between the 4-km and 36-km REAM simulations on weekends as on weekdays (not shown).

657 3.7 Evaluation of 36- and 4-km NO_x distribution with OMI, GOME-2A, and ACAM measurements

658 The evaluation of model simulations of surface, aircraft, and satellite observations tends to point out a high
659 bias in 4- than 36-km model simulations. We note that this comparison is based on the averages of multiple sites.

660 NO_x emissions at individual sites are not always higher in the 4-km than 36-km REAM, such as SERC, Fairhill,
661 and Essex, with much higher 36-km NO_x emissions than 4-km NO_x emissions (Table S1). We conduct
662 individual-site comparisons of surface NO_2 concentrations, surface NO_y concentrations, NO_2 vertical profiles,
663 derived-NO_y vertical profiles, and NO_2 TVCDs of the 36-km REAM and the 4-km REAM results relative to the
664 corresponding observations in Figures S19 – S23. The 36-km simulation results can be larger, smaller, or
665 comparable to the 4-km simulation results, and both simulations can produce higher, lower, or similar results as
666 the observations for different variables at different sites. The varying model biases depending on the observation
667 site reflect the different spatial distributions of NO_x emissions between the 36- and 4-km REAM simulations
668 (Figure 2) and suggest potential distribution biases of NO_x emissions in both simulations.

669 Here we examine the 4-km model simulated NO_2 VCDs with high-resolution ACAM measurements onboard
670 the UC-12 aircraft in Figures 14 and S24, respectively. The spatial distributions of ACAM and 4-km REAM NO_2
671 VCDs are generally consistent with $R^2 = 0.35$ on weekdays and $R^2 = 0.50$ on weekends. The domain averages of
672 ACAM and 4-km REAM NO_2 VCDs are 4.7 ± 2.0 and $4.6 \pm 3.2 \times 10^{15}$ molecules cm^{-2} on weekdays and $3.0 \pm$
673 1.7 and $3.3 \pm 2.7 \times 10^{15}$ molecules cm^{-2} on weekends, respectively. The spatial distributions of ACAM and 4-km
674 REAM NO_2 VCDs are highly correlated with the spatial distribution of 4-km NEI2011 NO_x emissions. All three
675 distributions capture two strong peaks around Baltimore and Washington, D.C. urban regions and another weak
676 peak in the northeast corner of the domain (Wilmington city in Delaware) (Figures 14 and S24). However,
677 Figures 14 and S24 clearly show that NO_2 VCDs from the 4-km REAM simulation are more concentrated in
678 Baltimore and Washington, D.C. urban regions than ACAM, which are also reflected by the higher NO_2 VCD
679 standard deviations of the 4-km REAM results than ACAM. Several Pandora sites are in the highest NO_2 VCD
680 regions where the 4-km REAM generally produces larger NO_2 VCDs than ACAM, which explains why the NO_2
681 TVCDs over the 11 Pandora sites from the 4-km REAM simulation are higher than the observations (Figure 10)
682 and the 36-km REAM results (Figure 13) around noontime. Horizontal transport cannot explain the NO_2 VCD

distribution biases in the 4-km REAM simulation due to the following reasons. Firstly, horizontal wind fields are simulated as well by the nested 4-km WRF simulation as the 36-km WRF compared to P-3B measurements, as discussed in section 3.1. Secondly, the prevailing northwest wind in the daytime (Figure S5) should move NO_x eastward, but we find no significant eastward shift of NO_2 VCDs compared to NO_x emissions in both ACAM and 4-km REAM distributions (Figure 14). ~~Lastly, we find a local minimum of NO_2 VCDs in the middle of the Baltimore urban region (the purple circle in Figure 14b) in the ACAM distribution, which cannot be explained by horizontal transport or chemical nonlinearity due to the surrounding high NO_x emissions in the 4-km REAM simulation.~~ Therefore, we attribute the distribution inconsistency between ACAM and the 4-km REAM to the distribution biases of NEI2011 NO_x emissions at the 4-km resolution since the average below-aircraft NO_2 VCDs between ACAM and the 4-km REAM are about the same.

It is noteworthy that the number of data points used to calculate grid cell mean NO_2 VCDs varies significantly across the domain, as shown in Figures 14f and S24f. To mitigate potential sampling errors, we only consider the grid cells with ≥ 10 data points on weekdays in Figure S25. Whether we scale NO_2 VCDs using the corresponding domain averages (Figure S25) or not (not shown), the 4-km REAM generally shows more concentrated NO_2 VCDs in Baltimore and Washington, D.C. urban regions but more dispersed NO_2 VCDs in rural areas than ACAM, consistent with our discussion above. In addition, about 91% of ACAM NO_2 VCD data are measured from 8:00 – 16:00 LT, and only using ACAM NO_2 VCDs between 8:00 and 16:00 LT for the above comparison does not affect our results shown here. Moreover, to minimize the effect of overestimated afternoon vertical mixing (Figure 8) on the 4-km REAM simulation results, we also examine the comparison between ACAM NO_2 VCDs from 9:00 – 14:00 LT with coincident 4-km REAM results, which produces similar results as shown here. Finally, considering the NO_x lifetime difference between morning and noontime, we also analyze the NO_2 VCD data at 11:00 – 14:00 LT, and similar results are found.

We also evaluate the NO_2 VCD distributions from the 4-km REAM simulation on weekdays and weekends with ACAM NO_2 VCDs below the U-12 aircraft obtained from https://www-air.larc.nasa.gov/cgi-bin/ArcView/discover-aq.dc-2011?UC12=1#LIU.XIONG/ in Figures S2~~6~~5 and S2~~7~~6. Although the domain mean ACAM NO_2 VCDs in Figures S2~~6~~5 and S2~~7~~6 are higher than coincident 4-km REAM results due to the different retrieval method from Lamsal et al. (2017), such as different above-aircraft NO_2 VCDs and different a priori NO_2 vertical profiles, we can still find clear distribution inconsistencies between the 4-km REAM and ACAM NO_2 VCDs. The 4-km REAM NO_2 VCDs are more concentrated in the Baltimore and Washington, D.C. urban regions than this set of ACAM data, which is consistent with the conclusions derived from the ACAM dataset retrieved by Lamsal et al. (2017).

The potential distribution bias of the NEI2011 NO_x emissions at 36-km resolution is analyzed by comparing the 36-km REAM simulated NO_2 TVCDs with those retrieved by OMI and GOME-2A, as shown in Figures 15 (OMI, 13:00 LT) and S2~~8~~7 (GOME-2A, 9:30 LT). Both KNMI and our retrievals based on the 36-km REAM NO_2 vertical profiles show that OMI and GOME-2A NO_2 TVCDs have lower spatial variations than the corresponding 36-km REAM simulation results. OMI and GOME-2A retrievals have lower NO_2 TVCDs around the Baltimore and Washington, D.C. urban regions and higher values in relatively rural regions than the 36-km REAM. The distribution bias of the 36-km REAM NO_2 TVCDs is also identified on weekends through their comparison with OMI and GOME-2A retrievals (not shown). The good agreement between simulated and observed wind suggests that the model horizontal transport error cannot explain such an urban-rural contrast between satellite observations and 36-km REAM simulation results. However, two caveats deserve attention. Firstly, the 36-km REAM cannot resolve urban areas as detailed as the 4-km REAM (Figure 14), and urban and rural regions may coexist in one 36-km grid cell. Secondly, the OMI and GOME-2A pixels can be much larger than 36-km REAM grid cells, possibly leading to more spatially homogenous distributions of satellite NO_2 TVCD data.

3.8 Implications for NO_x emissions

The analysis of section 3.7 indicates that the NEI2011 NO_x emission distributions at 36- and 4-km resolutions are likely biased for the Baltimore-Washington region. The distribution bias of NO_x emission inventories is corroborated by the comparison of the NO_x emission inventory derived from the CONsolidated Community Emissions Processor Tool, Motor Vehicle (CONCEPT MV) v2.1 with that estimated by the Sparse Matrix Operator Kernel Emissions (SMOKE) v3.0 model with the Motor Vehicle Emissions Simulator (MOVES) v2010a (DenBleyker et al., 2012). CONCEPT with finer vehicle activity information as input produced a wider-spread but less-concentrated running exhaust NO_x emissions compared to MOVES in the Denver urban area for July 2008 (DenBleyker et al., 2012). In addition, Canty et al. (2015) found that CMAQ 4.7.1, with on-road emissions from MOVES and off-road emissions from the National Mobile Inventory Model (NMIM), overestimated NO_2 TVCD over urban regions and underestimated NO_2 TVCDs over rural areas in the northeastern U.S. for July and August 2011 compared to the OMNO2 product. The urban-rural contrast was also found in Texas during the 2013 DISCOVER-AQ campaign in the studies of Souri et al. (2016) and Souri et al. (2018), implying distribution uncertainties in NO_x emissions, although these studies and Canty et al. (2015) focused more on polluted regions with overestimated NO_x emissions in their conclusions. The emission distribution bias may also explain why Anderson et al. (2014) have different results from our simulated concentrations in Table 1. In their study, they compared in-situ observations with a nested CMAQ simulation with a resolution of 1.33 km. It is difficult to build up a reliable emission inventory for the whole U.S. at very high resolutions with currently available datasets due to the significant inhomogeneity of NO_x emissions (Marr et al., 2013), but we can still expect significant improvements ~~of~~in the temporal-spatial distributions of NO_x emissions in the near future as GPS-based information start to be used in the NEI estimates (DenBleyker et al., 2017).

Here, we emphasize that our study is not necessarily contradictory to recent studies concerning the overestimation of NEI NO_x emissions (Anderson et al., 2014; Canty et al., 2015; McDonald et al., 2018; Souri et al., 2016; Souri et al., 2018; Travis et al., 2016). Different types of observations in different periods and locations are analyzed for various purposes. This study focuses more on the spatial distribution of NO_x emissions in NEI2011, while previous studies are concerned more about the NO_x emission magnitudes in highly polluted sites, although the spatial distribution issue was also mentioned in some of the studies. If we limit our analyses to those observations in Figures 7, 10, and 12 and the 4-km REAM, we would also conclude an overestimation of NEI NO_x emissions. Considering the significant heterogeneity of NO_x emissions, the spatial distribution of NO_x emissions is a critical factor in evaluating NO_x emissions and improving emission estimation and air quality models, which deserves more attention in future studies, especially when chemical and transport models are moving to higher and higher resolutions.

4 Conclusions

We investigate the diurnal cycles of surface NO_2 concentrations, NO_2 vertical profiles, and NO_2 TVCDs using REAM model simulations on the basis of the observations from air quality monitoring sites, aircraft, Pandora, OMI, and GOME-2A during the DISCOVER-AQ 2011 campaign. We find that WRF simulated nighttime k_{zz}-determined ~~PBLH~~MLHs are significantly lower than ELF lidar measurements. Increasing nighttime mixing from 18:00 – 5:00 LT in the REAM simulations, we significantly improve REAM simulations of nighttime surface NO_2 and O_3 concentrations.

The REAM simulation reproduces well the observed regional mean diurnal cycles of surface NO_2 and NO_y concentrations, NO_2 vertical profiles, and NO_2 TVCDs on weekdays. Observed NO_2 concentrations in the boundary layer and TVCDs on weekends are significantly lower than on weekdays. By specifying a weekend to weekday NO_x emission ratio of 2:3 and applying a less variable NO_x emission diurnal profile on weekends than

772 weekdays, REAM can simulate well the weekend observations. Two issues are also noted. First, Pandora TVCDs
773 show different variations from aircraft-derived and REAM-simulated TVCDs in the early morning and late
774 afternoon, which may be due to the uncertainties of Pandora measurements at large SZAs and the small effective
775 FOV of Pandora. Second, the weekday OMI NO_2 TVCDs derived by NASA are somewhat lower than the KNMI
776 OMI product, P-3B aircraft-derived TVCDs, Pandora, and REAM results; the difference may be caused by the a
777 priori vertical profiles used in the NASA retrieval.

778 While a higher-resolution simulation is assumed to be superior at a priori, the large observation dataset
779 during DISCOVER-AQ 2011 offers the opportunity of a detailed comparison of 4-km and 36-km model
780 simulations. Through the comparison, we find two areas that have not been widely recognized. The first is not
781 using convection parameterization in high-resolution WRF simulations since convection can be resolved
782 explicitly and most convection parameterizations are not designed for high-resolution simulations. We find that
783 4-km WRF tends to overestimate boundary-layer mixing and vertical transport in the late afternoon, leading to a
784 high model bias in simulated NO_2 vertical profiles compared to P-3B aircraft observations. The reasons for this
785 late-afternoon bias in 4-km WRF simulations and model modifications to mitigate this bias need further studies.

786 A second issue is related to the spatial distribution of NO_x emissions in NEI2011. In general, the 4-km
787 simulation results tend to have a high bias relative to the 36-km results on the regional mean observations.
788 However, for individual sites, relative to the 36-km model simulations, the 4-km model results can show larger,
789 smaller, or similar biases compared to the observations depending upon observation location. Based on process
790 diagnostics and analyses, we find that the bias discrepancies between the 36-km and 4-km REAM simulations are
791 mainly attributed to their different NO_x emissions and their spatial gradients at different sites. The comparison of
792 4-km ACAM NO_2 VCD measurements from the UC-12 aircraft with coincident 4-km REAM results shows that
793 4-km REAM NO_2 VCDs are more concentrated in urban regions than the ACAM observations. OMI and GOME-

2A data also show less spatially varying NO_2 TVCD distributions with lower NO_2 TVCDs around the Baltimore-Washington urban regions and higher TVCDs in surrounding rural areas than corresponding 36-km REAM simulation results. Further model analysis indicates that the 36- and 4-km VCD discrepancies are due primarily to the distribution bias of NEI2011 NO_x emissions at 36- and 4-km resolutions. Our results highlight the research need to improve the methodologies and datasets to improve the spatial distributions in emission estimates.

Data availability

The DISCOVER-AQ 2011 campaign datasets are archived on https://www-air.larc.nasa.gov/cgi-bin/ArcView/discover-aq.dc-2011 (last access: March 14, 2021). EPA air quality monitoring datasets are from https://www3.epa.gov/airdata/ (last access: June 23, 2015). The NASA OMI NO_2 product is from https://disc.gsfc.nasa.gov/datasets/OMNO2_003/summary (last access: September 26, 2020). The KNMI OMI NO_2 product is from http://www.temis.nl/airpollution/no2.html (last access: January 14, 2015). We obtain the KNMI GOME-2A NO_2 VCD archives from http://www.temis.nl/airpollution/no2col/no2colgome2_v2.php (last access: January 22, 2015). The GMI MERRA-2 simulation results are from https://portal.nccs.nasa.gov/datashare/dirac/gmidata2/users/mrdamon/Hindcast-Family/HindcastMR2/2011/stations/ (last access: May 14, 2019). We obtain the UC-12 ACAM NO_2 VCD product by X. Liu from https://www-air.larc.nasa.gov/cgi-bin/ArcView/discover-aq.dc-2011?UC12=1#LIU.XIONG/ (last access: December 31, 2019). The Stage IV precipitation data is downloaded from https://rda.ucar.edu/datasets/ds507.5/ (last access: December 28, 2019). The NCEP CFSv2 6-hourly product is available at http://rda.ucar.edu/datasets/ds094.0/ (last access: March 10, 2015). REAM simulation results for this study and the UC-12 ACAM NO_2 VCD product by Lamsal et al. (2017) are available upon request.

Author contribution

JL and YW designed the study. JL, RZ, and CS updated the REAM model. JL conducted model simulations. KFB developed the DOMINO algorithm, CS applied the algorithm to REAM vertical profiles, and JL updated the retrieval algorithm and did the retrieval by using REAM NO_2 vertical profiles. AW, JH, EAC, RWL, JJS, RD, AMT, TNK, LNL, SJJ, MGK, XL, CRN made various measurements in the DISCOVER-AQ 2011 campaign. JL conducted the analyses with discussions with YW, RZ, CS, AW, JH, KFB, EAC, RWL, JJS, RD, AMT, TNK, LNL, SJJ, MGK, XL, and CRN. JL and YW led the writing of the manuscript with inputs from all other coauthors. All coauthors reviewed the manuscript.

Competing interests

The authors declare that they have no conflict of interest.

Acknowledgments

This work was supported by the NASA ACMAP Program. We thank Chun Zhao for providing us the PNNL NEI2011 emission inventory. We thank Yuzhong Zhang and Jenny Fisher for providing the updated GEOS-Chem chemistry mechanism files and thank Yuzhong Zhang, Yongjia Song, Hang Qu, Ye Cheng, Aoxing Zhang, Yufei Zou and Ziming Ke for discussion with J. Li. We thank Susan Strahan for providing the GMI outputs download link.

References

Anderson, D. C., Loughner, C. P., Diskin, G., Weinheimer, A., Canty, T. P., Salawitch, R. J., Worden, H. M., Fried, A., Mikoviny, T., and Wisthaler, A.: Measured and modeled CO and NO_y in DISCOVER-AQ: An evaluation of emissions and chemistry over the eastern US, Atmos. Environ., 96, 78-87, https://doi.org/10.1016/j.atmosenv.2014.07.004, 2014.

Beirle, S., Platt, U., Wenig, M., and Wagner, T.: Weekly cycle of NO_2 by GOME measurements: A signature of anthropogenic sources, Atmos. Chem. Phys., 3, 2225-2232, https://doi.org/10.5194/acp-3-2225-2003, 2003.

Boersma, K. F., Eskes, H. J., Veefkind, J. P., Brinksma, E. J., Van Der A, R. J., Sneep, M., Van Den Oord, G. H. J., Levelt, P. F., Stammes, P., and Gleason, J. F.: Near-real time retrieval of tropospheric NO_2 from OMI, Atmos. Chem. Phys., 7, 2103-2118, https://doi.org/10.5194/acp-7-2103-2007, 2007.

Boersma, K. F., Jacob, D. J., Eskes, H. J., Pinder, R. W., Wang, J., and Van Der A, R. J.: Intercomparison of SCIAMACHY and OMI tropospheric NO_2 columns: Observing the diurnal evolution of chemistry and emissions from space, J. Geophys. Res.-Atmos., 113, https://doi.org/10.1029/2007JD008816, 2008.

Boersma, K. F., Jacob, D. J., Trainic, M., Rudich, Y., De Smedt, I., Dirksen, R., and Eskes, H. J.: Validation of urban NO_2 concentrations and their diurnal and seasonal variations observed from the SCIAMACHY and OMI sensors using in situ surface measurements in Israeli cities, Atmos. Chem. Phys., 9, 3867-3879, https://doi.org/10.5194/acp-9-3867-2009, 2009.

Boersma, K. F., Eskes, H. J., Dirksen, R. J., Veefkind, J. P., Stammes, P., Huijnen, V., Kleipool, Q. L., Sneep, M., Claas, J., and Leitão, J.: An improved tropospheric NO_2 column retrieval algorithm for the Ozone Monitoring Instrument, Atmos. Meas. Tech., 4, 1905-1928, https://doi.org/10.5194/amt-4-1905-2011, 2011.

Boersma, K. F., Eskes, H. J., Richter, A., De Smedt, I., Lorente, A., Beirle, S., van Geffen, J. H., Zara, M., Peters, E., and Roozendael, M. V.: Improving algorithms and uncertainty estimates for satellite NO_2 retrievals: results from the quality assurance for the essential climate variables (QA4ECV) project, Atmos. Meas. Tech., 11, 6651-6678, https://doi.org/10.5194/amt-11-6651-2018, 2018.

Breuer, H., Ács, F., Horváth, Á., Németh, P., and Rajkai, K.: Diurnal course analysis of the WRF-simulated and observation-based planetary boundary layer height, Advances in Science and Research, 11, 83-88, https://doi.org/10.5194/asr-11-83-2014, 2014.

Brohede, S., McLinden, C. A., Berthet, G., Haley, C. S., Murtagh, D., and Sioris, C. E.: A stratospheric NO_2 climatology from Odin/OSIRIS limb-scatter measurements, Can. J. Phys., 85, 1253-1274, https://doi.org/10.1139/p07-141, 2007.

Brown, S. S., Dibb, J. E., Stark, H., Aldener, M., Vozella, M., Whitlow, S., Williams, E. J., Lerner, B. M., Jakoubek, R., and Middlebrook, A. M.: Nighttime removal of NO_x in the summer marine boundary layer, Geophys. Res. Lett., 31, https://doi.org/10.1029/2004GL019412, 2004.

Bucsela, E. J., Krotkov, N. A., Celarier, E. A., Lamsal, L. N., Swartz, W. H., Bhartia, P. K., Boersma, K. F., Veefkind, J. P., Gleason, J. F., and Pickering, K. E.: A new stratospheric and tropospheric NO_2 retrieval algorithm for nadir-

viewing satellite instruments: applications to OMI, Atmos. Meas. Tech., 6, 2607-2626, https://doi.org/10.5194/amt-6-2607-2013, 2013.

Canty, T., Hembeck, L., Vinciguerra, T., Goldberg, D., Carpenter, S., Allen, D., Loughner, C., Salawitch, R., and Dickerson, R.: Ozone and NO_x chemistry in the eastern US: evaluation of CMAQ/CB05 with satellite (OMI) data, Atmos. Chem. Phys., 15, 10965, https://doi.org/10.5194/acp-15-10965-2015, 2015.

Chance, K.: OMI Algorithm Theoretical Basis Document: OMI Trace Gas Algorithms, available at https://ozoneaq.gsfc.nasa.gov/media/docs/ATBD-OMI-04.pdf, Smithsonian Astrophysical Observatory, Cambridge, MA, USA2.0, 78, 2002.

Cheng, Y., Wang, Y., Zhang, Y., Chen, G., Crawford, J. H., Kleb, M. M., Diskin, G. S., and Weinheimer, A. J.: Large biogenic contribution to boundary layer O_3-CO regression slope in summer, Geophys. Res. Lett., 44, 7061-7068, https://doi.org/10.1002/2017GL074405, 2017.

Cheng, Y., Wang, Y., Zhang, Y., Crawford, J. H., Diskin, G. S., Weinheimer, A. J., and Fried, A.: Estimator of surface ozone using formaldehyde and carbon monoxide concentrations over the eastern United States in summer, J. Geophys. Res.-Atmos., 123, 7642-7655, https://doi.org/10.1029/2018JD028452, 2018.

Choi, S., Lamsal, L. N., Follette-Cook, M., Joiner, J., Krotkov, N. A., Swartz, W. H., Pickering, K. E., Loughner, C. P., Appel, W., Pfister, G., Saide, P. E., Cohen, R. C., Weinheimer, A. J., and Herman, J. R.: Assessment of NO_2 observations during DISCOVER-AQ and KORUS-AQ field campaigns, Atmos. Meas. Tech., 13, 2523-2546, https://doi.org/10.5194/amt-13-2523-2020, 2020.

Choi, Y., Wang, Y., Zeng, T., Cunnold, D., Yang, E. S., Martin, R., Chance, K., Thouret, V., and Edgerton, E.: Springtime transitions of NO_2, CO, and O_3 over North America: Model evaluation and analysis, J. Geophys. Res.-Atmos., 113, https://doi.org/10.1029/2007JD009632, 2008.

Choi, Y., Kim, H., Tong, D., and Lee, P.: Summertime weekly cycles of observed and modeled NO_x and O_3 concentrations as a function of satellite-derived ozone production sensitivity and land use types over the Continental United States, Atmos. Chem. Phys., 12, 6291-6307, https://doi.org/10.5194/acp-12-6291-2012, 2012.

Compton, J. C., Delgado, R., Berkoff, T. A., and Hoff, R. M.: Determination of planetary boundary layer height on short spatial and temporal scales: A demonstration of the covariance wavelet transform in ground-based wind profiler and lidar measurements, Journal of Atmospheric and Oceanic Technology, 30, 1566-1575, https://doi.org/10.1175/JTECH-D-12-00116.1, 2013.

David, L. M., and Nair, P. R.: Diurnal and seasonal variability of surface ozone and NO_x at a tropical coastal site: Association with mesoscale and synoptic meteorological conditions, J. Geophys. Res.-Atmos., 116, https://doi.org/10.1029/2010JD015076, 2011.

Davis, C., Brown, B., and Bullock, R.: Object-based verification of precipitation forecasts. Part I: Methodology and application to mesoscale rain areas, Monthly Weather Review, 134, 1772-1784, https://doi.org/10.1175/MWR3145.1, 2006.

Day, D. A., Wooldridge, P. J., Dillon, M. B., Thornton, J. A., and Cohen, R. C.: A thermal dissociation laser - induced fluorescence instrument for in situ detection of NO_2, peroxy nitrates, alkyl nitrates, and HNO_3, J. Geophys. Res.-Atmos., 107, ACH 4-1-ACH 4-14, https://doi.org/10.1029/2001JD000779, 2002.

de Foy, B.: City-level variations in NOx emissions derived from hourly monitoring data in Chicago, Atmos. Environ., 176, 128-139, https://doi.org/10.1016/j.atmosenv.2017.12.028, 2018.

DenBleyker, A., Morris, R. E., Lindhjem, C. E., Parker, L. K., Shah, T., Koo, B., Loomis, C., and Dilly, J.: Temporal and Spatial Detail in Mobile Source Emission Inventories for Regional Air Quality Modeling, 2012 International Emission Inventory Conference, Florida, U.S., August 13 - 16, 2012, 2012.

DenBleyker, A., Koupal, J., DeFries, T., and Palacios, C.: Improvement of Default Inputs for MOVES and SMOKE-MOVES: CRC Project A-100, available at https://crcao.org/reports/recentstudies2017/A-100/ERG_FinalReport_CRCA100_28Feb2017.pdf, Eastern Research Group, Inc., Austin, TX, 86, 2017.

Dirksen, R. J., Boersma, K. F., Eskes, H. J., Ionov, D. V., Bucsela, E. J., Levelt, P. F., and Kelder, H. M.: Evaluation of stratospheric NO_2 retrieved from the Ozone Monitoring Instrument: Intercomparison, diurnal cycle, and trending, J. Geophys. Res.-Atmos., 116, https://doi.org/10.1029/2010JD014943, 2011.

EPA: Profile of the 2011 National Air Emissions Inventory, available at https://www.epa.gov/sites/production/files/2015-08/documents/lite_finalversion_ver10.pdf, U.S. Environmental Protection Agency, 2014.

Fisher, J. A., Jacob, D. J., Travis, K. R., Kim, P. S., Marais, E. A., Chan Miller, C., Yu, K., Zhu, L., Yantosca, R. M., and Sulprizio, M. P.: Organic nitrate chemistry and its implications for nitrogen budgets in an isoprene-and monoterpene-rich atmosphere: constraints from aircraft ($SEAC^4RS$) and ground-based (SOAS) observations in the Southeast US, Atmos. Chem. Phys., 16, 5969-5991, https://doi.org/10.5194/acp-16-5969-2016, 2016.

Flynn, C. M., Pickering, K. E., Crawford, J. H., Lamsal, L., Krotkov, N., Herman, J., Weinheimer, A., Chen, G., Liu, X., and Szykman, J.: Relationship between column-density and surface mixing ratio: Statistical analysis of O_3 and NO_2 data from the July 2011 Maryland DISCOVER-AQ mission, Atmos. Environ., 92, 429-441, https://doi.org/10.1016/j.atmosenv.2014.04.041, 2014.

Frey, M. M., Brough, N., France, J. L., Anderson, P. S., Traulle, O., King, M. D., Jones, A. E., Wolff, E. W., and Savarino, J.: The diurnal variability of atmospheric nitrogen oxides (NO and NO_2) above the Antarctic Plateau driven by atmospheric stability and snow emissions, Atmos. Chem. Phys., 13, 3045-3062, https://doi.org/10.5194/acp-13-3045-2013, 2013.

Gaur, A., Tripathi, S. N., Kanawade, V. P., Tare, V., and Shukla, S. P.: Four-year measurements of trace gases (SO_2, NO_x, CO, and O_3) at an urban location, Kanpur, in Northern India, Journal of Atmospheric Chemistry, 71, 283-301, https://doi.org/10.1007/s10874-014-9295-8, 2014.

Gourley, J. J., Hong, Y., Flamig, Z. L., Wang, J., Vergara, H., and Anagnostou, E. N.: Hydrologic evaluation of rainfall estimates from radar, satellite, gauge, and combinations on Ft. Cobb basin, Oklahoma, Journal of Hydrometeorology, 12, 973-988, https://doi.org/10.1175/2011JHM1287.1, 2011.

Guenther, A. B., Jiang, X., Heald, C. L., Sakulyanontvittaya, T., Duhl, T., Emmons, L. K., and Wang, X.: The Model of Emissions of Gases and Aerosols from Nature version 2.1 (MEGAN2.1): an extended and updated framework for modeling biogenic emissions, Geosci. Model Dev., 5, 1471-1492, https://doi.org/10.5194/gmd-5-1471-2012, 2012.

Hains, J. C., Boersma, K. F., Kroon, M., Dirksen, R. J., Cohen, R. C., Perring, A. E., Bucsela, E., Volten, H., Swart, D. P. J., and Richter, A.: Testing and improving OMI DOMINO tropospheric NO_2 using observations from the DANDELIONS and INTEX - B validation campaigns, J. Geophys. Res.-Atmos., 115, https://doi.org/10.1029/2009JD012399, 2010.

Herman, J., Cede, A., Spinei, E., Mount, G., Tzortziou, M., and Abuhassan, N.: NO_2 column amounts from ground-based Pandora and MFDOAS spectrometers using the direct-Sun DOAS technique: Intercomparisons and application to OMI validation, J. Geophys. Res.-Atmos., 114, https://doi.org/10.1029/2009JD011848, 2009.

Herman, J., Spinei, E., Fried, A., Kim, J., Kim, J., Kim, W., Cede, A., Abuhassan, N., and Segal-Rozenhaimer, M.: NO_2 and HCHO measurements in Korea from 2012 to 2016 from Pandora spectrometer instruments compared with OMI retrievals and with aircraft measurements during the KORUS-AQ campaign, Atmos. Meas. Tech., 11, 4583-4603, https://doi.org/10.5194/amt-11-4583-2018, 2018.

Herman, J., Abuhassan, N., Kim, J., Kim, J., Dubey, M., Raponi, M., and Tzortziou, M.: Underestimation of column NO_2 amounts from the OMI satellite compared to diurnally varying ground-based retrievals from multiple PANDORA spectrometer instruments, Atmos. Meas. Tech., 12, 5593-5612, https://doi.org/10.5194/amt-12-5593-2019, 2019.

Hong, S.-Y., Noh, Y., and Dudhia, J.: A new vertical diffusion package with an explicit treatment of entrainment processes, Monthly weather review, 134, 2318-2341, https://doi.org/10.1175/MWR3199.1, 2006.

Hu, X., Doughty, D. C., Sanchez, K. J., Joseph, E., and Fuentes, J. D.: Ozone variability in the atmospheric boundary layer in Maryland and its implications for vertical transport model, Atmos. Environ., 46, 354-364, https://doi.org/10.1016/j.atmosenv.2011.09.054, 2012.

Huijnen, V., Eskes, H. J., Poupkou, A., Elbern, H., Boersma, K. F., Foret, G., Sofiev, M., Valdebenito, A., Flemming, J., and Stein, O.: Comparison of OMI NO_2 tropospheric columns with an ensemble of global and European regional air quality models, Atmos. Chem. Phys., 10, 3273-3296, https://doi.org/10.5194/acp-10-3273-2010, 2010.

Ionov, D. V., Timofeyev, Y. M., Sinyakov, V. P., Semenov, V. K., Goutail, F., Pommereau, J. P., Bucsela, E. J., Celarier, E. A., and Kroon, M.: Ground - based validation of EOS - Aura OMI NO_2 vertical column data in the midlatitude mountain ranges of Tien Shan (Kyrgyzstan) and Alps (France), J. Geophys. Res.-Atmos., 113, https://doi.org/10.1029/2007JD008659, 2008.

Irie, H., Kanaya, Y., Akimoto, H., Tanimoto, H., Wang, Z., Gleason, J. F., and Bucsela, E. J.: Validation of OMI tropospheric NO_2 column data using MAX-DOAS measurements deep inside the North China Plain in June 2006: Mount Tai Experiment 2006, Atmos. Chem. Phys., 8, 6577-6586, https://doi.org/10.5194/acp-8-6577-2008, 2008.

Irie, H., Boersma, K. F., Kanaya, Y., Takashima, H., Pan, X., and Wang, Z.: Quantitative bias estimates for tropospheric NO_2 columns retrieved from SCIAMACHY, OMI, and GOME-2 using a common standard for East Asia, Atmos. Meas. Tech., 5, 2403-2411, https://doi.org/10.5194/amt-5-2403-2012, 2012.

969 Jones, A. E., Weller, R., Wolff, E. W., and Jacobi, H. W.: Speciation and rate of photochemical NO and NO_2
970 production in Antarctic snow, Geophys. Res. Lett., 27, 345-348, https://doi.org/10.1029/1999GL010885, 2000.

971 Judd, L. M., Al-Saadi, J. A., Valin, L. C., Pierce, R. B., Yang, K., Janz, S. J., Kowalewski, M. G., Szykman, J. J.,
972 Tiefengraber, M., and Mueller, M.: The Dawn of Geostationary Air Quality Monitoring: Case Studies from Seoul and
973 Los Angeles, Front. Environ. Sci., 6, 85, https://doi.org/10.3389/fenvs.2018.00085, 2018.

974 Judd, L. M., Al-Saadi, J. A., Janz, S. J., Kowalewski, M. G., Pierce, R. B., Szykman, J. J., Valin, L. C., Swap, R.,
975 Cede, A., Mueller, M., Tiefengraber, M., Abuhassan, N., and Williams, D.: Evaluating the impact of spatial resolution
976 on tropospheric NO_2 column comparisons within urban areas using high-resolution airborne data, Atmos. Meas. Tech.,
977 12, 6091-6111, https://doi.org/10.5194/amt-12-6091-2019, 2019.

978 Judd, L. M., Al-Saadi, J. A., Szykman, J. J., Valin, L. C., Janz, S. J., Kowalewski, M. G., Eskes, H. J., Veefkind, J. P.,
979 Cede, A., Mueller, M., Gebetsberger, M., Swap, R., Pierce, R. B., Nowlan, C. R., Abad, G. G., Nehrir, A., and
980 Williams, D.: Evaluating Sentinel-5P TROPOMI tropospheric NO_2 column densities with airborne and Pandora
981 spectrometers near New York City and Long Island Sound, Atmos. Meas. Tech. ~~Discuss., 2020, 1-52~~, 13, 6113-6140,
982 https://doi.org/10.5194/amt-13-6113-2020~~-151~~, 2020.

983 Kalinga, O. A., and Gan, T. Y.: Estimation of rainfall from infrared - microwave satellite data for basin - scale
984 hydrologic modelling, Hydrological processes, 24, 2068-2086, https://doi.org/10.1002/hyp.7626, 2010.

985 Kaynak, B., Hu, Y., Martin, R. V., Sioris, C. E., and Russell, A. G.: Comparison of weekly cycle of NO_2 satellite
986 retrievals and NO_x emission inventories for the continental United States, J. Geophys. Res.-Atmos., 114,
987 https://doi.org/10.1029/2008JD010714, 2009.

988 Kim, S. W., McDonald, B., Baidar, S., Brown, S., Dube, B., Ferrare, R., Frost, G., Harley, R., Holloway, J., and Lee,
989 H. J.: Modeling the weekly cycle of NO_x and CO emissions and their impacts on O_3 in the Los Angeles-South Coast
990 Air Basin during the CalNex 2010 field campaign, J. Geophys. Res.-Atmos., 121, 1340-1360,
991 https://doi.org/10.1002/2015JD024292, 2016.

992 Knepp, T., Pippin, M., Crawford, J., Chen, G., Szykman, J., Long, R., Cowen, L., Cede, A., Abuhassan, N., and
993 Herman, J.: Estimating surface NO_2 and SO_2 mixing ratios from fast-response total column observations and potential
994 application to geostationary missions, Journal of atmospheric chemistry, 72, 261-286, https://doi.org/10.1007/s10874-
995 013-9257-6, 2015.

996 Knepp, T. N., Szykman, J. J., Long, R., Duvall, R. M., Krug, J., Beaver, M., Cavender, K., Kronmiller, K., Wheeler,
997 M., and Delgado, R.: Assessment of mixed-layer height estimation from single-wavelength ceilometer profiles, Atmos.
998 Meas. Tech., 10, 3963-3983, https://doi.org/10.5194/amt-10-3963-2017, 2017.

999 Kollonige, D. E., Thompson, A. M., Josipovic, M., Tzortziou, M., Beukes, J. P., Burger, R., Martins, D. K., van Zyl, P.
1000 G., Vakkari, V., and Laakso, L.: OMI Satellite and Ground - Based Pandora Observations and Their Application to
1001 Surface NO_2 Estimations at Terrestrial and Marine Sites, J. Geophys. Res.-Atmos., 123, 1441-1459,
1002 https://doi.org/10.1002/2017JD026518, 2018.

Krotkov, N. A., Lamsal, L. N., Celarier, E. A., Swartz, W. H., Marchenko, S. V., Bucsela, E. J., Chan, K. L., Wenig, M., and Zara, M.: The version 3 OMI NO_2 standard product, Atmos. Meas. Tech., 10, 3133-3149, https://doi.org/10.5194/amt-10-3133-2017, 2017.

Lamsal, L. N., Krotkov, N. A., Celarier, E. A., Swartz, W. H., Pickering, K. E., Bucsela, E. J., Gleason, J. F., Martin, R. V., Philip, S., and Irie, H.: Evaluation of OMI operational standard NO_2 column retrievals using in situ and surface-based NO_2 observations, Atmos. Chem. Phys., 14, 11587-11609, https://doi.org/10.5194/acp-14-11587-2014, 2014.

Lamsal, L. N., Duncan, B. N., Yoshida, Y., Krotkov, N. A., Pickering, K. E., Streets, D. G., and Lu, Z.: US NO_2 trends (2005–2013): EPA Air Quality System (AQS) data versus improved observations from the Ozone Monitoring Instrument (OMI), Atmos. Environ., 110, 130-143, https://doi.org/10.1016/j.atmosenv.2015.03.055, 2015.

Lamsal, L. N., Janz, S. J., Krotkov, N. A., Pickering, K. E., Spurr, R. J. D., Kowalewski, M. G., Loughner, C. P., Crawford, J. H., Swartz, W. H., and Herman, J.: High‐resolution NO_2 observations from the Airborne Compact Atmospheric Mapper: Retrieval and validation, J. Geophys. Res.-Atmos., 122, 1953-1970, https://doi.org/10.1002/2016JD025483, 2017.

Lamsal, L. N., Krotkov, N. A., Vasilkov, A., Marchenko, S., Qin, W., Yang, E. S., Fasnacht, Z., Joiner, J., Choi, S., Haffner, D., Swartz, W. H., Fisher, B., and Bucsela, E.: Ozone Monitoring Instrument (OMI~~/~~) Aura ~~Nitrogen Dioxide Standard Product~~nitrogen dioxide standard product version 4.0 with i~~I~~mproved s~~S~~urface and c~~C~~loud t~~T~~reatments, Atmos. Meas. Tech.~~ Discuss., 2020, 1-56~~, 14, 455-479, https://doi.org/10.5194/amt-~~2020-200, 2020~~14-455-2021, 2021.

Levelt, P. F., Hilsenrath, E., Leppelmeier, G. W., van den Oord, G. H. J., Bhartia, P. K., Tamminen, J., de Haan, J. F., and Veefkind, J. P.: Science objectives of the ozone monitoring instrument, IEEE Transactions on Geoscience and Remote Sensing, 44, 1199-1208, https://doi.org/10.1109/TGRS.2006.872336, 2006.

Li, J., Wang, Y., and Qu, H.: Dependence of summertime surface ozone on NO_x and VOC emissions over the United States: Peak time and value, Geophys. Res. Lett., 46, 3540-3550, https://doi.org/10.1029/2018GL081823, 2019.

Lin, Y., and Mitchell, K. E.: the NCEP stage II/IV hourly precipitation analyses: Development and applications, 19th Conf. Hydrology, American Meteorological Society, San Diego, CA, USA, 2005,

Liu, C., Liu, X., Kowalewski, M., Janz, S., González Abad, G., Pickering, K., Chance, K., and Lamsal, L.: Analysis of ACAM data for trace gas retrievals during the 2011 DISCOVER-AQ campaign, Journal of Spectroscopy, 2015, https://doi.org/10.1155/2015/827160, 2015a.

Liu, C., Liu, X., Kowalewski, M. G., Janz, S. J., González Abad, G., Pickering, K. E., Chance, K., and Lamsal, L. N.: Characterization and verification of ACAM slit functions for trace-gas retrievals during the 2011 DISCOVER-AQ flight campaign, Atmos. Meas. Tech., 8, 751-759, https://doi.org/10.5194/amt-8-751-2015, 2015b.

Liu, Z., Wang, Y., Gu, D., Zhao, C., Huey, L. G., Stickel, R., Liao, J., Shao, M., Zhu, T., and Zeng, L.: Summertime photochemistry during CAREBeijing-2007: RO_x budgets and O_3 formation, Atmos. Chem. Phys., 12, 7737-7752, https://doi.org/10.5194/acp-12-7737-2012, 2012.

Lopez, P.: Direct 4D-Var assimilation of NCEP stage IV radar and gauge precipitation data at ECMWF, Monthly Weather Review, 139, 2098-2116, https://doi.org/10.1175/2010MWR3565.1, 2011.

Luo, G., Yu, F., and Schwab, J.: Revised treatment of wet scavenging processes dramatically improves GEOS-Chem 12.0.0 simulations of surface nitric acid, nitrate, and ammonium over the United States, Geosci. Model Dev., 12, 3439-3447, https://doi.org/10.5194/gmd-12-3439-2019, 2019.

Marchenko, S., Krotkov, N., Lamsal, L., Celarier, E., Swartz, W., and Bucsela, E.: Revising the slant column density retrieval of nitrogen dioxide observed by the Ozone Monitoring Instrument, J. Geophys. Res.-Atmos., 120, 5670-5692, https://doi.org/10.1002/2014JD022913, 2015.

Marr, L. C., Moore, T. O., Klapmeyer, M. E., and Killar, M. B.: Comparison of NO_x Fluxes Measured by Eddy Covariance to Emission Inventories and Land Use, Environ. Sci. Technol., 47, 1800-1808, https://doi.org/10.1021/es303150y, 2013.

McDonald, B., McKeen, S., Cui, Y. Y., Ahmadov, R., Kim, S.-W., Frost, G. J., Pollack, I., Peischl, J., Ryerson, T. B., and Holloway, J.: Modeling Ozone in the Eastern US using a Fuel-Based Mobile Source Emissions Inventory, Environ. Sci. Technol., https://doi.org/10.1021/acs.est.8b00778, 2018.

Munro, R., Eisinger, M., Anderson, C., Callies, J., Corpaccioli, E., Lang, R., Lefebvre, A., Livschitz, Y., and Albinana, A. P.: GOME-2 on MetOp, Proc. of The 2006 EUMETSAT Meteorological Satellite Conference, Helsinki, Finland, 2006, 48,

Nelson, B. R., Prat, O. P., Seo, D.-J., and Habib, E.: Assessment and implications of NCEP Stage IV quantitative precipitation estimates for product intercomparisons, Weather and Forecasting, 31, 371-394, https://doi.org/10.1175/WAF-D-14-00112.1, 2016.

Ng, N. L., Brown, S. S., Archibald, A. T., Atlas, E., Cohen, R. C., Crowley, J. N., Day, D. A., Donahue, N. M., Fry, J. L., and Fuchs, H.: Nitrate radicals and biogenic volatile organic compounds: oxidation, mechanisms, and organic aerosol, Atmos. Chem. Phys., 17, 2103-2162, https://doi.org/10.5194/acp-17-2103-2017, 2017.

Nowlan, C. R., Liu, X., Leitch, J. W., Chance, K., González Abad, G., Liu, C., Zoogman, P., Cole, J., Delker, T., Good, W., Murcray, F., Ruppert, L., Soo, D., Follette-Cook, M. B., Janz, S. J., Kowalewski, M. G., Loughner, C. P., Pickering, K. E., Herman, J. R., Beaver, M. R., Long, R. W., Szykman, J. J., Judd, L. M., Kelley, P., Luke, W. T., Ren, X., and Al-Saadi, J. A.: Nitrogen dioxide observations from the Geostationary Trace gas and Aerosol Sensor Optimization (GeoTASO) airborne instrument: Retrieval algorithm and measurements during DISCOVER-AQ Texas 2013, Atmos. Meas. Tech., 9, 2647-2668, https://doi.org/10.5194/amt-9-2647-2016, 2016.

Nowlan, C. R., Liu, X., Janz, S. J., Kowalewski, M. G., Chance, K., Follette-Cook, M. B., Fried, A., González Abad, G., Herman, J. R., Judd, L. M., Kwon, H. A., Loughner, C. P., Pickering, K. E., Richter, D., Spinei, E., Walega, J., Weibring, P., and Weinheimer, A. J.: Nitrogen dioxide and formaldehyde measurements from the GEOstationary Coastal and Air Pollution Events (GEO-CAPE) Airborne Simulator over Houston, Texas, Atmos. Meas. Tech., 11, 5941-5964, https://doi.org/10.5194/amt-11-5941-2018, 2018.

Oetjen, H., Baidar, S., Krotkov, N. A., Lamsal, L. N., Lechner, M., and Volkamer, R.: Airborne MAX-DOAS measurements over California: Testing the NASA OMI tropospheric NO_2 product, J. Geophys. Res.-Atmos., 118, 7400-7413, https://doi.org/10.1002/jgrd.50550, 2013.

Peng, J., Hu, M., Guo, S., Du, Z., Zheng, J., Shang, D., Zamora, M. L., Zeng, L., Shao, M., and Wu, Y.-S.: Markedly enhanced absorption and direct radiative forcing of black carbon under polluted urban environments, Proc. Natl. Acad. Sci. U.S.A., 201602310, https://doi.org/10.1073/pnas.1602310113, 2016.

Peters, E., Wittrock, F., Großmann, K., Frieß, U., Richter, A., and Burrows, J. P.: Formaldehyde and nitrogen dioxide over the remote western Pacific Ocean: SCIAMACHY and GOME-2 validation using ship-based MAX-DOAS observations, Atmos. Chem. Phys., 12, 11179-11197, https://doi.org/10.5194/acp-12-11179-2012, 2012.

Reddy, B. S. K., Kumar, K. R., Balakrishnaiah, G., Gopal, K. R., Reddy, R. R., Sivakumar, V., Lingaswamy, A. P., Arafath, S. M., Umadevi, K., and Kumari, S. P.: Analysis of diurnal and seasonal behavior of surface ozone and its precursors (NO_x) at a semi-arid rural site in Southern India, Aerosol Air Qual Res, 12, 1081-1094, https://doi.org/10.4209/aaqr.2012.03.0055 2012.

Reed, A. J., Thompson, A. M., Kollonige, D. E., Martins, D. K., Tzortziou, M. A., Herman, J. R., Berkoff, T. A., Abuhassan, N. K., and Cede, A.: Effects of local meteorology and aerosols on ozone and nitrogen dioxide retrievals from OMI and pandora spectrometers in Maryland, USA during DISCOVER-AQ 2011, Journal of atmospheric chemistry, 72, 455-482, https://doi.org/10.1007/s10874-013-9254-9, 2015.

Reed, C., Evans, M. J., Carlo, P. D., Lee, J. D., and Carpenter, L. J.: Interferences in photolytic NO_2 measurements: explanation for an apparent missing oxidant?, Atmos. Chem. Phys., 16, 4707-4724, https://doi.org/10.5194/acp-16-4707-2016, 2016.

Richter, A., Begoin, M., Hilboll, A., and Burrows, J. P.: An improved NO_2 retrieval for the GOME-2 satellite instrument, Atmos. Meas. Tech., 4, 1147-1159, https://doi.org/10.5194/amt-4-1147-2011, 2011.

Russell, A. R., Valin, L. C., and Cohen, R. C.: Trends in OMI NO_2 observations over the United States: effects of emission control technology and the economic recession, Atmos. Chem. Phys., 12, 12197-12209, https://doi.org/10.5194/acp-12-12197-2012, 2012.

Saha, S., Moorthi, S., Wu, X., Wang, J., Nadiga, S., Tripp, P., Behringer, D., Hou, Y. T., Chuang, H.-y., and Iredell, M.: NCEP climate forecast system version 2 (CFSv2) 6-hourly products, available at https://rda.ucar.edu/datasets/ds094.0/, https://doi.org/10.5065/D61C1TXF, 2011 (last access: Mar 10, 2015).

Sawamura, P., Müller, D., Hoff, R. M., Hostetler, C. A., Ferrare, R. A., Hair, J. W., Rogers, R. R., Anderson, B. E., Ziemba, L. D., and Beyersdorf, A. J.: Aerosol optical and microphysical retrievals from a hybrid multiwavelength lidar data set–DISCOVER-AQ 2011, Atmos. Meas. Tech., 7, 3095-3112, https://doi.org/10.5194/amt-7-3095-2014, 2014.

Seinfeld, J. H., and Pandis, S. N.: Atmospheric chemistry and physics: from air pollution to climate change, John Wiley & Sons, Inc, Hoboken, New Jersey, 2016.

Sen, B., Toon, G. C., Osterman, G. B., Blavier, J.-F., Margitan, J. J., Salawitch, R. J., and Yue, G. K.: Measurements of reactive nitrogen in the stratosphere, J. Geophys. Res.-Atmos., 103, 3571-3585, https://doi.org/10.1029/97JD02468, 1998.

Shin, H. H., and Hong, S.-Y.: Intercomparison of planetary boundary-layer parametrizations in the WRF model for a single day from CASES-99, Boundary-Layer Meteorology, 139, 261-281, https://doi.org/10.1007/s10546-010-9583-z, 2011.

Silvern, R. F., Jacob, D. J., Mickley, L. J., Sulprizio, M. P., Travis, K. R., Marais, E. A., Cohen, R. C., Laughner, J. L., Choi, S., Joiner, J., and Lamsal, L. N.: Using satellite observations of tropospheric NO_2 columns to infer long-term trends in US NO_x emissions: the importance of accounting for the free tropospheric NO_2 background, Atmos. Chem. Phys., 19, 8863-8878, https://doi.org/10.5194/acp-19-8863-2019, 2019.

Souri, A. H., Choi, Y., Jeon, W., Li, X., Pan, S., Diao, L., and Westenbarger, D. A.: Constraining NO_x emissions using satellite NO_2 measurements during 2013 DISCOVER-AQ Texas campaign, Atmos. Environ., 131, 371-381, https://doi.org/10.1016/j.atmosenv.2016.02.020, 2016.

Souri, A. H., Choi, Y., Pan, S., Curci, G., Nowlan, C. R., Janz, S. J., Kowalewski, M. G., Liu, J., Herman, J. R., and Weinheimer, A. J.: First top‐down estimates of anthropogenic NO_x emissions using high‐resolution airborne remote sensing observations, J. Geophys. Res.-Atmos., 123, 3269-3284, https://doi.org/10.1002/2017JD028009, 2018.

Spinei, E., Cede, A., Swartz, W. H., Herman, J., and Mount, G. H.: The use of NO_2 absorption cross section temperature sensitivity to derive NO_2 profile temperature and stratospheric–tropospheric column partitioning from visible direct-sun DOAS measurements, Atmos. Meas. Tech., 7, 4299-4316, https://doi.org/10.5194/amt-7-4299-2014, 2014.

Spurr, R.: LIDORT and VLIDORT: Linearized pseudo-spherical scalar and vector discrete ordinate radiative transfer models for use in remote sensing retrieval problems, in: Light Scattering Reviews 3, Springer, 229-275, 2008.

Thompson, A. M., Stauffer, R. M., Boyle, T. P., Kollonige, D. E., Miyazaki, K., Tzortziou, M., Herman, J. R., Abuhassan, N., Jordan, C. E., and Lamb, B. T.: Comparison of Near‐Surface NO_2 Pollution With Pandora Total Column NO_2 During the Korea‐United States Ocean Color (KORUS OC) Campaign, J. Geophys. Res.-Atmos., 124, 13560-13575, https://doi.org/10.1029/2019JD030765, 2019.

Thornton, J. A., Wooldridge, P. J., and Cohen, R. C.: Atmospheric NO_2: In situ laser-induced fluorescence detection at parts per trillion mixing ratios, Anal. Chem., 72, 528-539, https://doi.org/10.1021/ac9908905, 2000.

Tong, D., Lamsal, L., Pan, L., Ding, C., Kim, H., Lee, P., Chai, T., Pickering, K. E., and Stajner, I.: Long-term NO_x trends over large cities in the United States during the great recession: Comparison of satellite retrievals, ground observations, and emission inventories, Atmos. Environ., 107, 70-84, https://doi.org/10.1016/j.atmosenv.2015.01.035, 2015.

Travis, K. R., Jacob, D. J., Fisher, J. A., Kim, P. S., Marais, E. A., Zhu, L., Yu, K., Miller, C. C., Yantosca, R. M., and Sulprizio, M. P.: Why do models overestimate surface ozone in the Southeast United States?, Atmos. Chem. Phys., 16, 13561-13577, https://doi.org/10.5194/acp-16-13561-2016, 2016.

Tu, J., Xia, Z.-G., Wang, H., and Li, W.: Temporal variations in surface ozone and its precursors and meteorological effects at an urban site in China, Atmospheric Research, 85, 310-337, https://doi.org/10.1016/j.atmosres.2007.02.003, 2007.

Valin, L. C., Russell, A. R., Hudman, R. C., and Cohen, R. C.: Effects of model resolution on the interpretation of satellite NO_2 observations, Atmos. Chem. Phys., 11, 11647-11655, https://doi.org/10.5194/acp-11-11647-2011, 2011.

van der A, R. J., Eskes, H. J., Roozendael, M. V., De Smedt, I., Blond, N., Boersma, F., Weiss, A., and van Peet, J. C. A.: Algorithm Document Tropospheric NO_2, available at http://www.temis.nl/docs/AD_NO2.pdf1.0, 23, 2010.

Van Geffen, J., Boersma, K., Van Roozendael, M., Hendrick, F., Mahieu, E., De Smedt, I., Sneep, M., and Veefkind, J.: Improved spectral fitting of nitrogen dioxide from OMI in the 405–465 nm window, Atmos. Meas. Tech., 8, 1685-1699, https://doi.org/10.5194/amt-8-1685-2015, 2015.

Van Stratum, B. J. H., Vilà-Guerau de Arellano, J., Ouwersloot, H. G., Dries, K. d., Van Laar, T. W., Martinez, M., Lelieveld, J., Diesch, J.-M., Drewnick, F., and Fischer, H.: Case study of the diurnal variability of chemically active species with respect to boundary layer dynamics during DOMINO, Atmos. Chem. Phys., 12, 5329-5341, https://doi.org/10.5194/acp-12-5329-2012, 2012.

Wooldridge, P. J., Perring, A. E., Bertram, T. H., Flocke, F. M., Roberts, J. M., Singh, H. B., Huey, L. G., Thornton, J. A., Wolfe, G. M., and Murphy, J. G.: Total Peroxy Nitrates ([Sigma] PNs) in the atmosphere: the Thermal Dissociation-Laser Induced Fluorescence (TD-LIF) technique and comparisons to speciated PAN measurements, Atmos. Meas. Tech., 3, 593, https://doi.org/10.5194/amt-3-593-2010, 2010.

Yuan, H., McGinley, J. A., Schultz, P. J., Anderson, C. J., and Lu, C.: Short-range precipitation forecasts from time-lagged multimodel ensembles during the HMT-West-2006 campaign, Journal of Hydrometeorology, 9, 477-491, https://doi.org/10.1175/2007JHM879.1, 2008.

Zhang, R., Wang, Y., Smeltzer, C., Qu, H., Koshak, W., and Boersma, K. F.: Comparing OMI-based and EPA AQS in situ NO_2 trends: towards understanding surface NO_x emission changes, Atmos. Meas. Tech., 11, 3955-3967, https://doi.org/10.5194/amt-11-3955-2018, 2018.

Zhang, Y., and Wang, Y.: Climate-driven ground-level ozone extreme in the fall over the Southeast United States, Proc. Natl. Acad. Sci. U.S.A., 113, 10025-10030, https://doi.org/10.1073/pnas.1602563113, 2016.

Zhang, Y., Wang, Y., Chen, G., Smeltzer, C., Crawford, J., Olson, J., Szykman, J., Weinheimer, A. J., Knapp, D. J., and Montzka, D. D.: Large vertical gradient of reactive nitrogen oxides in the boundary layer: Modeling analysis of DISCOVER‐AQ 2011 observations, J. Geophys. Res.-Atmos., 121, 1922-1934, https://doi.org/10.1002/2015JD024203, 2016.

Zhao, C., Wang, Y., Choi, Y., and Zeng, T.: Summertime impact of convective transport and lightning NO_x production over North America: modeling dependence on meteorological simulations, Atmos. Chem. Phys., 9, 4315-4327, https://doi.org/10.5194/acp-9-4315-2009, 2009.

Zhao, X., Griffin, D., Fioletov, V., McLinden, C., Davies, J., Ogyu, A., Lee, S. C., Lupu, A., Moran, M. D., Cede, A., Tiefengraber, M., and Müller, M.: Retrieval of total column and surface NO_2 from Pandora zenith-sky measurements, Atmos. Chem. Phys., 19, 10619-10642, https://doi.org/10.5194/acp-19-10619-2019, 2019.

Zhao, X., Griffin, D., Fioletov, V., McLinden, C., Cede, A., Tiefengraber, M., Müller, M., Bognar, K., Strong, K., Boersma, F., Eskes, H., Davies, J., Ogyu, A., and Lee, S. C.: Assessment of the quality of TROPOMI high-spatial-resolution NO_2 data products in the Greater Toronto Area, Atmos. Meas. Tech., 13, 2131-2159, https://doi.org/10.5194/amt-13-2131-2020, 2020.

Zheng, Y., Alapaty, K., Herwehe, J. A., Del Genio, A. D., and Niyogi, D.: Improving high-resolution weather forecasts using the Weather Research and Forecasting (WRF) Model with an updated Kain–Fritsch scheme, Monthly Weather Review, 144, 833-860, https://doi.org/10.1175/MWR-D-15-0005.1, 2016.

Table 1. Comparison of the concentrations of NO_y and its components between REAM and P-3B aircraft measurements during the DISCOVER-AQ campaign

			NO_y / ppb[1]	NO / ppb	NO_2_NCAR / ppb	NO_2_LIF / ppb[2]	∑PNs / ppb	∑ANs / ppb	HNO_3 / ppb	Derived-NO_y / ppb[3]
36-km[4]	Weekday[5]	P-3B	2.51 ± 2.09	0.18 ± 0.29	0.85 ± 1.13	0.68 ± 0.95	0.70 ± 0.58	0.31 ± 0.23	1.15 ± 0.73	2.86 ± 2.26
		REAM	3.64 ± 3.13	0.18 ± 0.30	0.74 ± 1.04	0.68 ± 0.89	0.54 ± 0.45	0.10 ± 0.09	1.80 ± 1.61	3.10 ± 2.70
		R^2	0.33	0.35	0.38	0.34	0.37	0.38	0.24	0.41
	Weekend	P-3B	3.00 ± 2.18	0.15 ± 0.20	0.71 ± 0.80	0.63 ± 0.72	0.91 ± 0.53	0.36 ± 0.21	1.15 ± 0.79	2.96 ± 2.15
		REAM	3.78 ± 2.20	0.15 ± 0.17	0.54 ± 0.59	0.53 ± 0.58	0.53 ± 0.29	0.09 ± 0.06	2.31 ± 1.38	3.43 ± 2.26
		R^2	0.29	0.28	0.41	0.45	0.27	0.39	0.50	0.51
4-km	Weekday	P-3B	2.51 ± 2.15	0.19 ± 0.30	0.86 ± 1.27	0.68 ± 0.98	0.70 ± 0.59	0.31 ± 0.22	1.17 ± 0.74	2.90 ± 2.27
		REAM	3.81 ± 3.81	0.19 ± 0.35	0.79 ± 1.31	0.76 ± 1.20	0.46 ± 0.51	0.08 ± 0.10	2.03 ± 1.91	3.31 ± 3.28
		R^2	0.28	0.22	0.26	0.32	0.37	0.29	0.38	0.47
	Weekend	P-3B	2.96 ± 2.13	0.14 ± 0.18	0.69 ± 0.74	0.63 ± 0.71	0.91 ± 0.51	0.35 ± 0.21	1.15 ± 0.80	2.94 ± 2.09
		REAM	4.36± 3.66	0.25 ± 0.40	0.85 ± 1.28	0.81 ± 1.23	0.41 ± 0.29	0.08 ± 0.08	2.54 ± 1.99	3.72 ± 3.52
		R^2	0.21	0.15	0.19	0.18	0.16	0.23	0.38	0.37

[1] For P-3B, the concentrations of NO_y, NO, and NO_2_NCAR were measured by using the NCAR 4-channel chemiluminescence instrument. The measurement uncertainties are 10%, 10 - 15%, and 10% for NO, NO_2, and NO_y, respectively. The 1-second, 1-sigma detection limits are 20 pptv, 30 pptv, and 20 pptv for NO, NO_2, and NO_y, respectively (https://discover-aq.larc.nasa.gov/pdf/2010STM/Weinheimer20101005_DISCOVERAQ_AJW.pdf). For REAM, NO_y is the sum of NO, NO_2, total peroxyacyl nitrates (∑PNs), total alkyl nitrates (∑ANs) (include alkyl nitrates and hydroxyalkyl nitrates), HNO_3, HONO, 2 × N_2O_5, HNO_4, first generation C5 carbonyl nitrate (nighttime isoprene nitrate ISN1: $C_5H_8NO_4$), 2 × C5 dihydroxydinitrate (DHDN: $C_5H_{10}O_8N_2$), methyl peroxy nitrate (MPN: $CH_3O_2NO_2$), propanone nitrate (PROPNN: $CH_3C(=O)CH_2ONO_2$), nitrate from methyl vinyl ketone (MVKN: $HOCH_2CH(ONO_2)C(=O)CH_3$), nitrate from methacrolein (MARCN: $HOCH_2C(ONO_2)(CH_3)CHO$), and ethanol nitrate (ETHLN: $CHOCH_2ONO_2$).

[2] For P-3B, the concentrations of NO_2_LIF, ∑PNs, ∑ANs, and HNO_3 were measured by applying the thermal dissociation-laser induced fluorescence (TD-LIF) technique. The accuracy of TD-LIF measurements of NO_2, ∑PNs, ∑ANs, and HNO_3 is better than 15%, and the detection limit for the sum of NO_2, ∑PNs, ∑ANs, and HNO_3 is ~ 10 ppt 10 s^{-1} (Day et al., 2002).

[3] To compare NO_y concentrations from TD-LIF measurements with those from REAM, we calculate derived-NO_y as the sum of NO, NO_2_LIF, ∑PNs, ∑ANs, and HNO_3. Only when the concentrations of all the five species are available at the same hour in the same grid cell, we can calculate derived-NO_y at the given hour in the given grid cell. Therefore, in Table 1, the averaged derived-NO_y values are not exactly equal to the sum of averaged NO, NO_2_LIF, ∑PNs, ∑ANs, and HNO_3 concentrations that only depend on the availability of a single species. In addition, the measurement times and frequencies between NO_y and derived-NO_y are not the same. A comparison between these two types of data needs coincident sampling, as described in the main text.

[4] Mean NO_x emissions over the six P-3B spiral sites are close (relative difference < 4%) between the 36-km and 4-km REAM (Table S1).

[5] Due to different sampling times and locations between weekdays and weekends, we do not recommend a direct comparison between weekday and weekend values here.

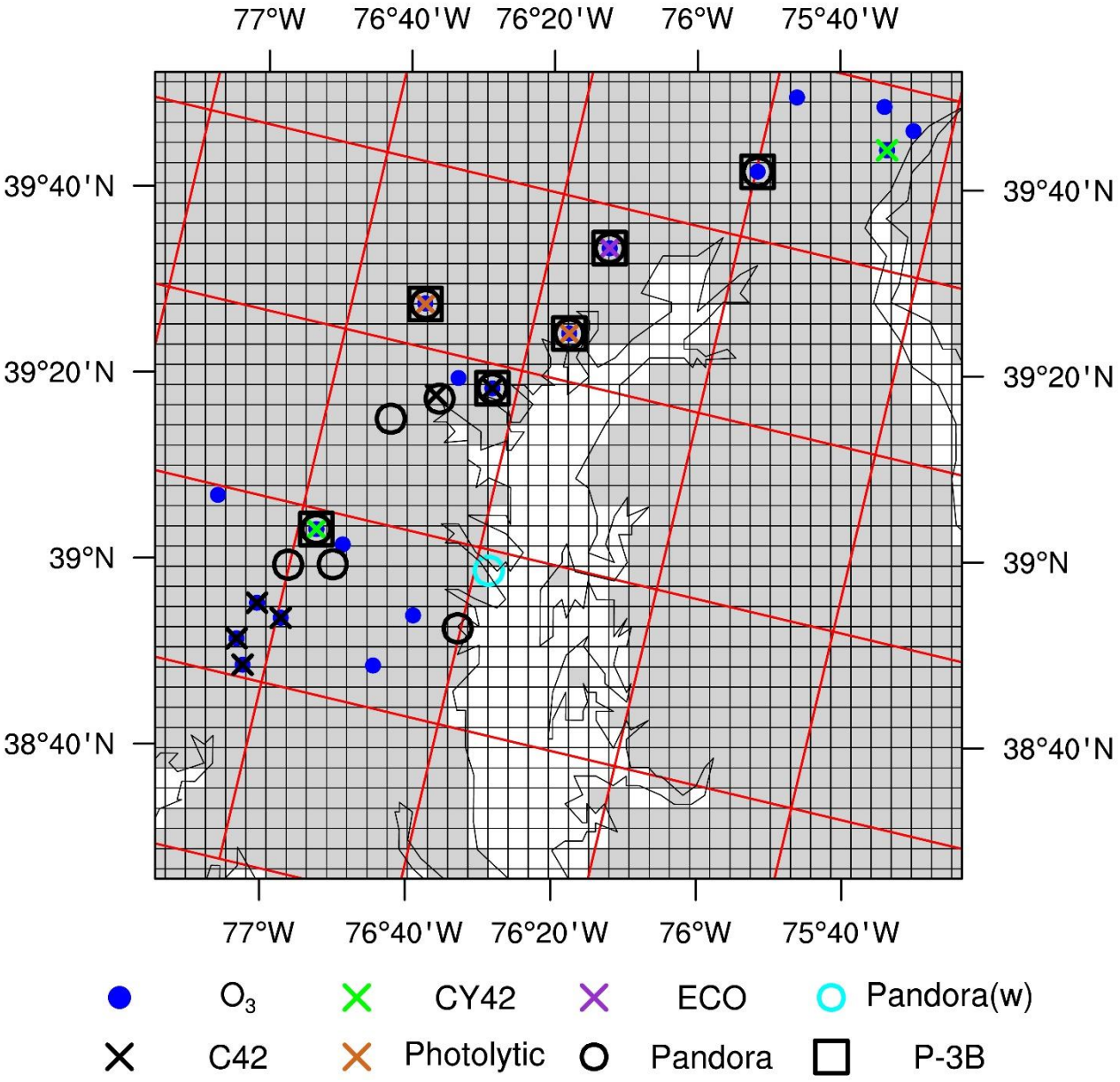

Figure 1. The locations of surface and P-3B aircraft observations during the DISCOVER-AQ 2011 campaign. We mark the 36-km REAM grid cells with red lines and the 4-km REAM grid cells with black lines. Gray shading denotes land surface in the nested 4-km WRF domain, while white area denotes ocean/water surface. Blue dots denote surface O_3 observation sites. Cross-marks denote surface NO_2 observation sites, and their colors denote different measurement instruments: green for the Thermo Electron 42C-Y NO_y analyzer, dark orchid for the Ecotech Model 9841/9843 T-NO_y analyzers, black for the Thermo Model 42C NO_x analyzer, and chocolate for the Teledyne API model 200eup photolytic NO_x analyzer. Circles denote Pandora sites, and the cyan circle denotes a Pandora site (USNA) on a ship. Black squares denote the inland P-3B aircraft spiral locations.

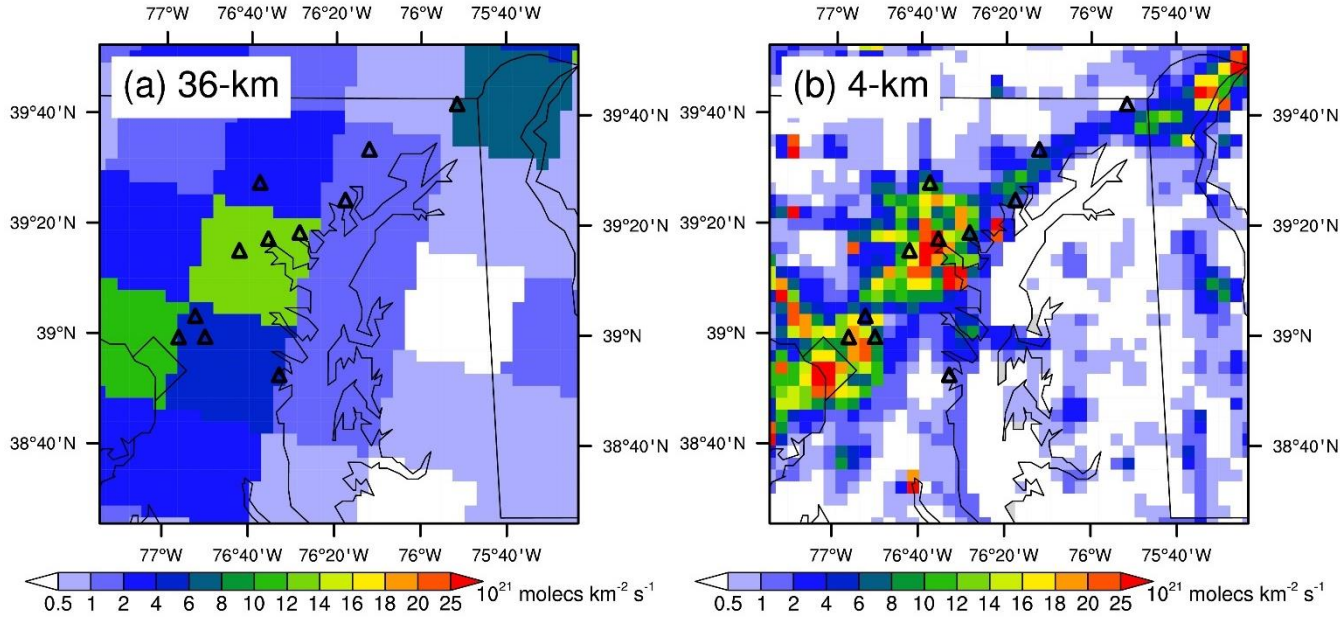

Figure 2. Distributions of NO_x emissions for the (a) 36-km and (b) 4-km REAM simulations around the DISCOVER-AQ 2011 region. Here NO_x emissions refer to the mean values (molecules km^{-2} s^{-1}) in one week (Monday – Sunday).

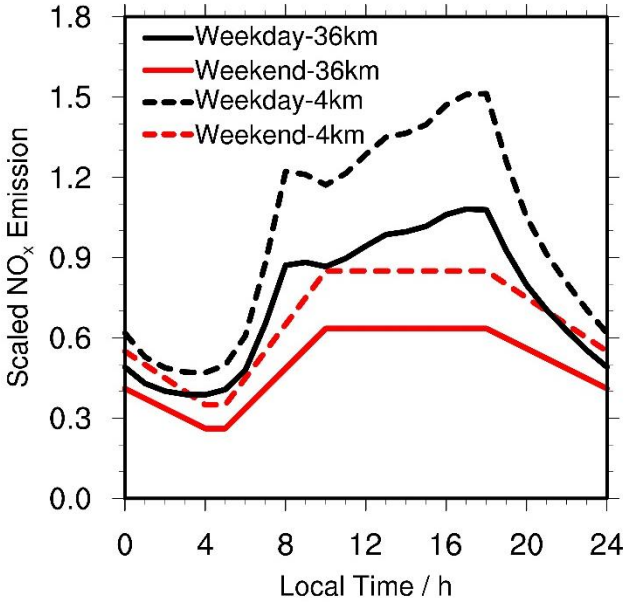

Figure 3. Relative diurnal profiles of weekday and weekend NO_x emissions (molecules km^{-2} s^{-1}) in the DISCOVER-AQ 2011 region (the 36/4 km grid cells over the 11 inland Pandora sites shown in Figure 1) for the 36-km and 4-km REAM. All the profiles are scaled by the 4-km weekday emission average value (molecules km^{-2} s^{-1}).

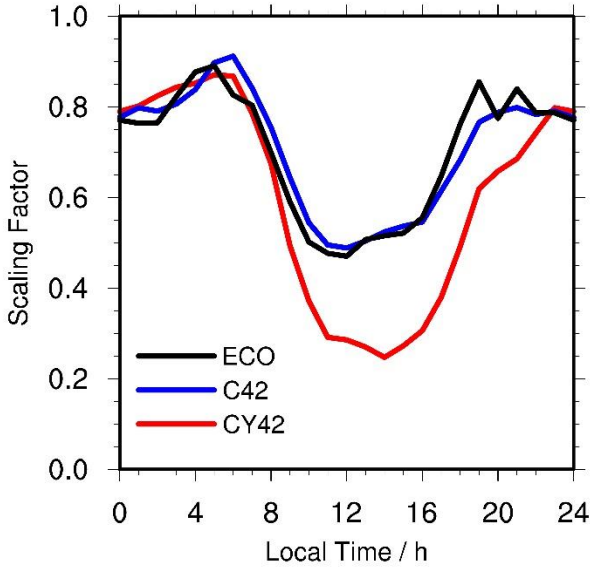

Figure 4. Hourly ratios of NO_2 measurements from the Teledyne API model 200 eup photolytic NO_x analyzer to NO_2 from coincident catalytic instruments for 2011 July. "CY42" denotes the ratios of photolytic NO_2 to NO_2 from the Thermo Electron 42C-Y NO_y analyzer in Edgewood, "C42" denotes the ratios of photolytic NO_2 to NO_2 from the Thermo Model 42C NO_x analyzer in Padonia, and "ECO" denotes the ratios of photolytic NO_2 to NO_2 from the Ecotech Model 9841 T-NO_y analyzer in Padonia. "ECO" ratios are also used to scale NO_2 measurements from the Ecotech Model 9843 T-NO_y analyzer.

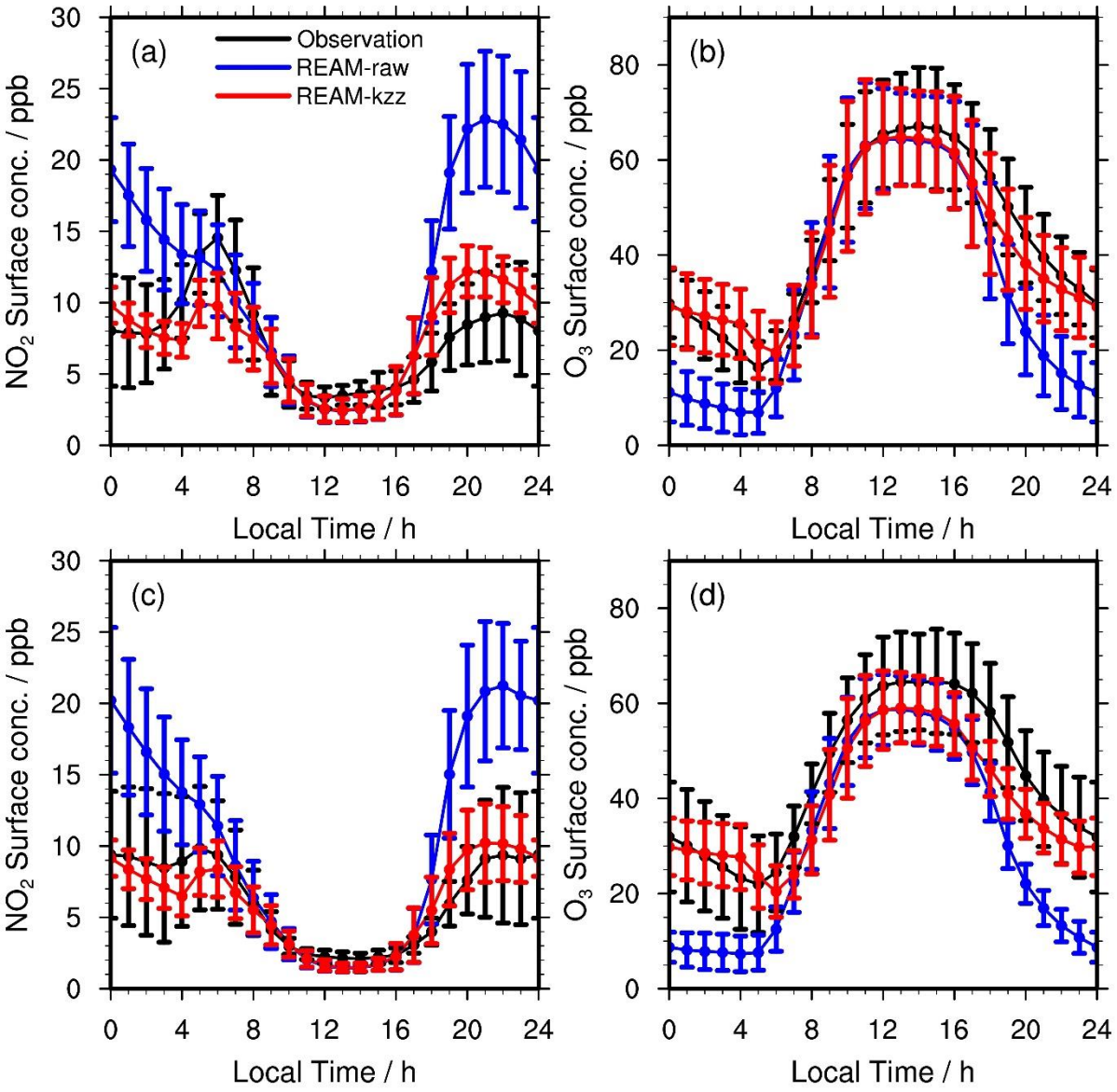

Figure 5. Diurnal cycles of surface (a, c) NO_2 and (b, d) O_3 concentrations on (a, b) weekdays and (c, d) weekends during the DISCOVER-AQ campaign in the DISCOVER-AQ region (the 36-km grid cells over the 11 inland Pandora sites shown in Figure 1). Black lines denote the mean observations from all the 11 NO_2 surface monitoring sites and 19 O_3 surface sites during the campaign (Figure 1), as mentioned in Section 2.5. "REAM-raw" (blue lines) denotes the coincident 36-km REAM simulation results with WRF-YSU simulated k_{zz} data, and "REAM-kzz" (red lines) is the coincident 36-km REAM simulation results with updated k_{zz} data. See the main text for details. Vertical bars denote corresponding standard deviations.

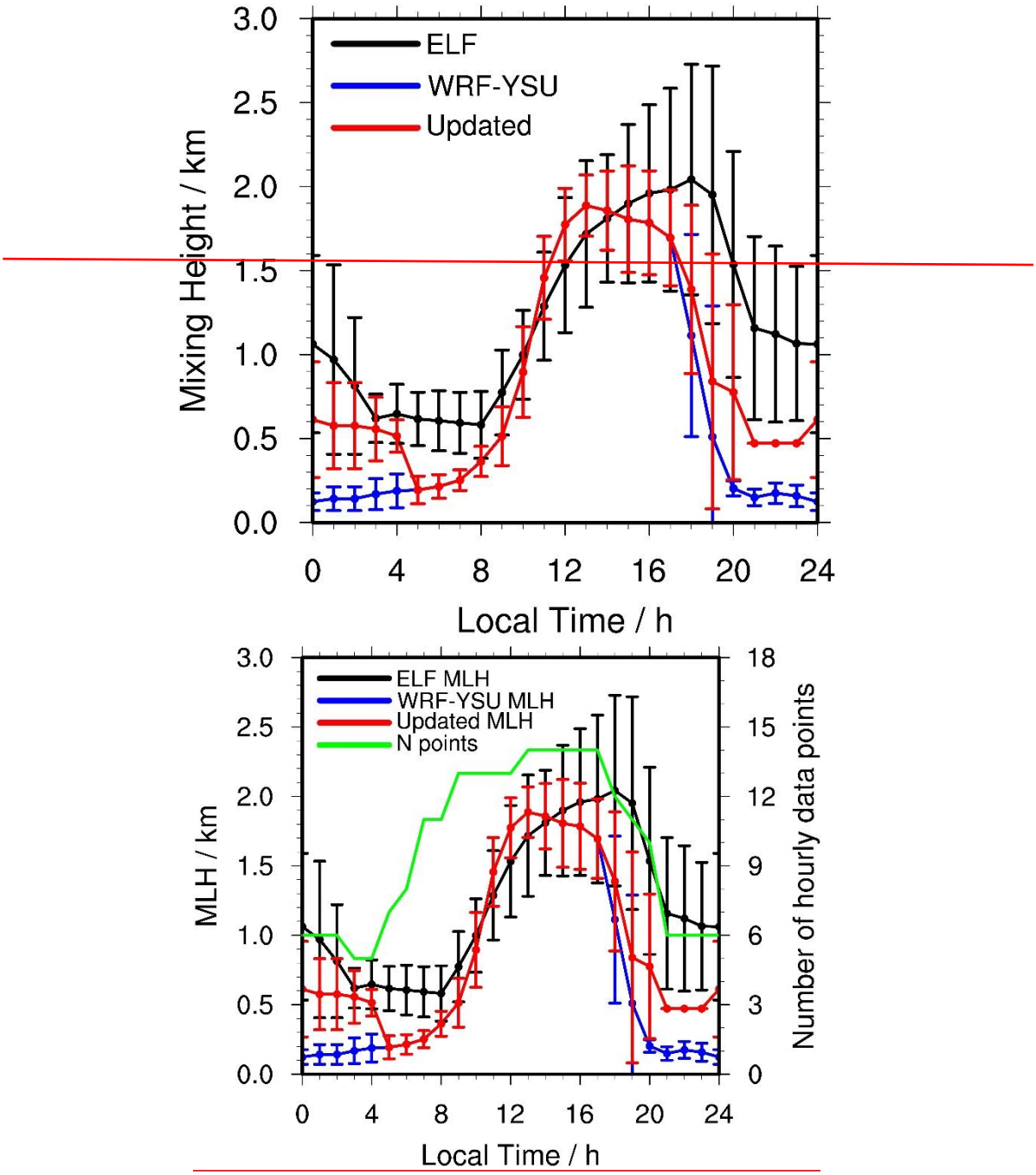

Figure 6. ELF observed and model simulated diurnal variations of MLH~~PBLH~~ at the UMBC site during the Discover-AQ campaign. "ELF MLH" denotes ELF derived ~~PBLHs~~ MLHs by using the covariance wavelet transform method. "WRF-YSU MLH" denotes the 36-km WRF-YSU k_{zz}-determined ~~PBLHs~~MLHs, and "Updated MLH" denotes updated k_{zz}-determined ~~PBLHs~~MLHs. See the main text for details. Vertical bars denote standard deviations. For the ELF MLHs, there are 13,506 1-

minute measurements in total during the campaign, and we bin them into hourly data. The green line corresponding to the right y-axis shows the diurnal variations of the number of hourly ELF data points.

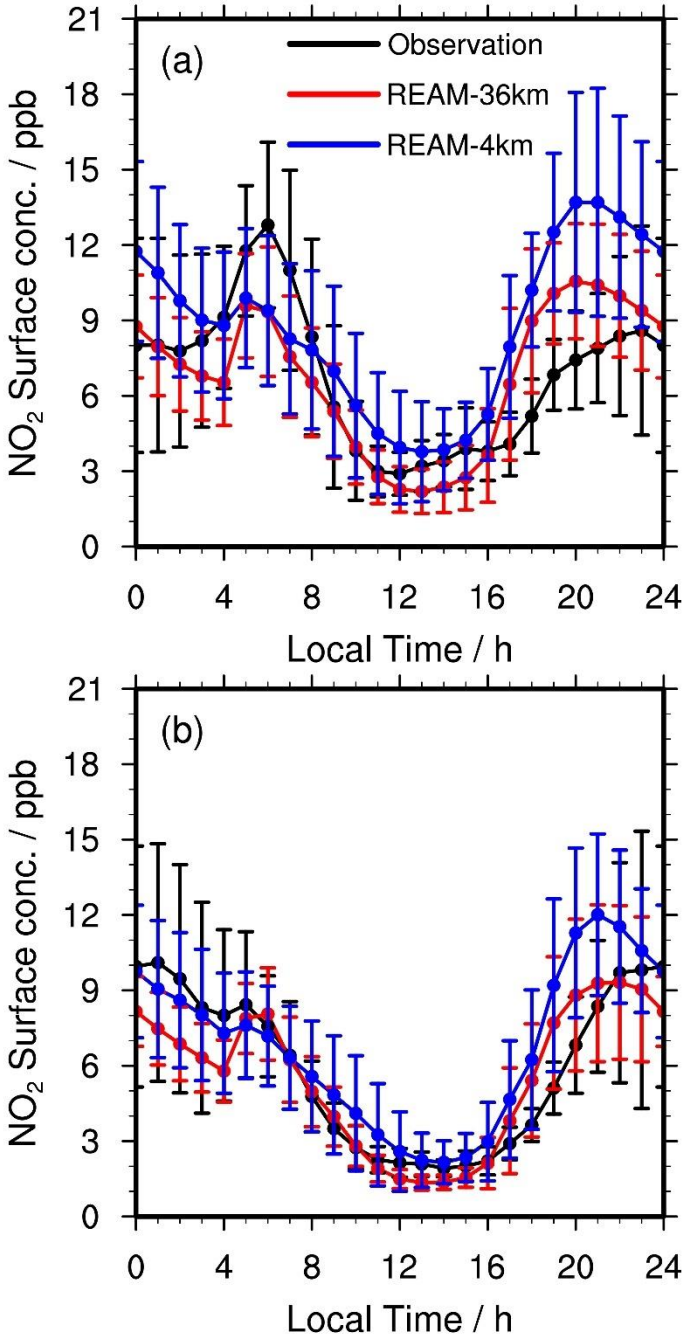

Figure 7. Diurnal cycles of observed and simulated average surface NO_2 concentrations over Padonia, Oldtown, Essex, Edgewood, Beltsville, and Aldino (Table S1) on (a) weekdays and (b) weekends. Black lines denote mean observations from the six sites. Red lines denote coincident 36-km REAM simulation results, and blue lines are for coincident 4-km REAM simulation results. Error bars denote standard deviations.

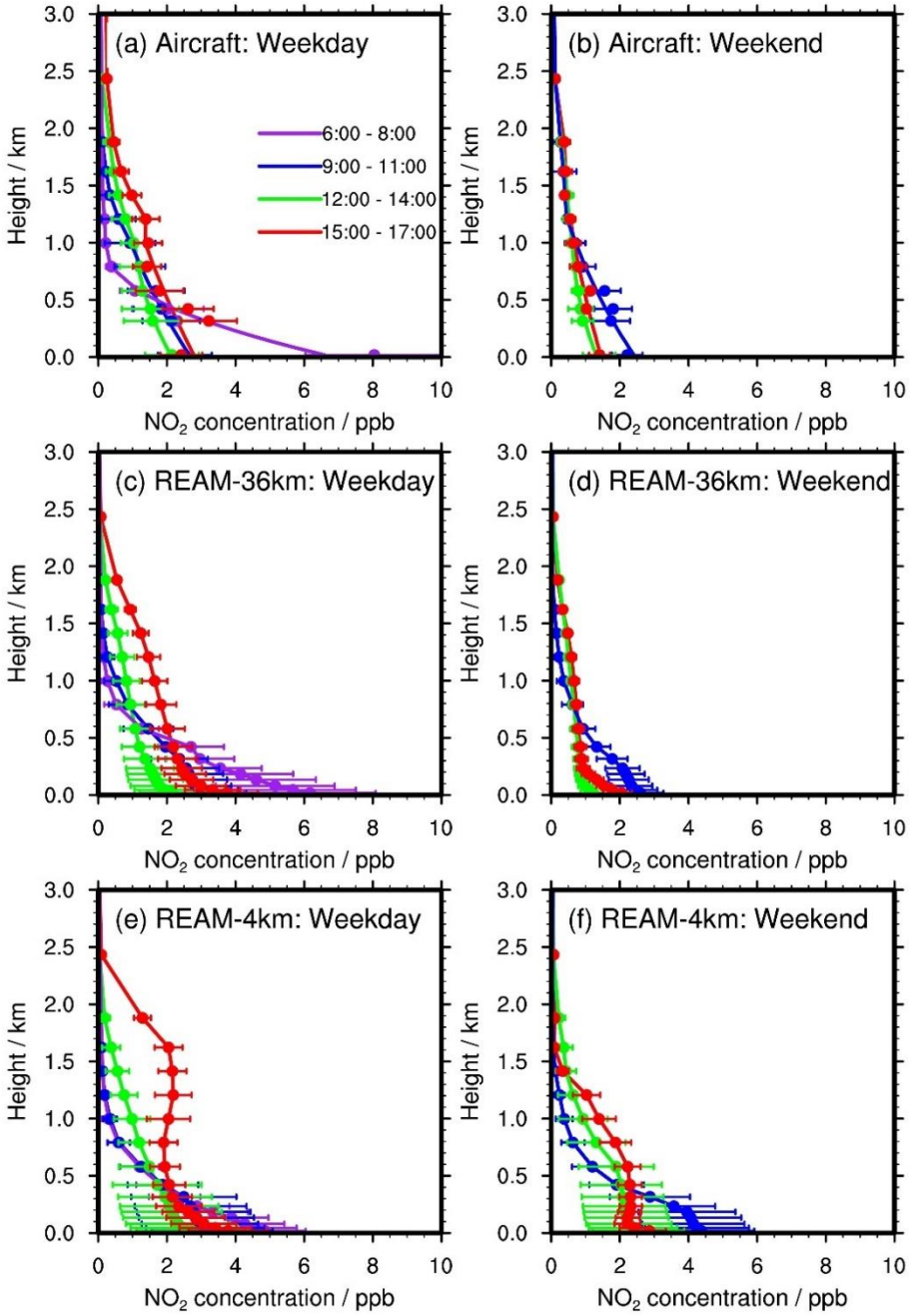

Figure 8. Temporal evolutions of NO_2 vertical profiles below 3 km on (a, c, e) weekdays and (b, d, f) weekends from the (a, b) P-3B aircraft and (c, d) 36-km and (e, f) 4-km REAM during the DISCOVER-AQ campaign. Horizontal bars denote the corresponding standard deviations. In (a) and (b), dots denote aircraft measurements, while lines below 1 km are based on quadratic polynomial fitting, as described in section 2.6. The fitting values are mostly in reasonable agreement with the aircraft and surface measurements in the boundary layer. On weekends, no aircraft observations were made at 6:00 – 8:00 LT, and therefore no corresponding model profiles are shown.

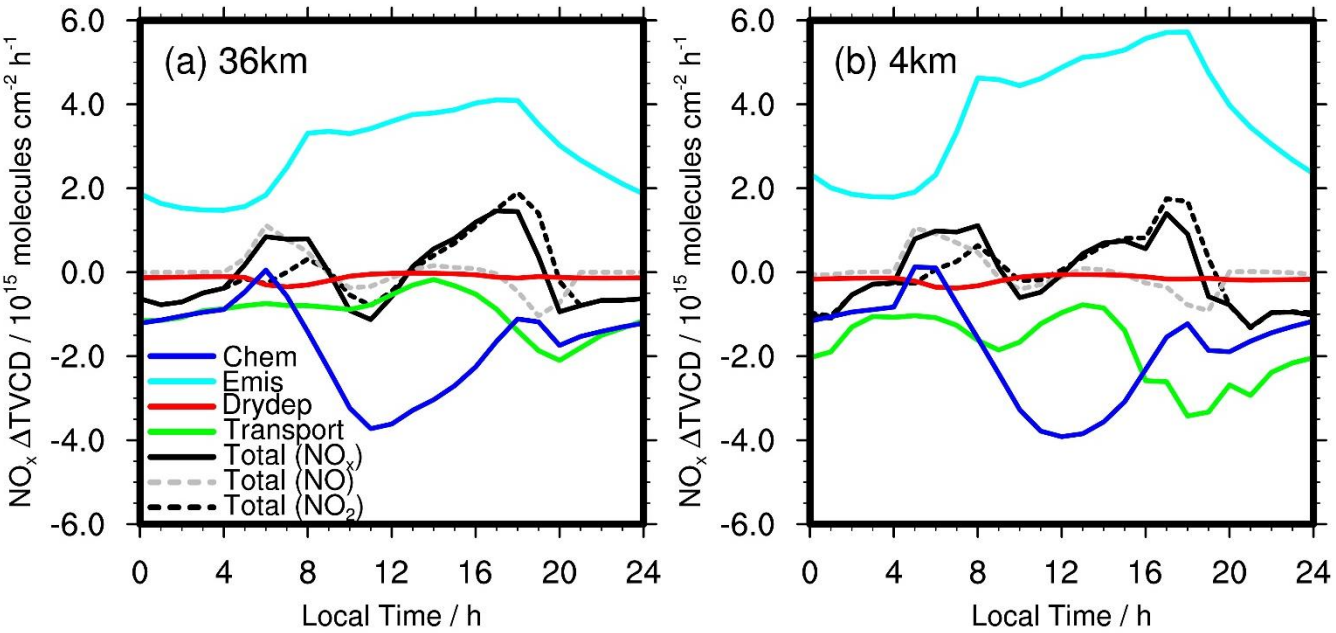

Figure 9. Contributions of emission, chemistry, transport, and dry deposition to NO_x TVCD diurnal variations over the 11 inland Pandora sites (Table S1 and Figure 1) on weekdays in July 2011 for the (a) 36-km and (b) 4-km REAM simulations. "Chem" refers to net NO_x chemistry production; "Emis" refers to NO_x emissions; "Drydep" denotes NO_x dry depositions; "Transport" includes advection, turbulent mixing, lightning NO_x production, and wet deposition. "Total (NO_x)" is the hourly change of NO_x TVCDs ($\triangle(TVCD) = TVCD_{t+1} - TVCD_t$). "Total ($NO_2$)" is the hourly change of NO_2 TVCDs, and "Total (NO)" is the hourly change of NO TVCDs.

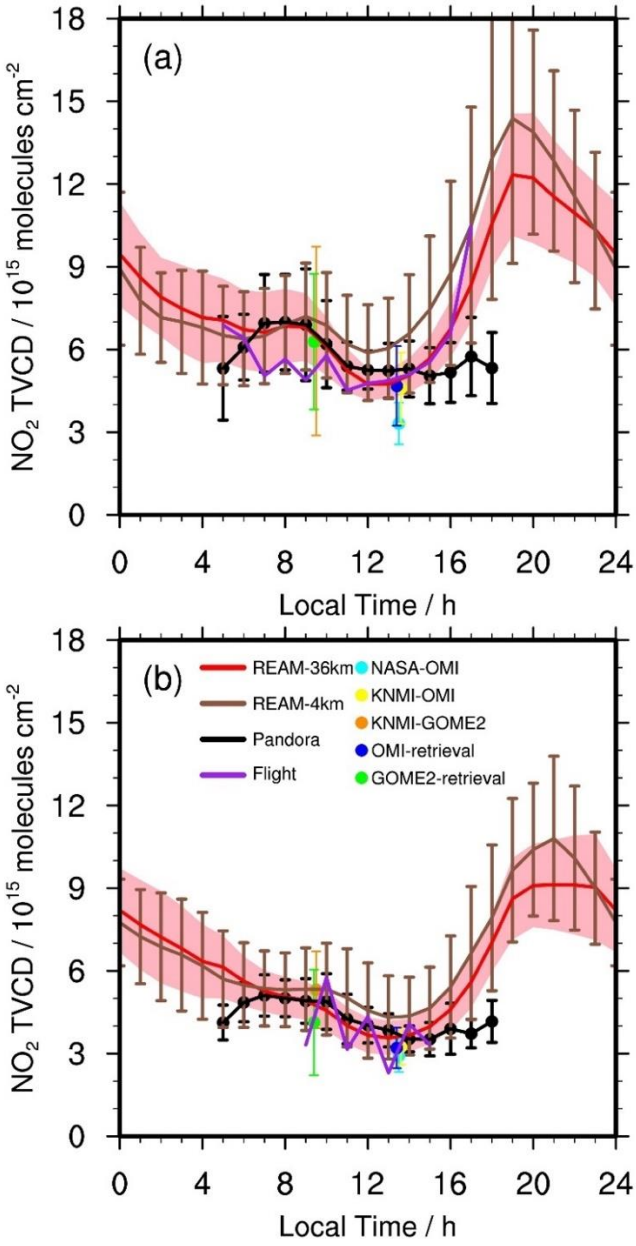

Figure 10. Daily variations of NO_2 TVCDs on (a) weekdays and (b) weekends during the DISCOVER-AQ campaign. "REAM-36km" refers to the 36-km REAM simulation results over the 11 inland Pandora sites. "REAM-4km" refers to the 4-km REAM simulation results over the 11 inland Pandora sites. "Pandora" refers to updated Pandora TVCD data. "Flight" denotes P-3B aircraft-derived NO_2 VCDs below 3.63 km. "NASA-OMI" denotes the OMI NO_2 TVCDs retrieved by NASA over the Pandora sites; "KNMI-OMI" denotes the OMI NO_2 TVCDs from KNMI; "KNMI-GOME2" is the GOME-2A NO_2 TVCDs from KNMI. "OMI-retrieval" and "GOME2-retrieval" denote OMI and GOME-2A TVCDs retrieved by using the KNMI DOMINO algorithm with corresponding 36-km REAM vertical profiles, respectively. The vertical bars denote corresponding standard deviations for all data except the 36-km REAM simulation results, the standard deviations of which are shown with pink shading. We list NO_2 TVCD values at 9:30 and 13:30 LT in Table S3.

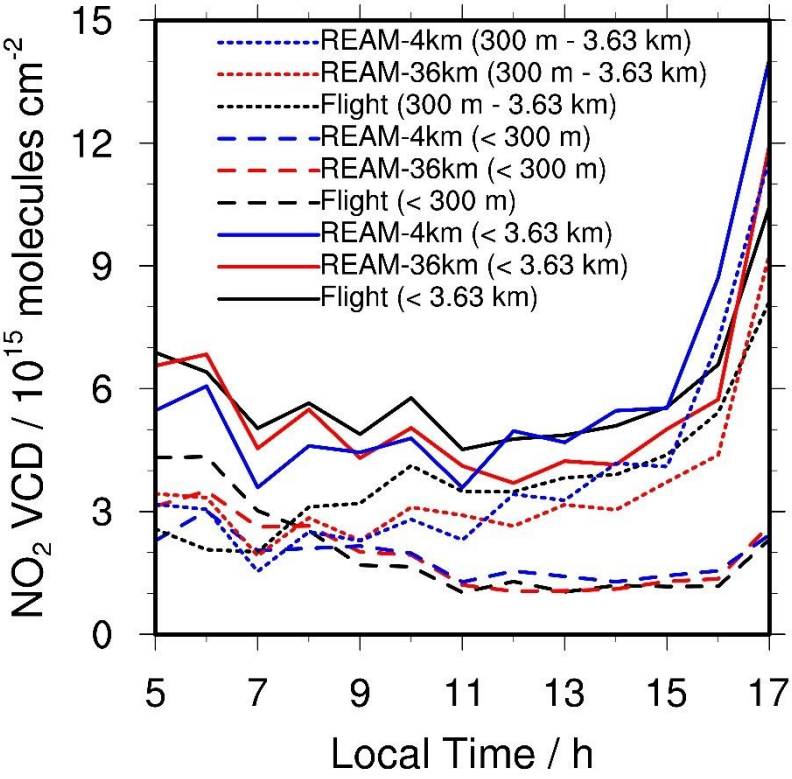

Figure 11. Weekday hourly variations of NO_2 VCDs at different height (AGL) bins (< 3.63 km AGL, < 300 m AGL, and 300 m ~ 3.63 km AGL) based on P-3B aircraft-derived datasets and the 36-km and 4-km REAM results. "Flight" denotes P-3B aircraft-derived NO_2 VCDs, "REAM-36km" denotes coincident 36-km REAM simulated VCDs, and "REAM-4km" denotes coincident 4-km REAM simulated VCDs.

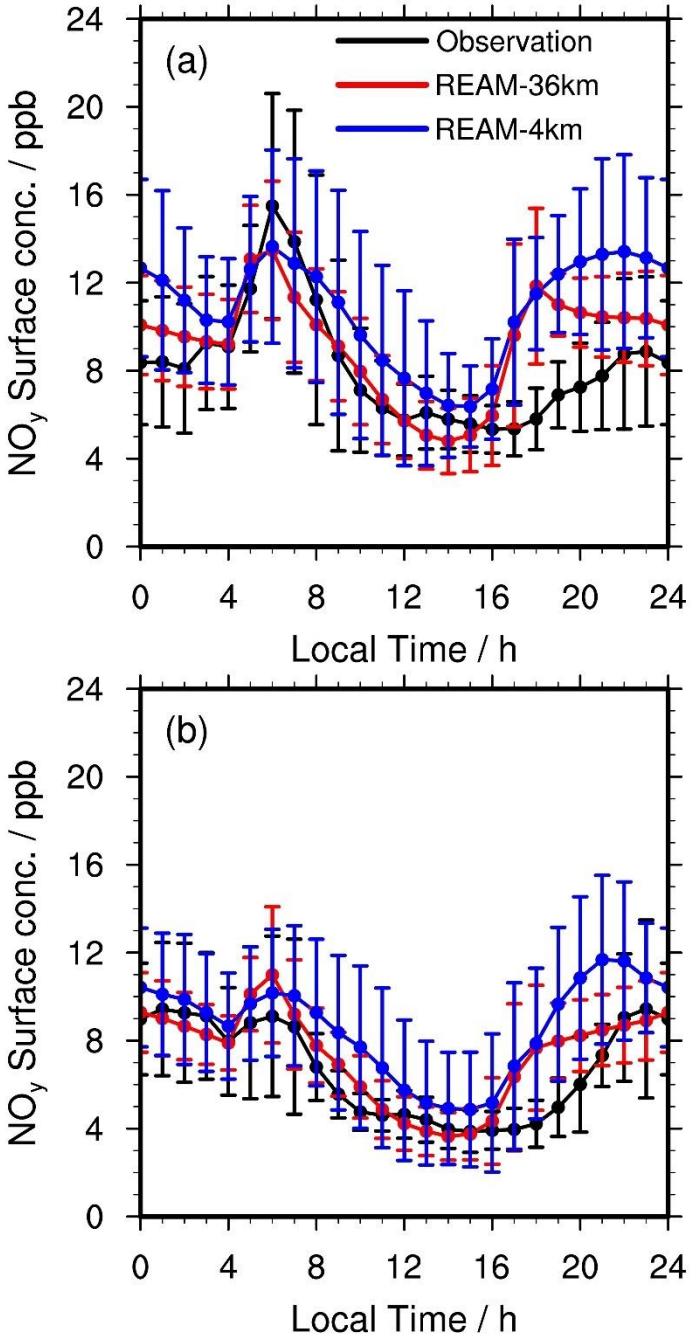

Figure 12. Diurnal cycles of observed and simulated average surface NO_y concentrations at Padonia, Edgewood, Beltsville, and Aldino on (a) weekdays and (b) weekends. Vertical bars denote the corresponding standard deviations. It is noteworthy that the mean NO_x emissions over Padonia, Edgewood, Beltsville, and Aldino are 99% higher in the 4-km than the 36-km REAM simulations (Table S1).

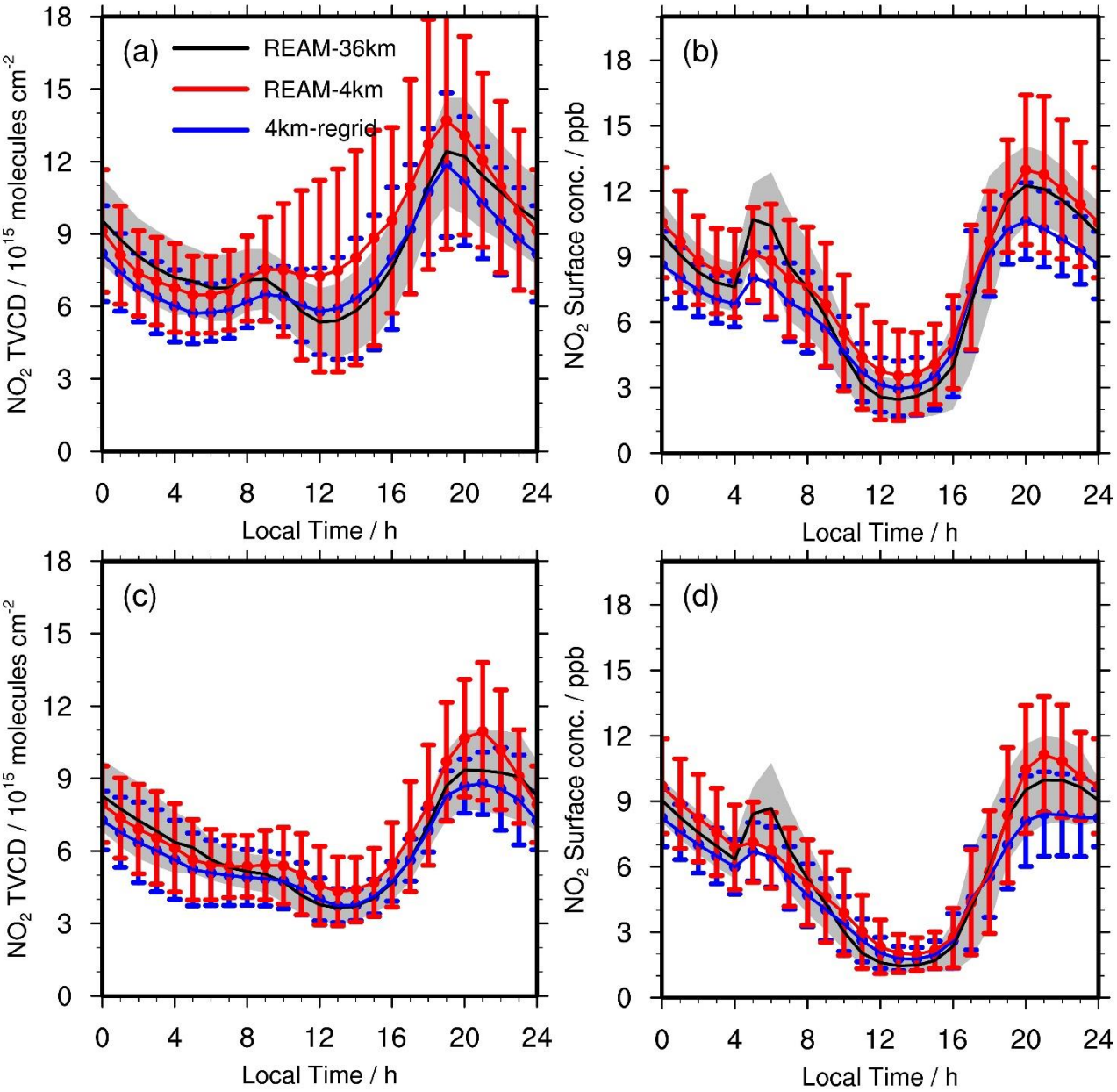

Figure 13. Comparisons of NO_2 (a, c) TVCDs and (b, d) surface concentrations over the 11 inland Pandora sites between the 4-km and 36-km REAM simulations on (a, b) weekdays and (c, d) weekends for July 2011. "REAM-36km" (black lines) denotes the 36-km REAM simulation results; "REAM-4km" (red lines) denotes the 4-km REAM simulation results; "4km-regrid" (blue lines) refers to the 36-km values by re-gridding the 4-km REAM simulation results into 36-km REAM grid cells. ~~Error bars denote standard deviations.~~The vertical bars denote corresponding standard deviations for all data except the 36-km REAM simulation results, the standard deviations of which are shown with gray shading.

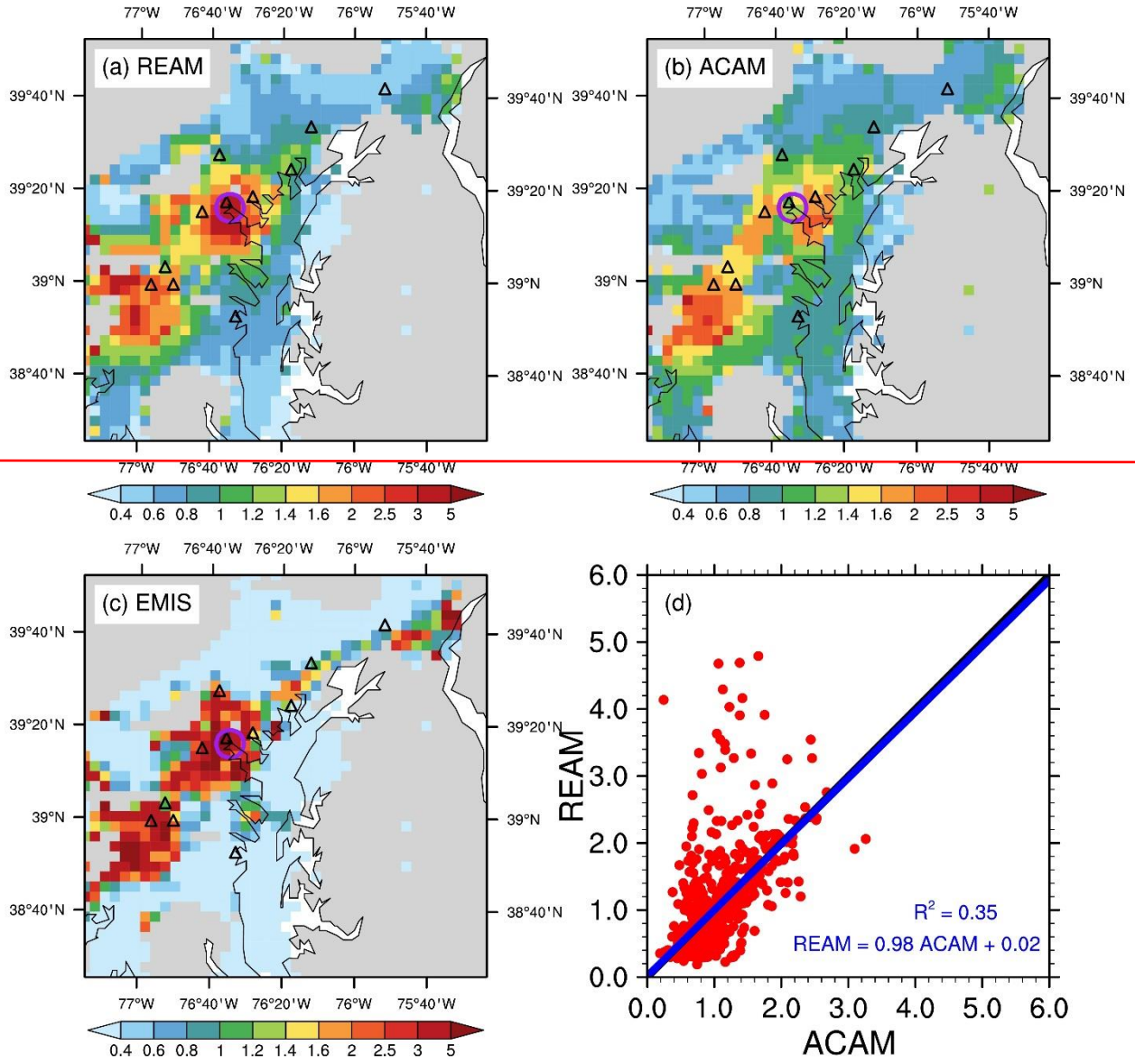
(a) REAM
(b) ACAM
(c) EMIS
(d)
77°W
76°40'W
76°20'W
76°W
75°40'W
39°40'N
39°20'N
39°N
38°40'N
0.4 0.6 0.8 1 1.2 1.4 1.6 2 2.5 3 5
REAM
ACAM
R² = 0.35
REAM = 0.98 ACAM + 0.02
0.0 1.0 2.0 3.0 4.0 5.0 6.0

1299

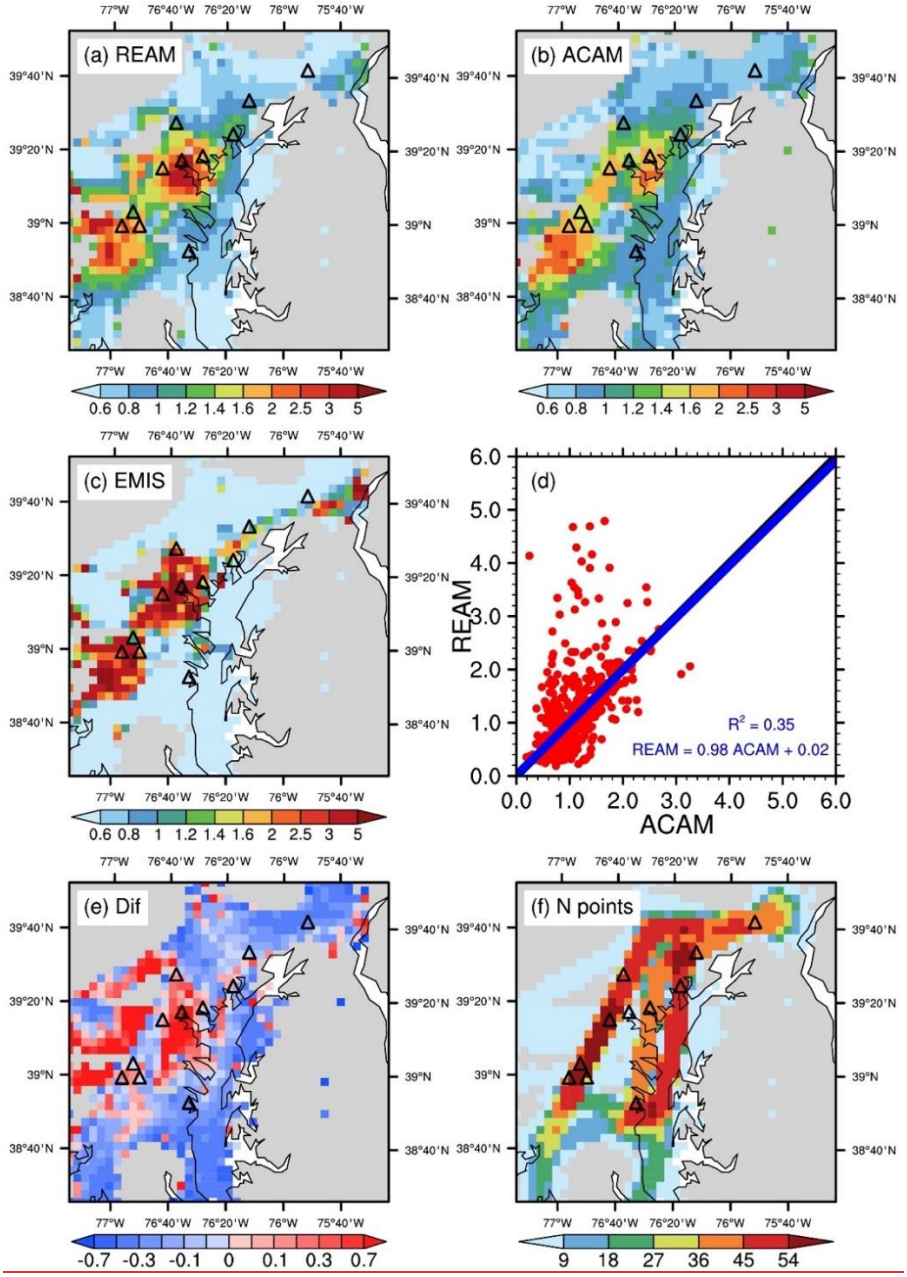

Figure 14. Distributions of the scaled mean (a) 4-km REAM simulated ~~ACAM~~ NO_2 VCDs below the UC-12 aircraft and (b) coincident ACAM ~~4-km REAM simulation result~~measurements on weekdays in July 2011. (c), the distribution of the scaled NEI2011 NO_x emissions on weekdays. ~~The purple circles denote a small region surrounded by high NO_x emission pixels and with high NO_2 VCDs in the 4-km REAM but low NO_2 VCDs in ACAM.~~ (d) ~~is t~~The scatter plot of the scaled 4-km REAM and ACAM ~~and 4-km REAM~~ NO_2 VCDs from (a) and (b). (e) shows the relative differences between (a) and (b) $(REAM/ACAM - 1)$. (f) The distribution of the number of data points used to calculate grid cell mean NO_2 VCDs in (a) and (b). Here, we scale all values (VCDs and NO_x emissions) based on their corresponding domain averages. The domain averages of ACAM and coincident 4-km REAM NO_2 VCDs are 4.7 ± 2.0 and 4.6 ± 3.2 × 10^{15} molecules cm^{-2}, respectively.

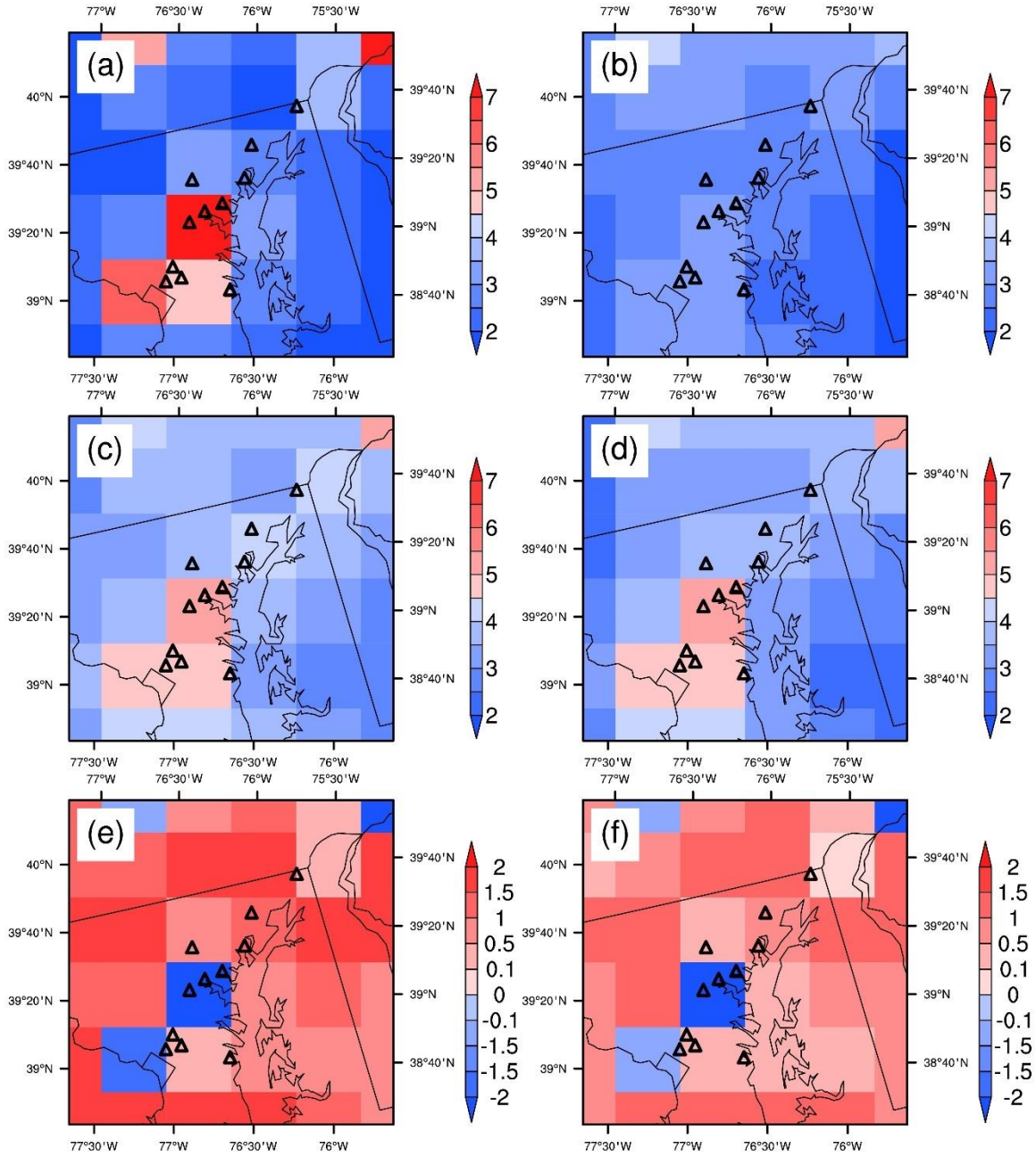

Figure 15. Distributions of weekday NO_2 TVCDs around the DISCOVER-AQ 2011 region for 13:30 LT in July 2011: (a) the 36-km REAM simulation results, (b) the NASA OMI product (OMNO2), (c) the KNMI OMI product, (d) the retrieved OMI NO_2 TVCDs by using the KNMI DOMINO algorithm with corresponding 36-km REAM vertical profiles, (e) the distribution of the NO_2 TVCD differences (c minus a) between KNMI OMI and 36-km REAM, and (f) the difference (d minus a) between retrieved OMI NO_2 TVCDs and the 36-km REAM results. The NO_2 TVCD unit is 10^{15} molecules cm^{-2}.

Supporting figures for

Comprehensive evaluations of diurnal NO_2 measurements during DISCOVER-AQ 2011: Effects of resolution dependent representation of NO_x emissions

Jianfeng Li[1, a], Yuhang Wang[1*], Ruixiong Zhang[1], Charles Smeltzer[1], Andrew Weinheimer[2], Jay Herman[3], K. Folkert Boersma[4, 5], Edward A. Celarier[6, 7, b], Russell W. Long[8], James J. Szykman[8], Ruben Delgado[3], Anne M. Thompson[6], Travis N. Knepp[9, 10], Lok N Lamsal[6], Scott J Janz[6], Matthew G Kowalewski[6], Xiong Liu[11], Caroline R. Nowlan[11]

[1]School of Earth and Atmospheric Sciences, Georgia Institute of Technology, Atlanta, Georgia, USA
[2]National Center for Atmospheric Research, Boulder, Colorado, USA
[3]University of Maryland Baltimore County JCET, Baltimore, Maryland, USA
[4]Royal Netherlands Meteorological Institute, De Bilt, the Netherlands
[5]Wageningen University, Meteorology and Air Quality Group, Wageningen, the Netherlands
[6]NASA Goddard Space Flight Center, Greenbelt, Maryland, USA
[7]Universities Space Research Association, Columbia, Maryland, USA
[8]National Exposure Research Laboratory, Office of Research and Development, U.S. Environmental Protection Agency, Research Triangle Park, NC, USA
[9]NASA Langley Research Center, Virginia, USA
[10]Science Systems and Applications, Inc., Hampton, Virginia, USA
[11]Harvard-Smithsonian Center for Astrophysics, Cambridge, Massachusetts, USA

[a]now at: Atmospheric Sciences and Global Change Division, Pacific Northwest National Laboratory, Richland, Washington, USA
[b]now at: Digital Spec, Tyson's Corner, VA, USA

[*] *Correspondence to* Yuhang Wang (yuhang.wang@eas.gatech.edu)

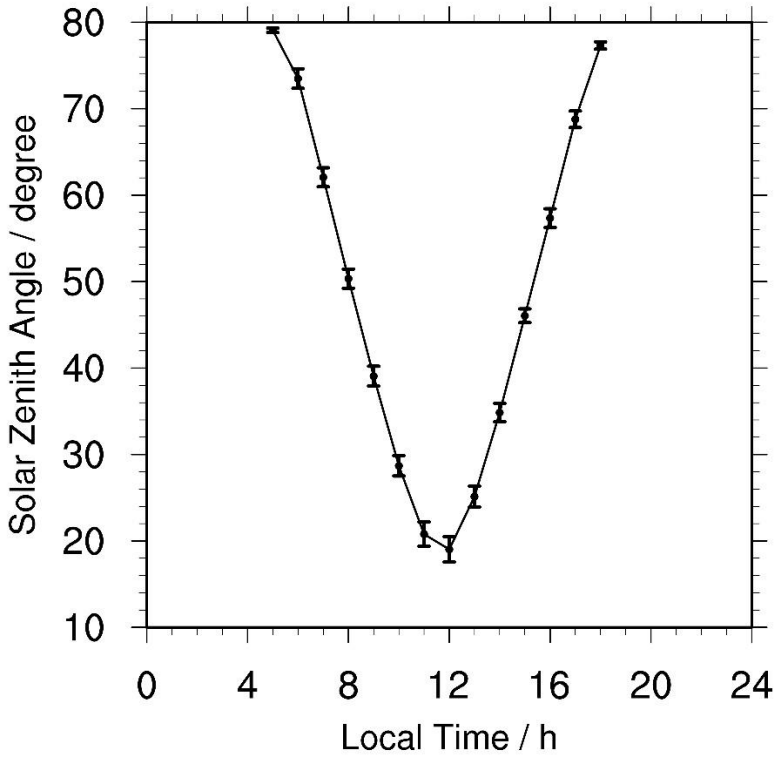

Figure S1. Diurnal variations of the solar zenith angles of Pandora measurements in July 2011. Here we use monthly averages of the 11 inland Pandora sites (Table S1 and Figure 1). Error bars denote standard deviations.

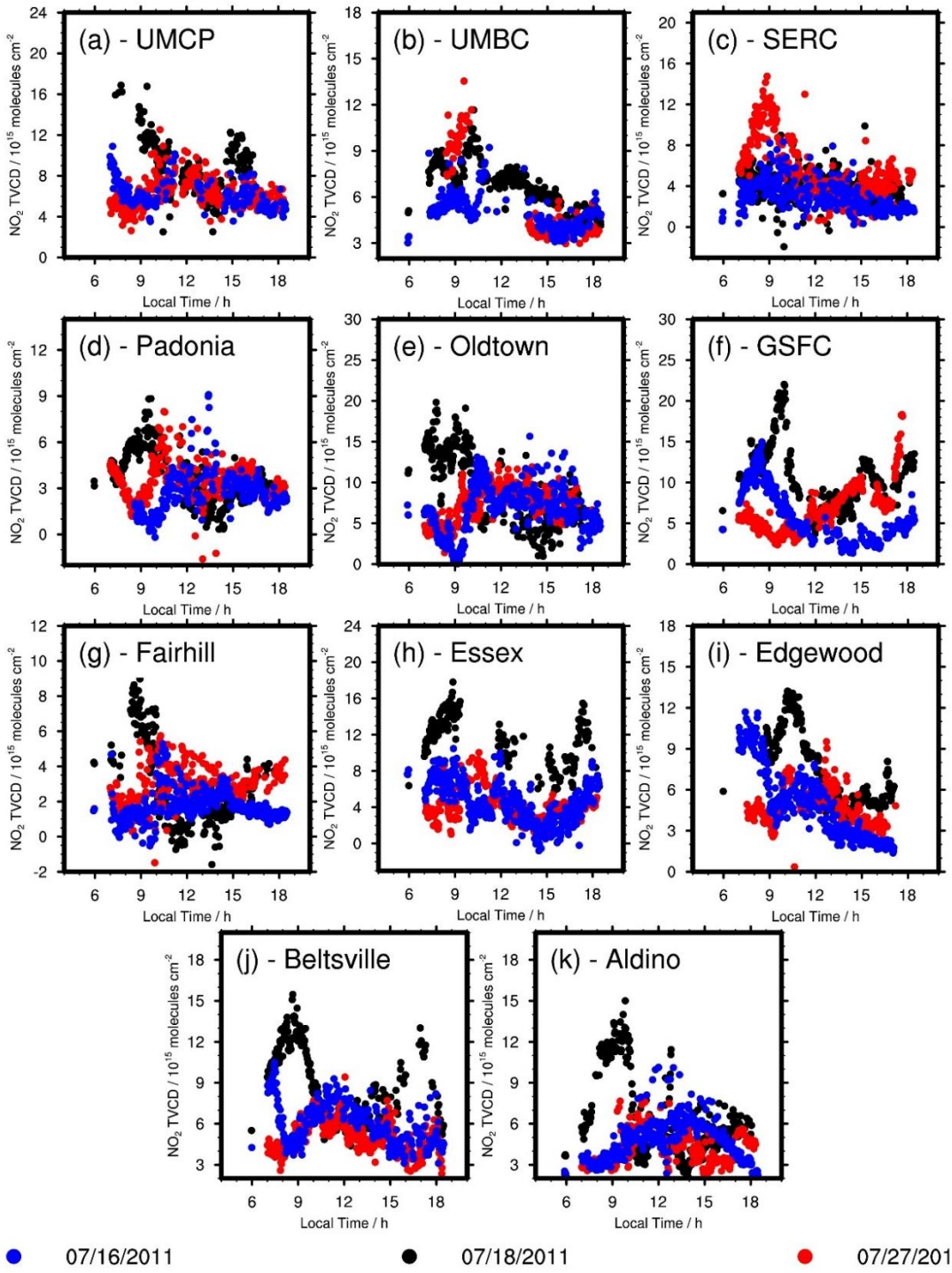

Figure S2. Daily variations of Pandora NO_2 TVCDs at the 11 inland sites for three randomly selected days in July 2011. Blue dots denote Pandora measurements on July 16, 2011 (Saturday), black dots denote July 18, 2011 (Monday), and red dots denote July 27, 2011 (Wednesday). Here Pandora NO_2 TVCDs are calculated by subtracting stratospheric NO_2 VCDs from Pandora total NO_2 VCDs. See the main text for details.

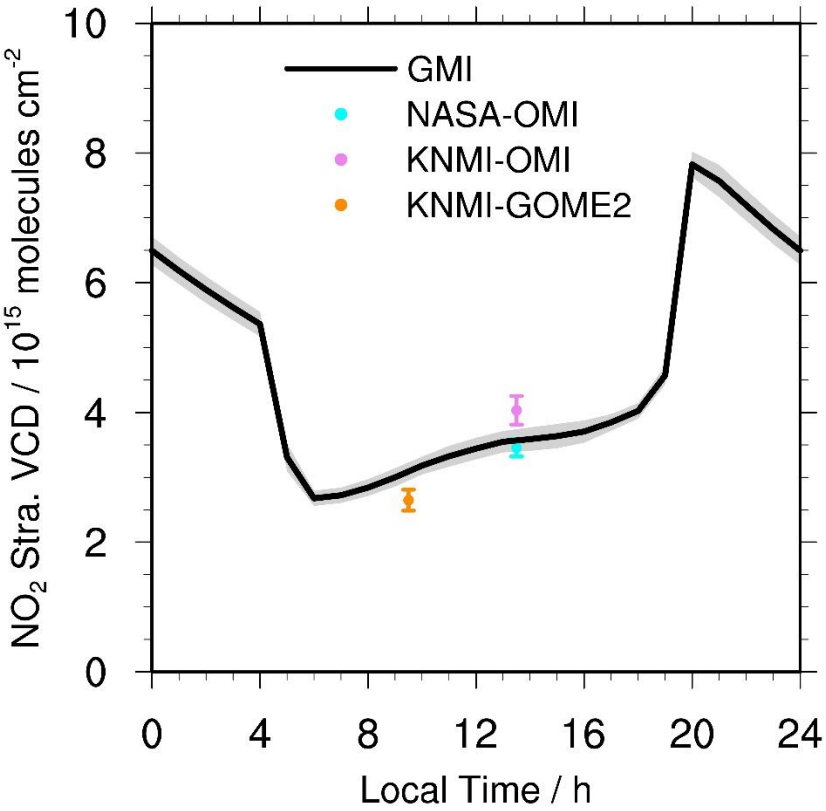

Figure S3. Stratospheric NO_2 VCD diurnal variations at the Greenbelt station in Maryland (39° N, 76.89° W) from the GMI MERRA-2 1° × 1.25° simulation (https://gmi.gsfc.nasa.gov/merra2hindcast/, last access: May 14, 2019) for July 2011, and the corresponding satellite stratospheric NO_2 VCDs in the DISCOVER-AQ region (about 39.2° N, 76.3° W) (Figure 1). "NASA-OMI" denotes the OMI NO_2 VCDs from NASA, "KNMI-OMI" denotes the OMI NO_2 VCDs from KNMI, and "KNMI-GOME2" denotes the GOME-2A NO_2 VCDs from KNMI. Gray shading and vertical bars denote the standard deviations of the GMI results and satellite stratospheric VCD products, respectively.

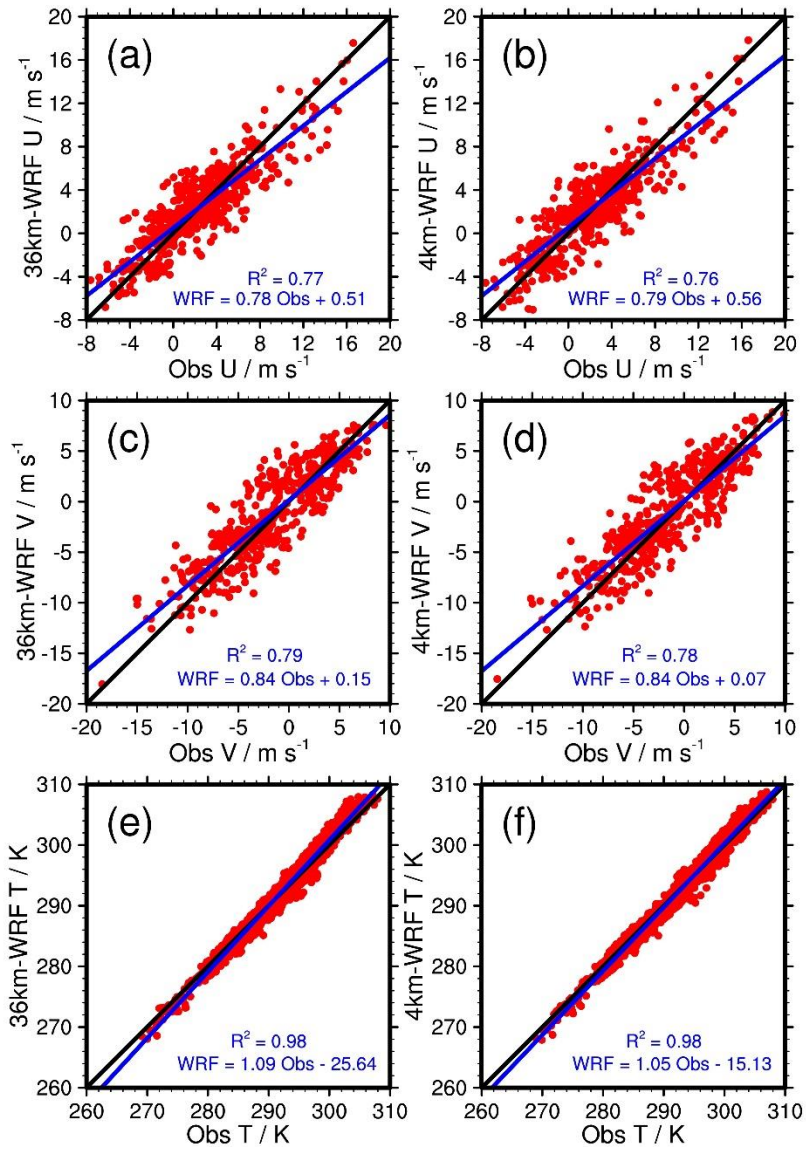

Figure S4. Comparisons of (a, b) U wind, (c, d) V wind, and (e, f) temperature (T) between P-3B spirals and coincident WRF simulation results for July 2011. For the P-3B observations, we derive U and V wind from the observed wind speed and wind direction (Figure S5), which were measured via a Honeywell INS sensor. The accuracies of P-3B wind speed and wind direction are 1 m s^{-1} and ± 5°, respectively. Air temperature on P-3B was measured by using a Rosemount model 102 sensor with an accuracy of ± 0.2 °C. The left panel is for comparisons between P-3B and the 36-km WRF simulation, and the right panel is for comparisons between P-3B and the nested 4-km WRF simulation. WRF wind components have been rotated to earth coordinates.

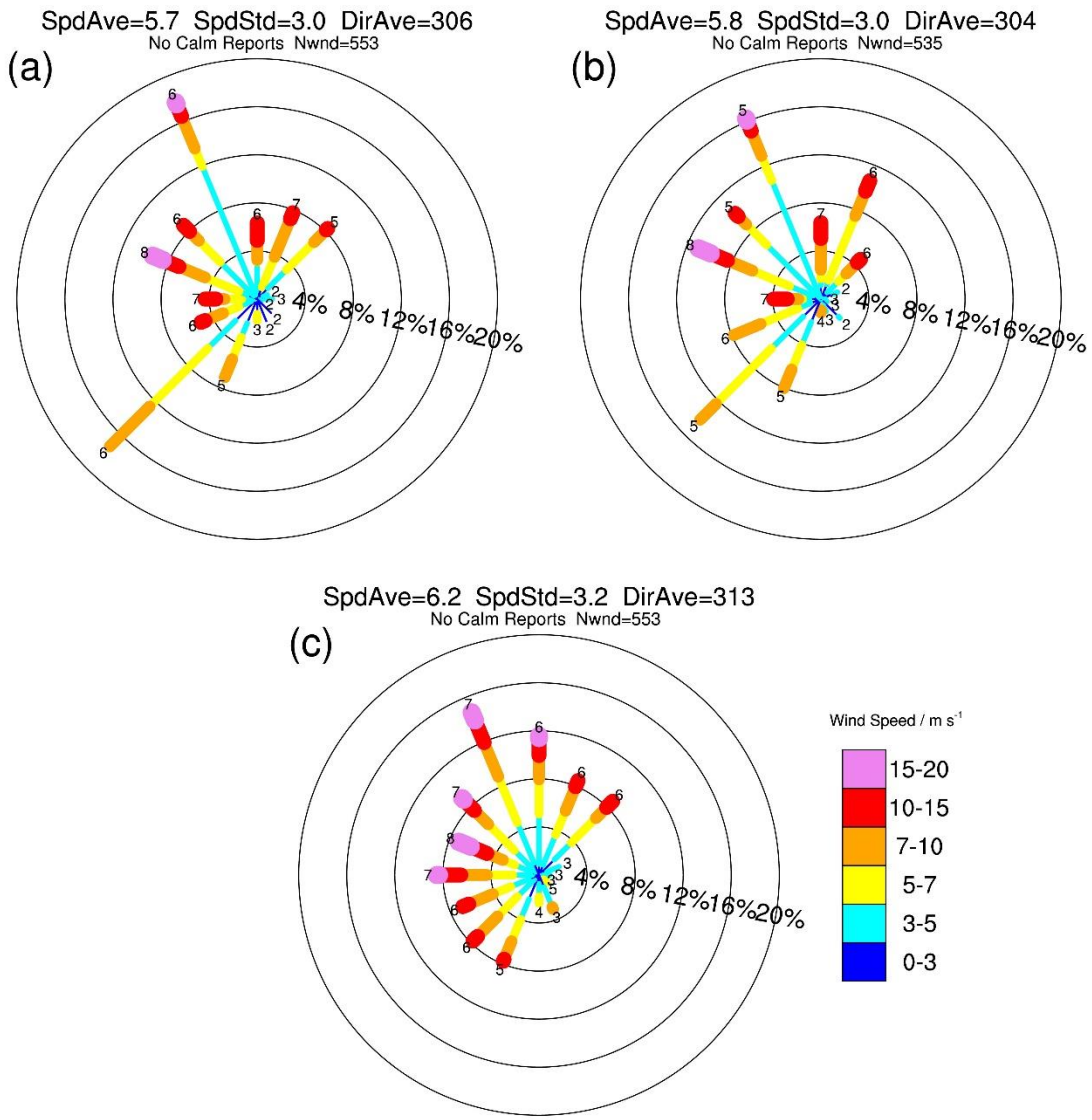

Figure S5. Wind roses for P-3B observations and coincident WRF simulation results for July 2011, (a) for the 36-km WRF simulation, (b) for the nested 4-km WRF simulation, and (c) for P-3B observations. WRF wind components have been rotated to earth coordinates. "SpdAve" denotes the average of wind speed, "SpdStd" denotes the standard deviation of wind speed, and "DirAve" denotes wind direction derived from averaged U-wind and V-wind.

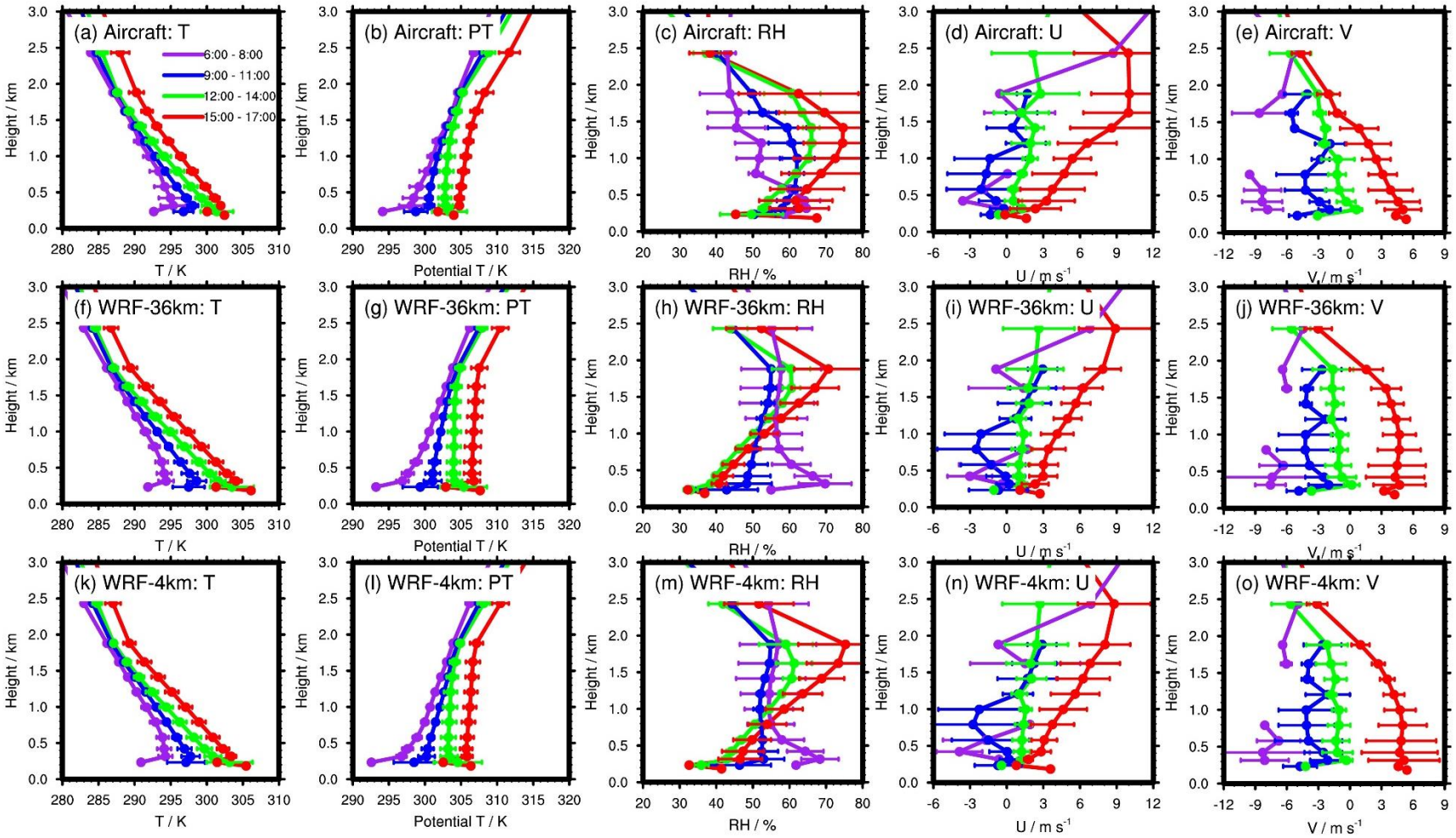

Figure S6. Temporal evolutions of vertical profiles for (a, f, k) temperature (T), (b, g, l) potential temperature (PT), (c, h, m) relative humidity (RH), (d, i, n) U-wind, and (e, j, o) V-wind below 3 km from the (a, b, c, d, e) P-3B aircraft and (f, g, h, i, j) 36-km and (k, l, ,m, n, o) nested 4-km WRF simulations during the DISCOVER-AQ campaign. Horizontal bars denote corresponding standard deviations. Purple lines denote 6:00 – 8:00 LT, blue lines for 9:00 – 11:00 LT, green lines for 12:00 – 14:00 LT, and red lines for 15:00 – 17:00 LT.

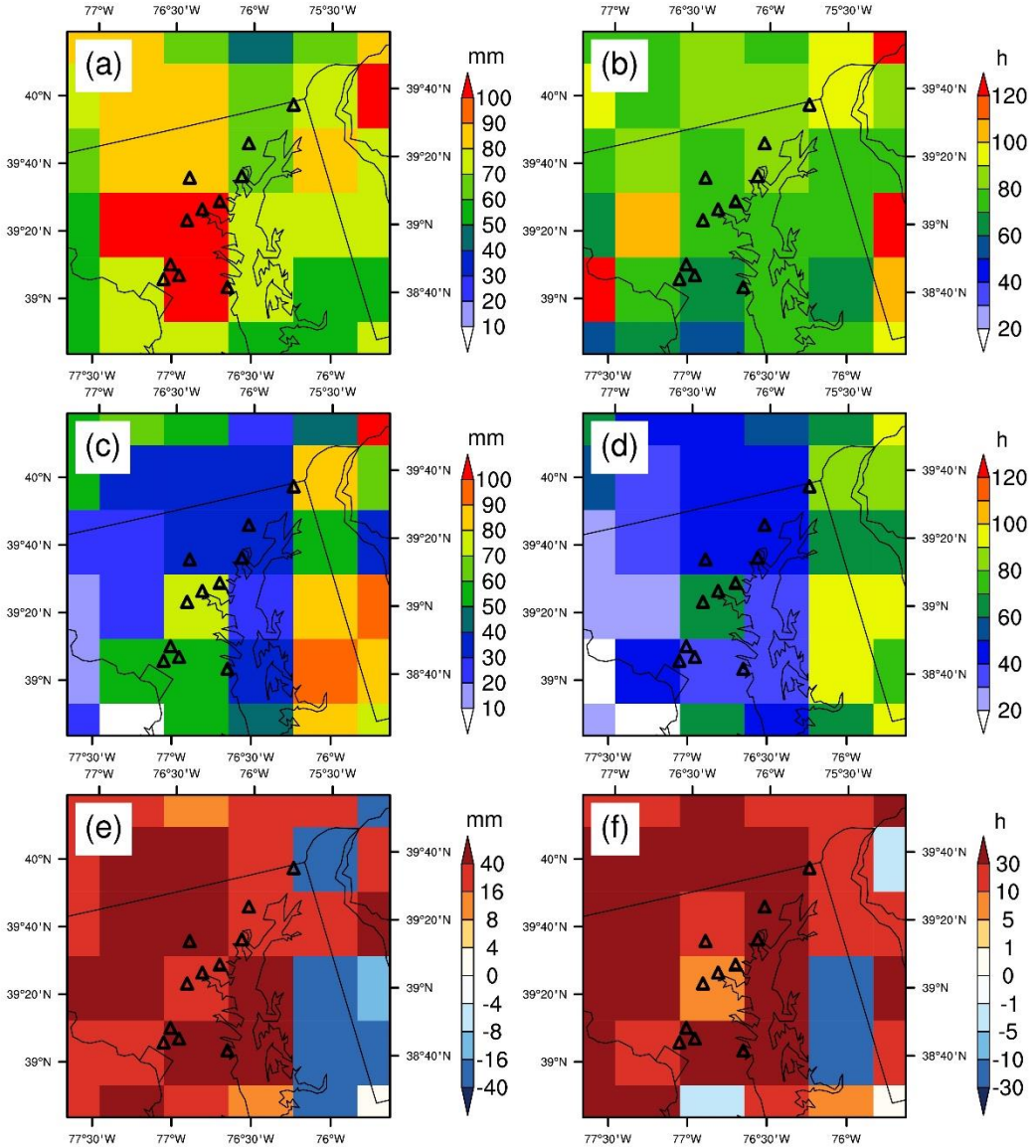

Figure S7. Distributions of (a, c) precipitation amounts and (b, d) precipitation durations in July 2011 for (a, b) Stage IV and (c, d) the 36-km WRF simulation. (e) and (f) are the differences in precipitation amount and precipitation duration between Stage IV and the 36-km WRF simulation. The original resolution of Stage IV is about 4 km over polar stereographic grids, and we regrid the dataset to the 36-km WRF pixels. Triangles denote the inland Pandora sites in Figure 1.

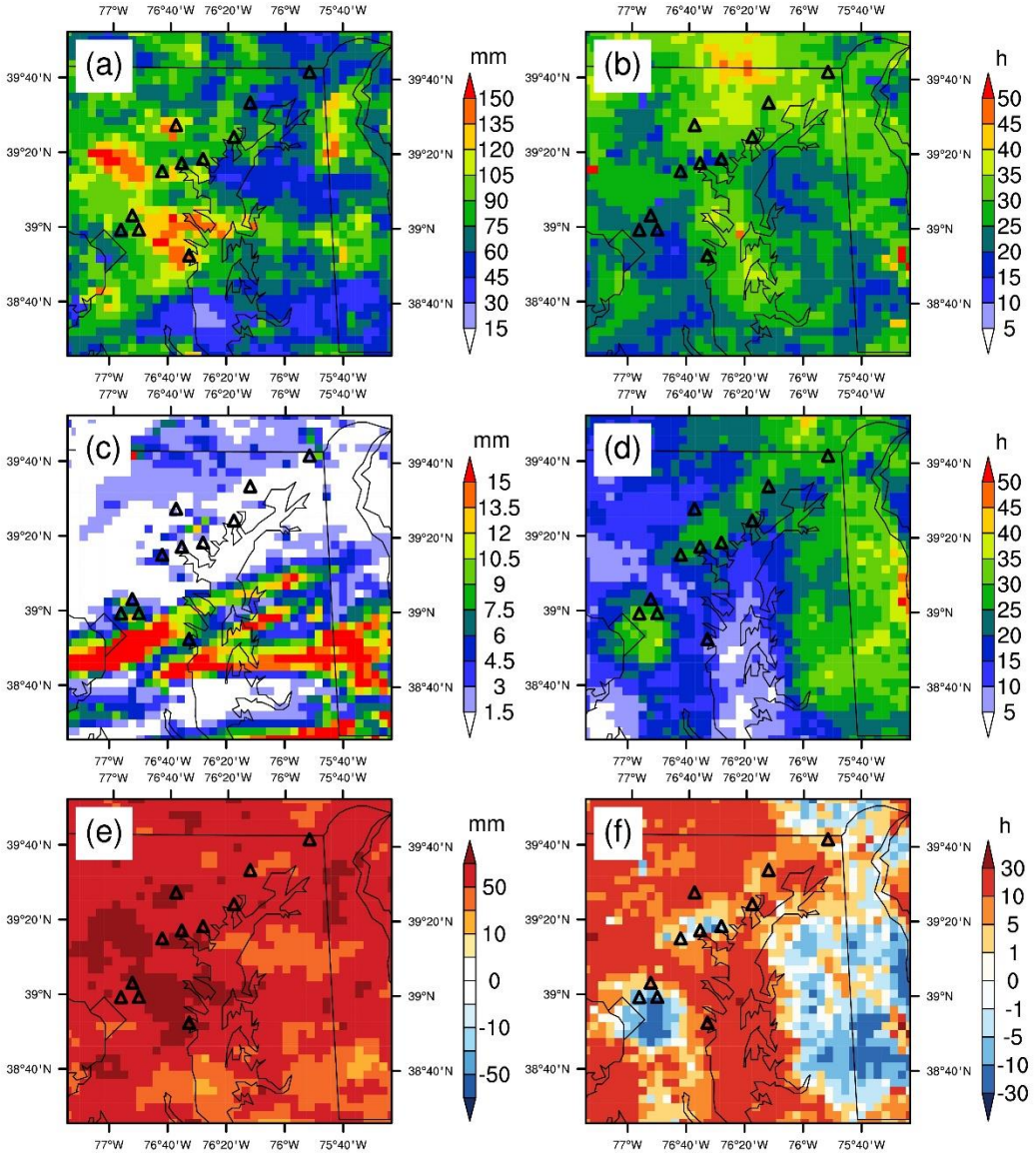

Figure S8. Distributions of (a, c) precipitation amounts and (b, d) precipitation durations in July 2011 for (a, b) Stage IV and (c, d) the nested 4-km WRF simulation. (e) and (f) stand for the differences in precipitation amount and precipitation duration between Stage IV and the nested 4-km WRF simulation. The original resolution of Stage IV is about 4 km over polar stereographic grids, and we regrid the dataset to the nested 4-km WRF pixels. Due to significantly lower precipitation amounts in the nested 4-km WRF simulation, we use different color bars for WRF and Stage IV data. Triangles denote the inland Pandora sites in Figure 1.

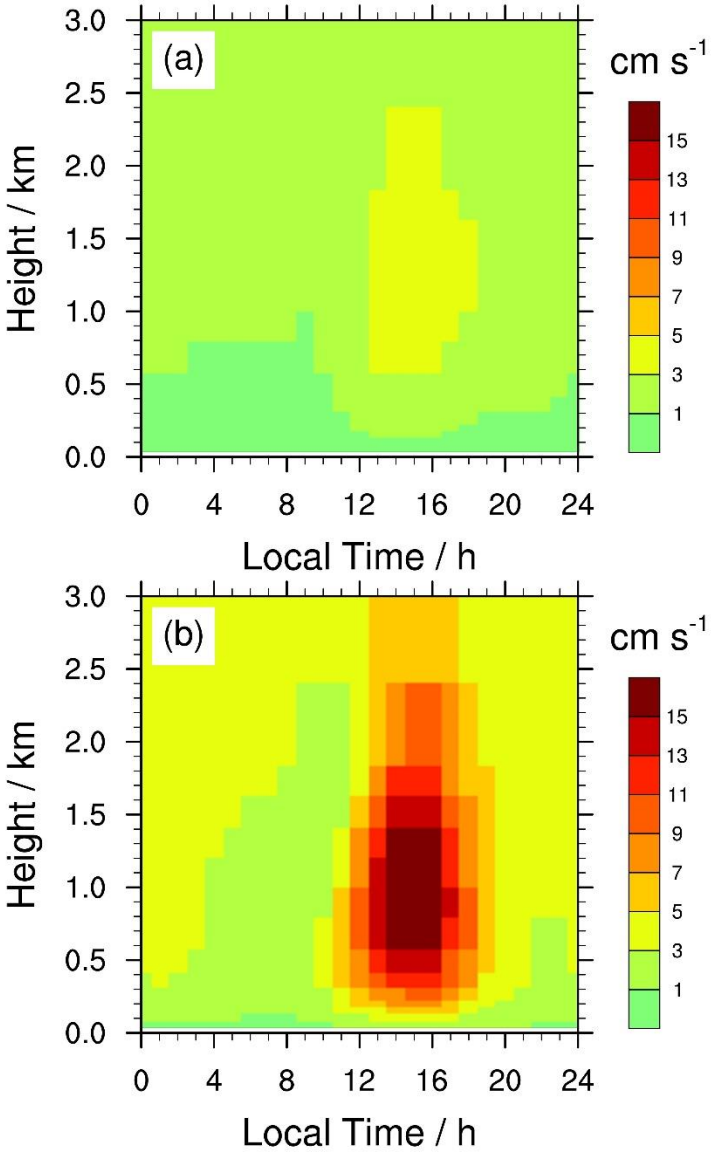

Figure S9. Diurnal variations of boundary-layer vertical velocities for the (a) 36-km and (b) nested 4-km WRF simulations in the DISCOVER-AQ region (Figure 1) for July 2011.

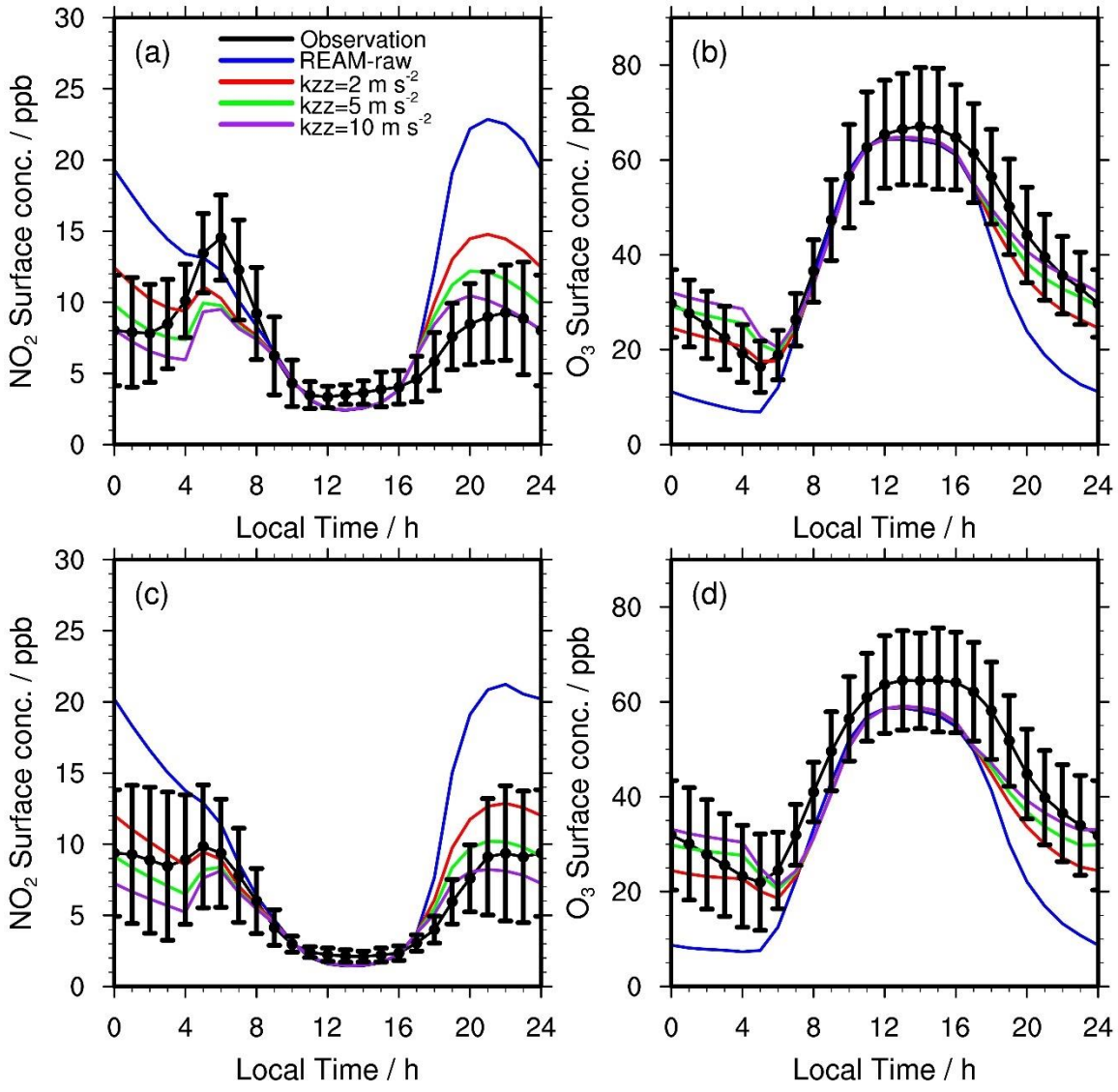

Figure S10. Similar as Figure 5 but with two additional REAM sensitivity tests with k_{zz} updated to 2 m s^{-2} or 10 m s^{-2} instead of 5 m s^{-2} following the approach mentioned in the main text.

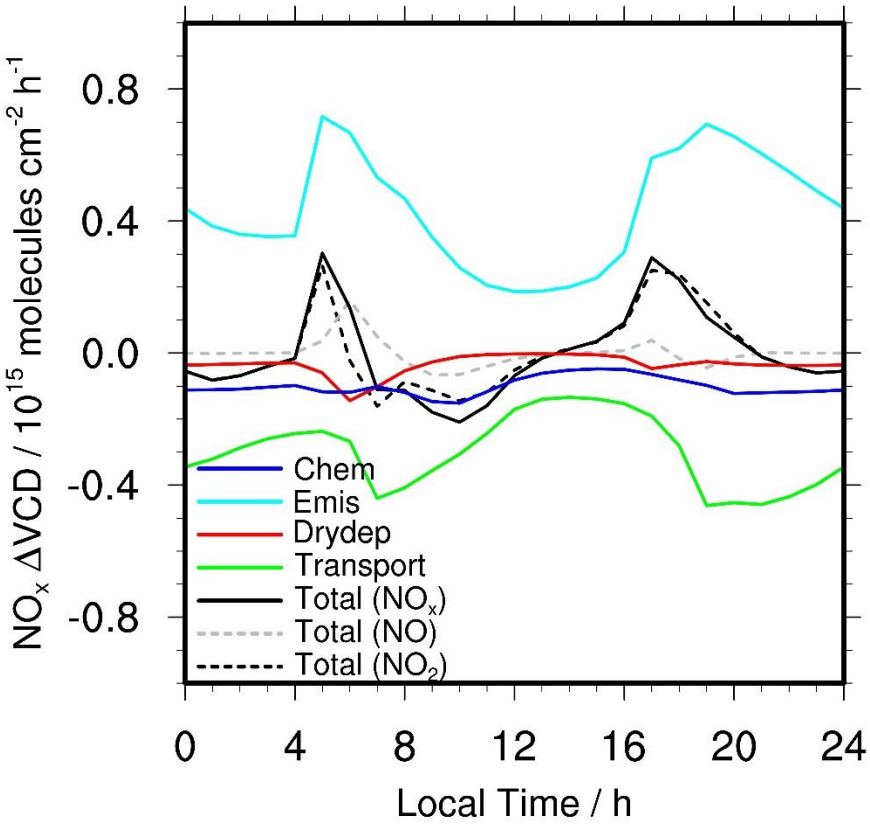

Figure S11. Contributions of emission, chemistry, transport, and dry deposition to NO_x VCD diurnal variations in the surface layer of the 36-km REAM simulation in the DISCOVER-AQ region on weekdays in July 2011. "Chem" refers to net NO_x chemistry production in the surface layer; "Emis" refers to NO_x emissions in the surface layer with the impact of vertical turbulent mixing; "Drydep" denotes NO_x dry depositions in the surface layer; "Transport" includes advection, turbulent mixing, lightning NO_x production, and wet deposition in the surface layer. "Total (NO_x)" is the hourly change of surface-layer NO_x VCDs ($\triangle(VCD) = VCD_{t+1} - VCD_t$). "Total ($NO_2$)" is the hourly change of surface-layer NO_2 VCDs, and "Total (NO)" is the hourly change of surface-layer NO VCDs.

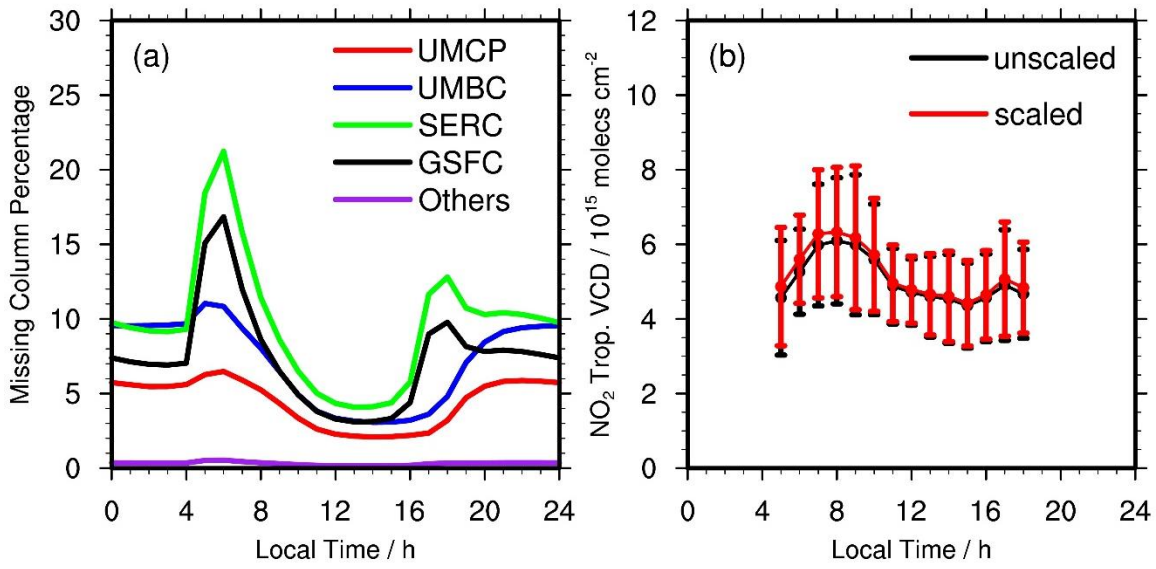

Figure S12. (a) Percentages of NO_2 VCDs below the heights of Pandora instruments in July 2011 based on 36-km REAM results; (b) the comparison between original Pandora TVCDs ("unscaled") and updated Pandora TVCDs ("scaled") with the inclusion of VCDs below the Pandora instruments. Here we use monthly averages in July 2011. Error bars in (b) denote standard deviations.

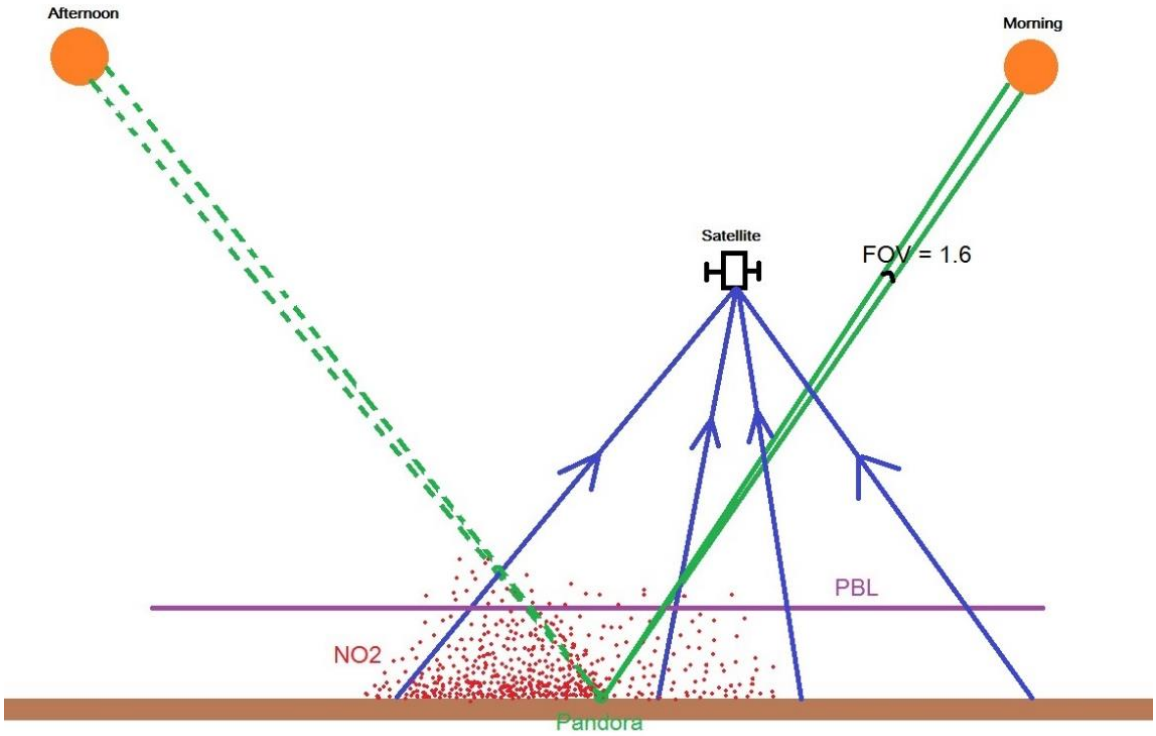

Figure S13. Schematic of remote and ground-based sensing of NO_2 VCDs. Green lines indicate the Pandora measurement rays, solid lines for the morning, and dash lines for the afternoon. Red dots denote NO_2 molecules. Blue lines represent the reflected radiation rays received by ~~the~~ satellite. Orange circles denote the sun, and the purple line denotes the PBL height.

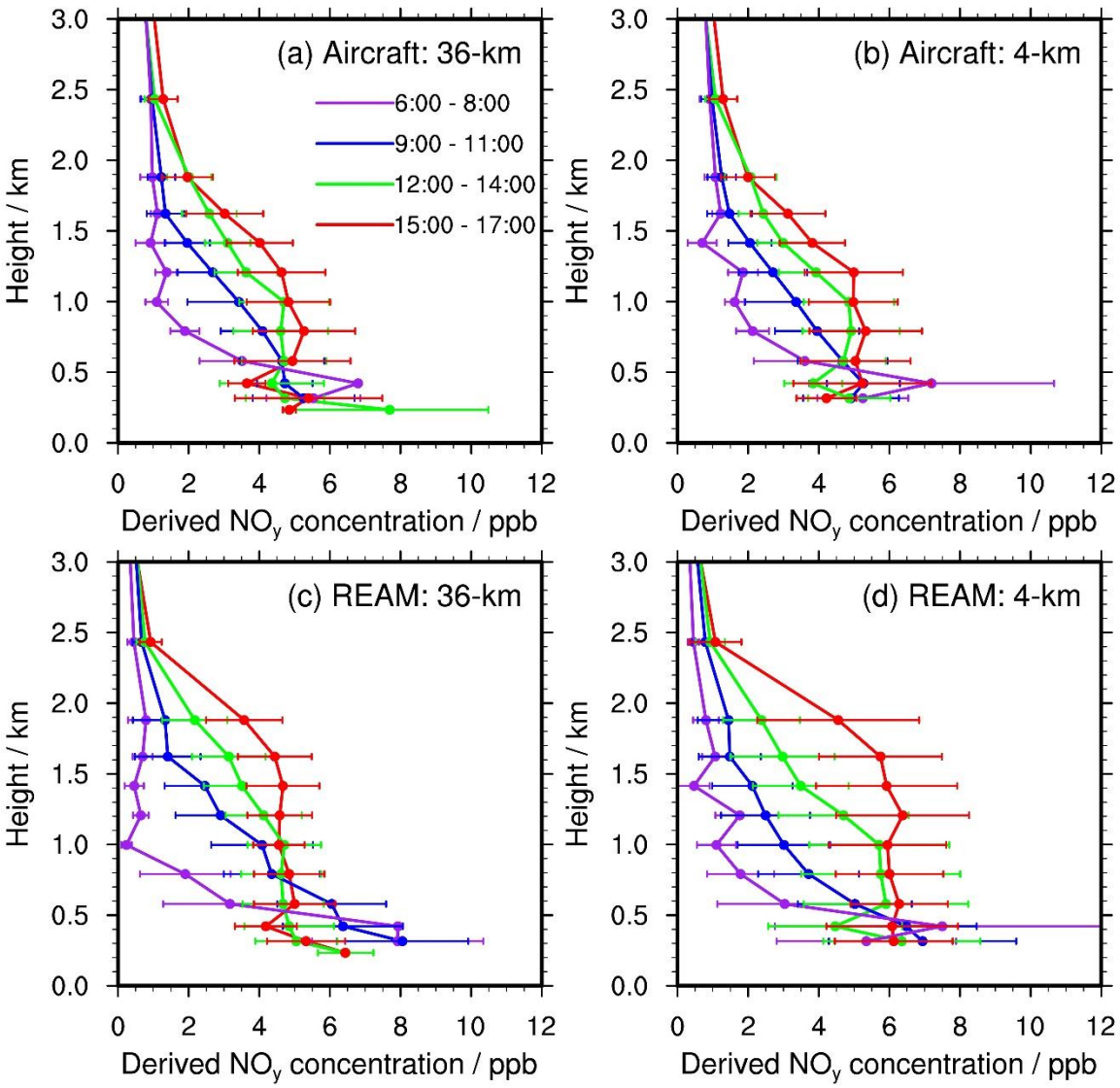

Figure S14. Temporal evolutions of derived-NO_y vertical profiles from the (a, b) P-3B aircraft and (c, d) REAM simulations at (a, c) 36-km and (b, d) 4-km resolutions during the DISCOVER-AQ campaign. Error bars denote the corresponding standard deviations. Due to the limited number of P-3B derived-NO_y observations and slightly different heights between 36- and 4-km grid cells from different WRF simulations (Table S2), small differences exist between the 36-km and 4-km observations when we bin them vertically to REAM grid cells (see also Table 1).

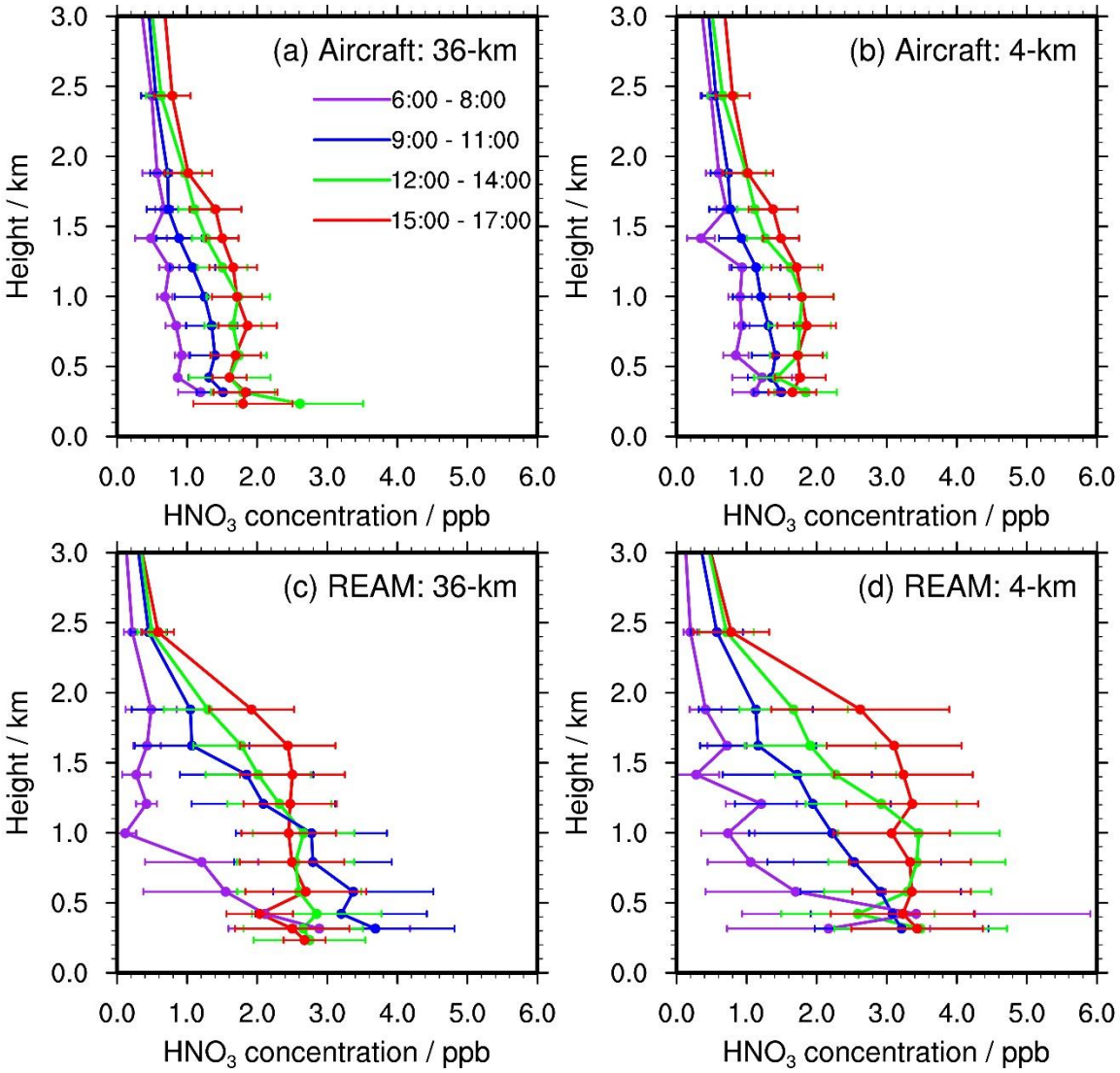

Figure S15. Same as Figure S14 but for coincident HNO_3 concentrations.

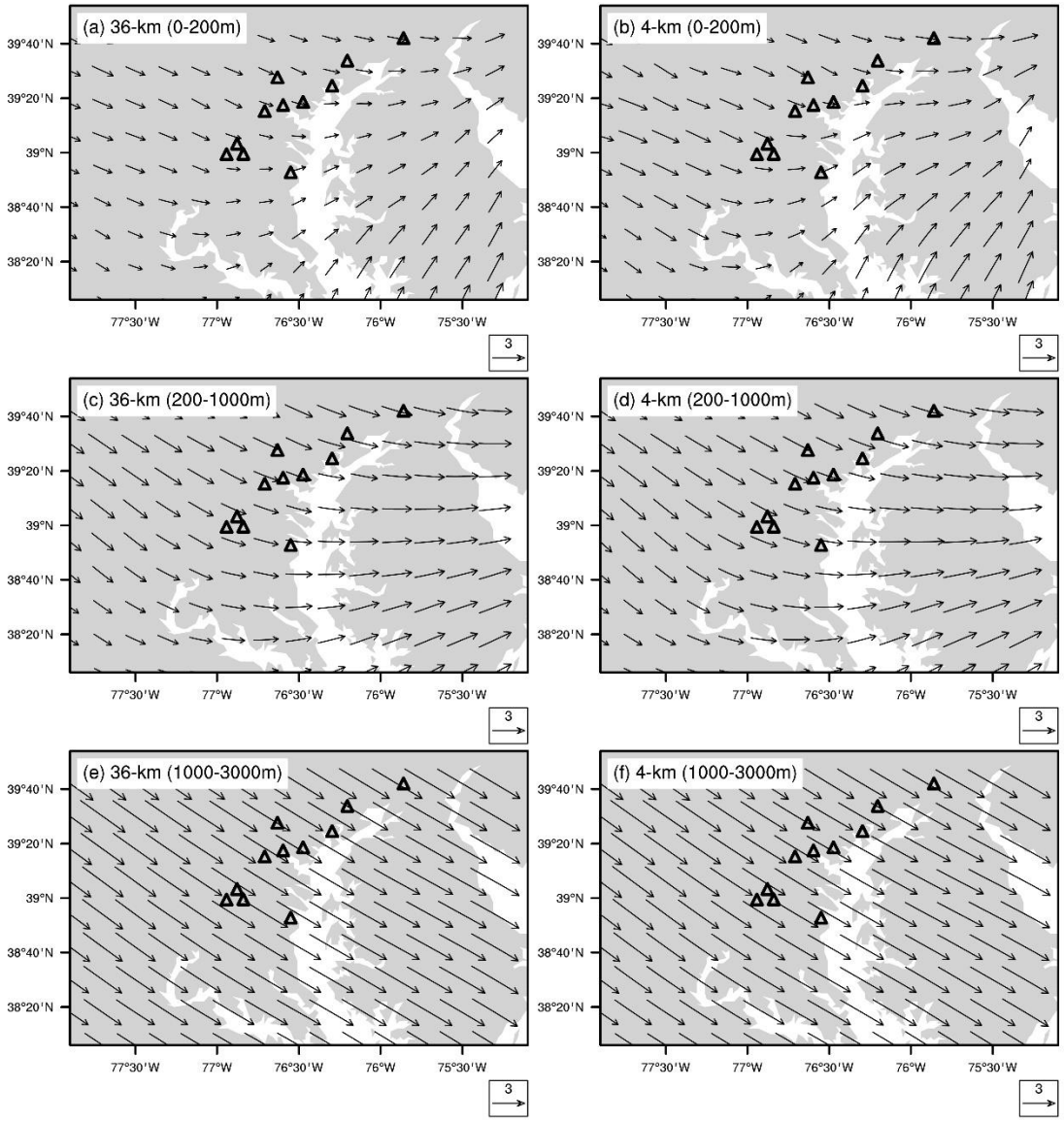

Figure S16. Comparisons of wind fields between the (a, c, e) 36-km and (b, d, f) nested 4-km WRF simulations for different height (AGL) bins in July 2011. (a) and (b) are for mean wind fields below about 200 m, (c) and (d) are for about 200 – 1000 m, and (e) and (f) are for about 1000 – 3000 m. Triangles denote the inland Pandora sites in Figure 1. The unit of wind speed is m s^{-1}.

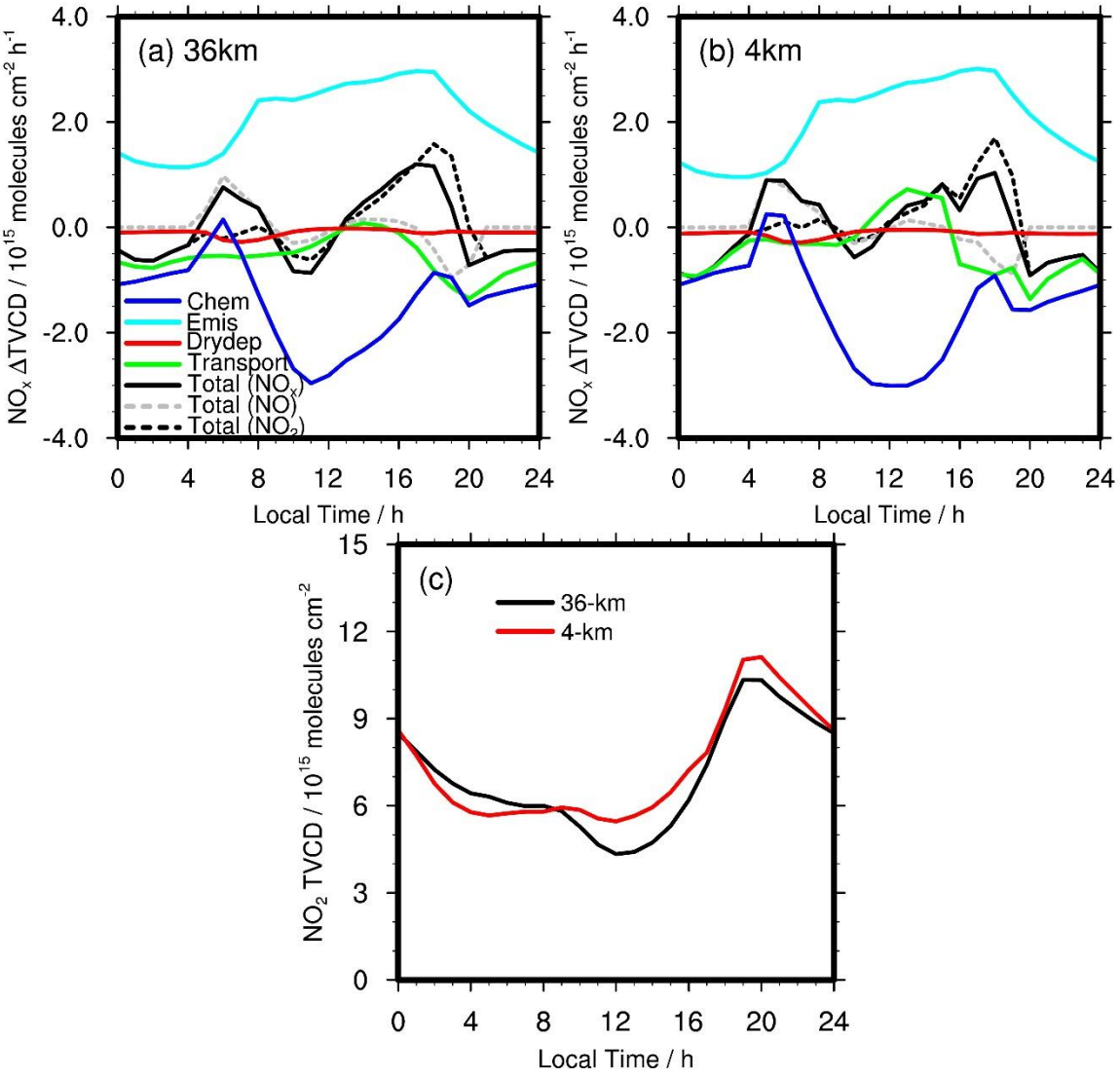

Figure S17. Contributions of emission, chemistry, transport, and dry deposition to NO_x TVCD diurnal variations over the six P-3B spiral sites (Figure 1 and Table S1) on weekdays in July 2011 for the (a) 36-km and (b) 4-km REAM simulations. "Chem" refers to net NO_x chemistry production; "Emis" refers to NO_x emissions; "Drydep" denotes NO_x dry depositions; "Transport" includes advection, turbulent mixing, lightning NO_x production, and wet deposition. "Total (NO_x)" is the hourly change of NO_x TVCDs ($\triangle(TVCD) = TVCD_{t+1} - TVCD_t$). "Total ($NO_2$)" is the hourly change of NO_2 TVCDs, and "Total (NO)" is the hourly change of NO TVCDs. (c), the 36-km and 4-km REAM simulated diurnal cycles of NO_2 TVCDs over the P-3B spiral sites on weekdays in July 2011. The black line in (c) denotes the 36-km REAM simulation results, and the red line denotes the 4-km REAM simulation results.

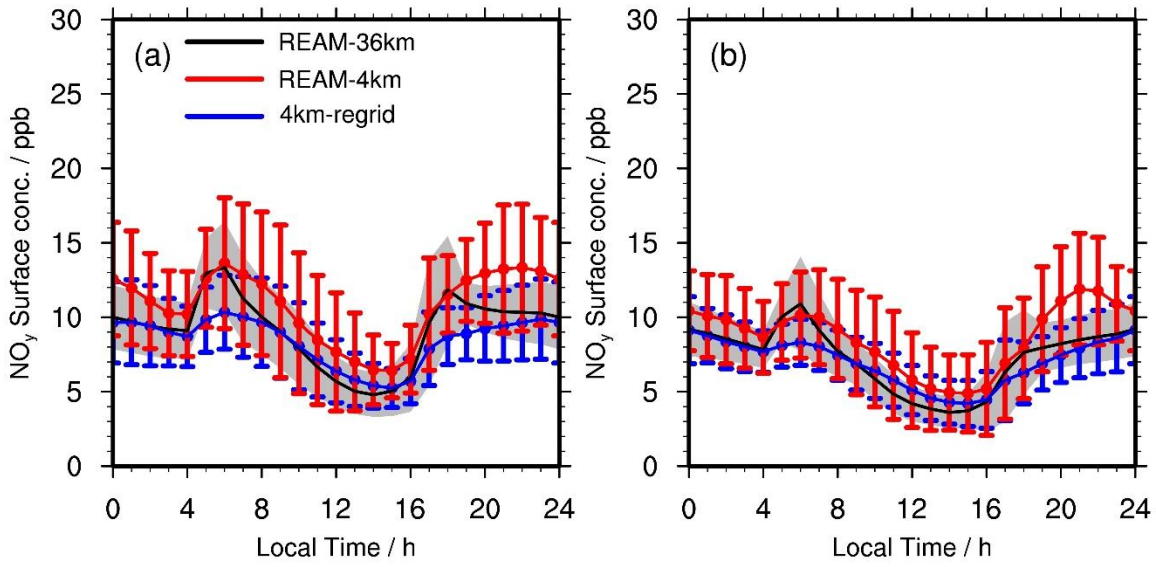

Figure S18. Comparisons of mean surface NO_y concentrations at Padonia, Edgewood, Beltsville, and Aldino between the 4-km and 36-km REAM simulations on (a) weekdays and (b) weekends for July 2011. "REAM-36km" (black lines) denotes the 36-km REAM simulation results; "REAM-4km" (red lines) denotes the 4-km REAM simulation results; "4km-regrid" refers to the 36-km values by re-gridding 4-km REAM simulation results into 36-km REAM grid cells. Error bars denote standard deviations.

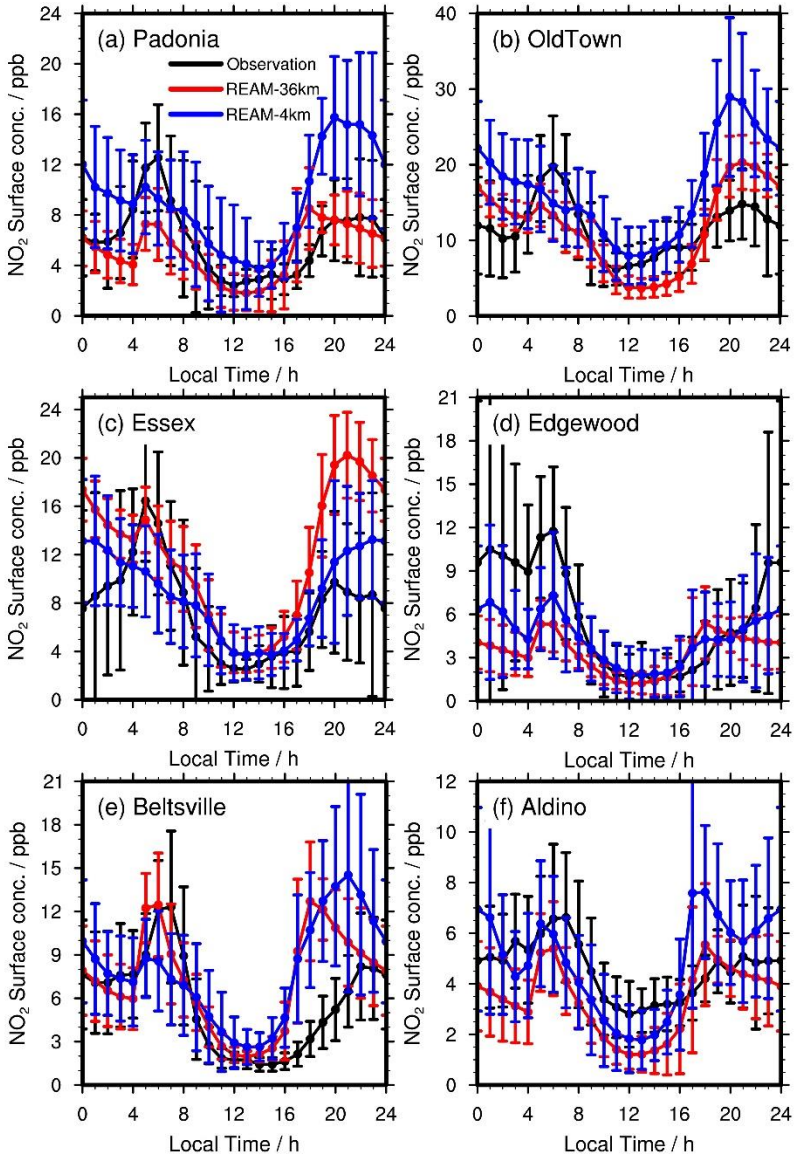

Figure S19. Same as Figure 7 but for individual observation sites on weekdays.

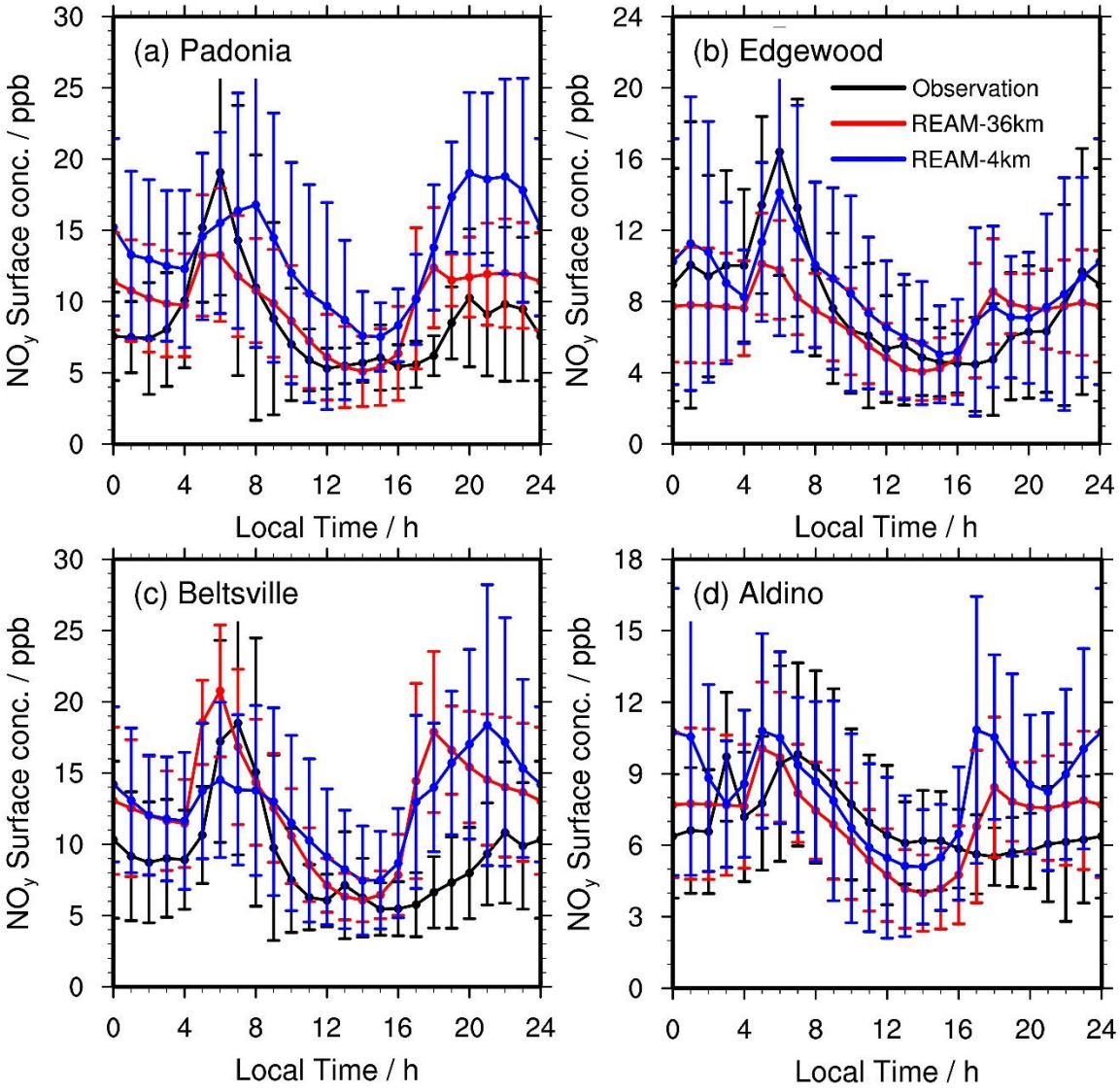

Figure S20. Same as Figure 12 but for individual observation sites on weekdays.

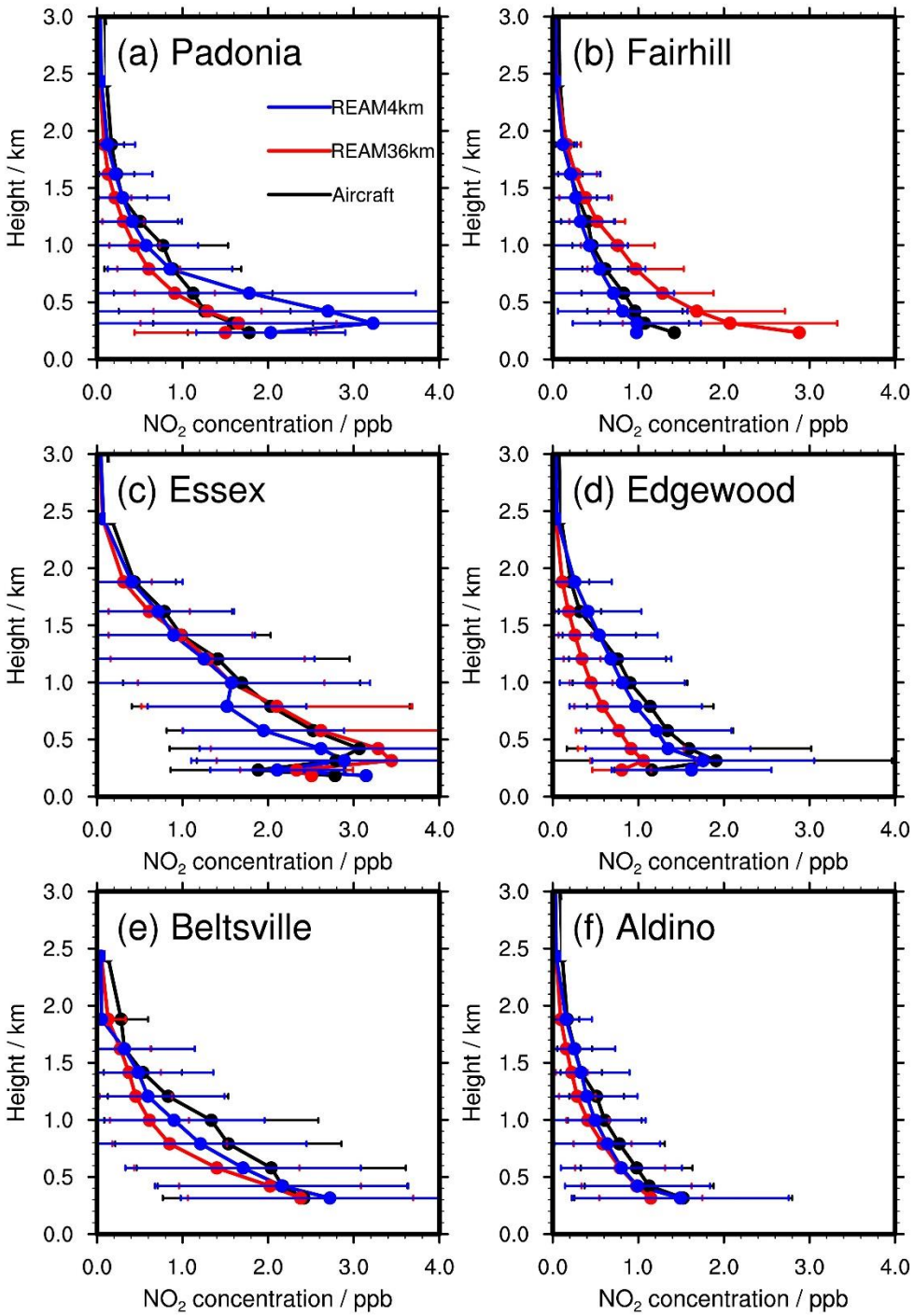

Figure S21. Comparison of NO_2 vertical profiles among P-3B aircraft observations and the 36-km and 4-km REAM simulations on weekdays in July 2011 for different spiral sites. Here we calculate the average of all available weekday NO_2 vertical profiles for each spiral site but do not consider the temporal evolutions shown in Figure 8.

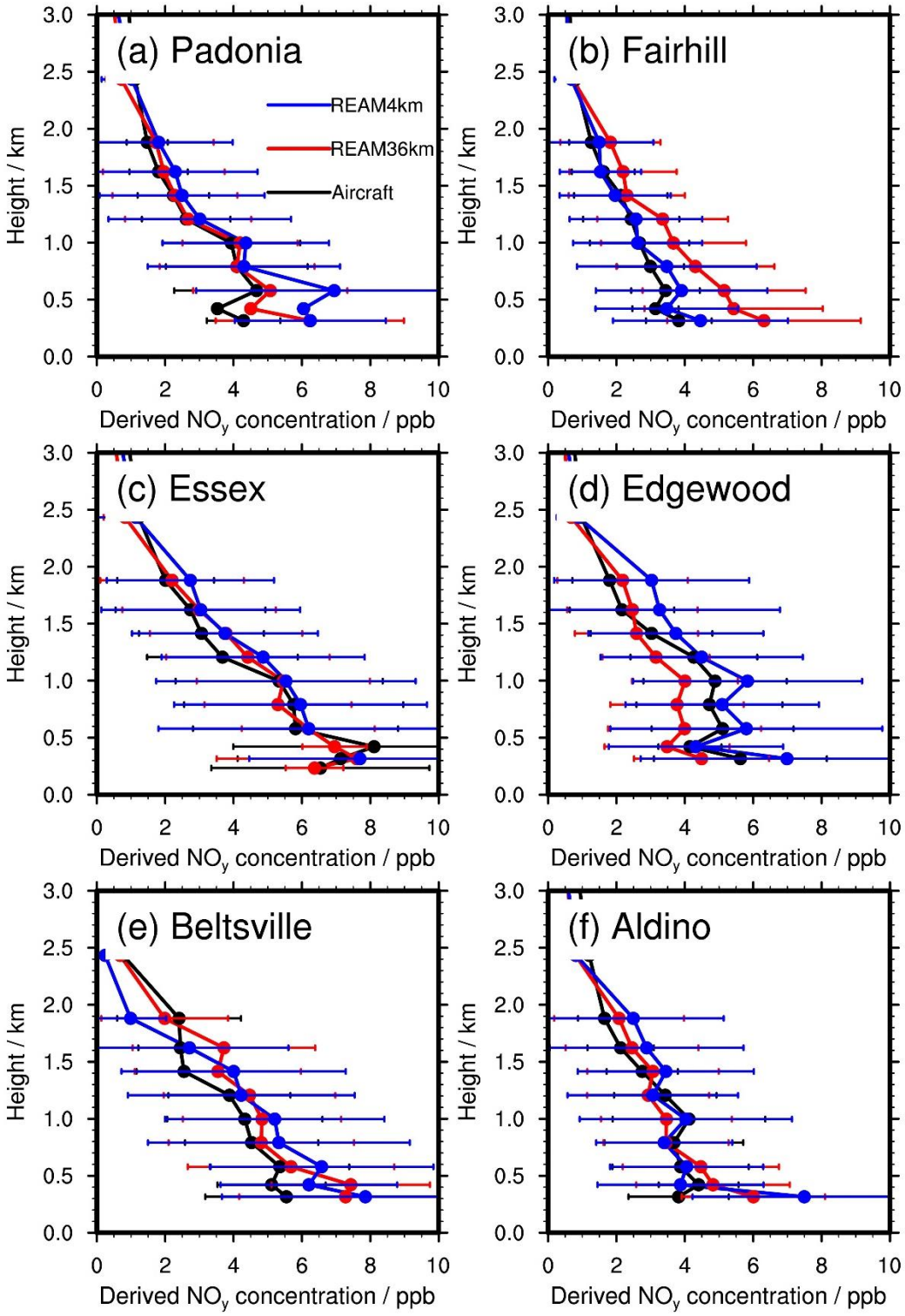

Figure S22. Same as Figure S21 but for derived-NO_y vertical profiles.

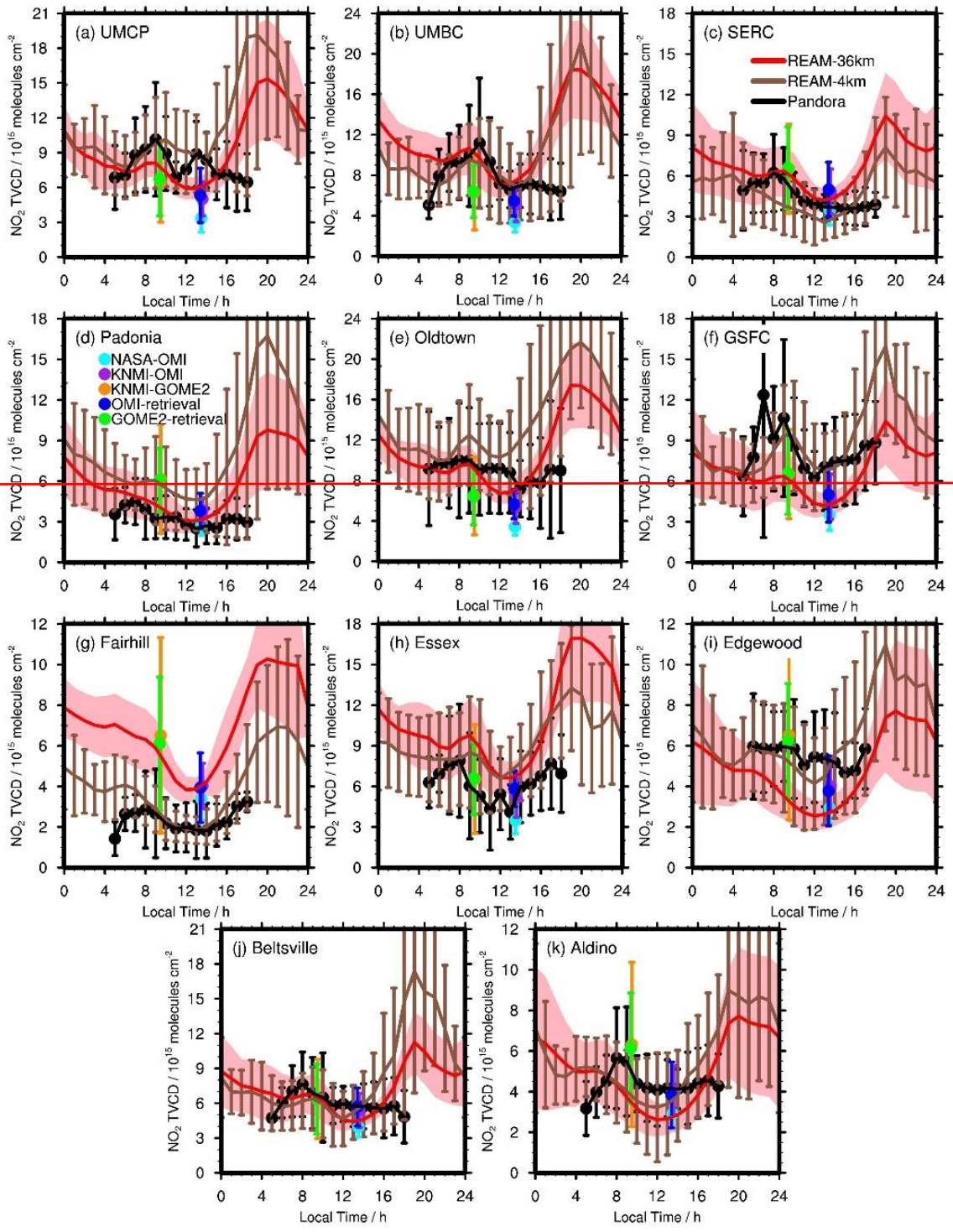
(a) UMCP
(b) UMBC
(c) SERC
REAM-36km
REAM-4km
Pandora
(d) Padonia
NASA-OMI
KNMI-OMI
KNMI-GOME2
OMI-retrieval
GOME2-retrieval
(e) Oldtown
(f) GSFC
(g) Fairhill
(h) Essex
(i) Edgewood
(j) Beltsville
(k) Aldino
NO2 TVCD / 10^15 molecules cm^-2
Local Time / h

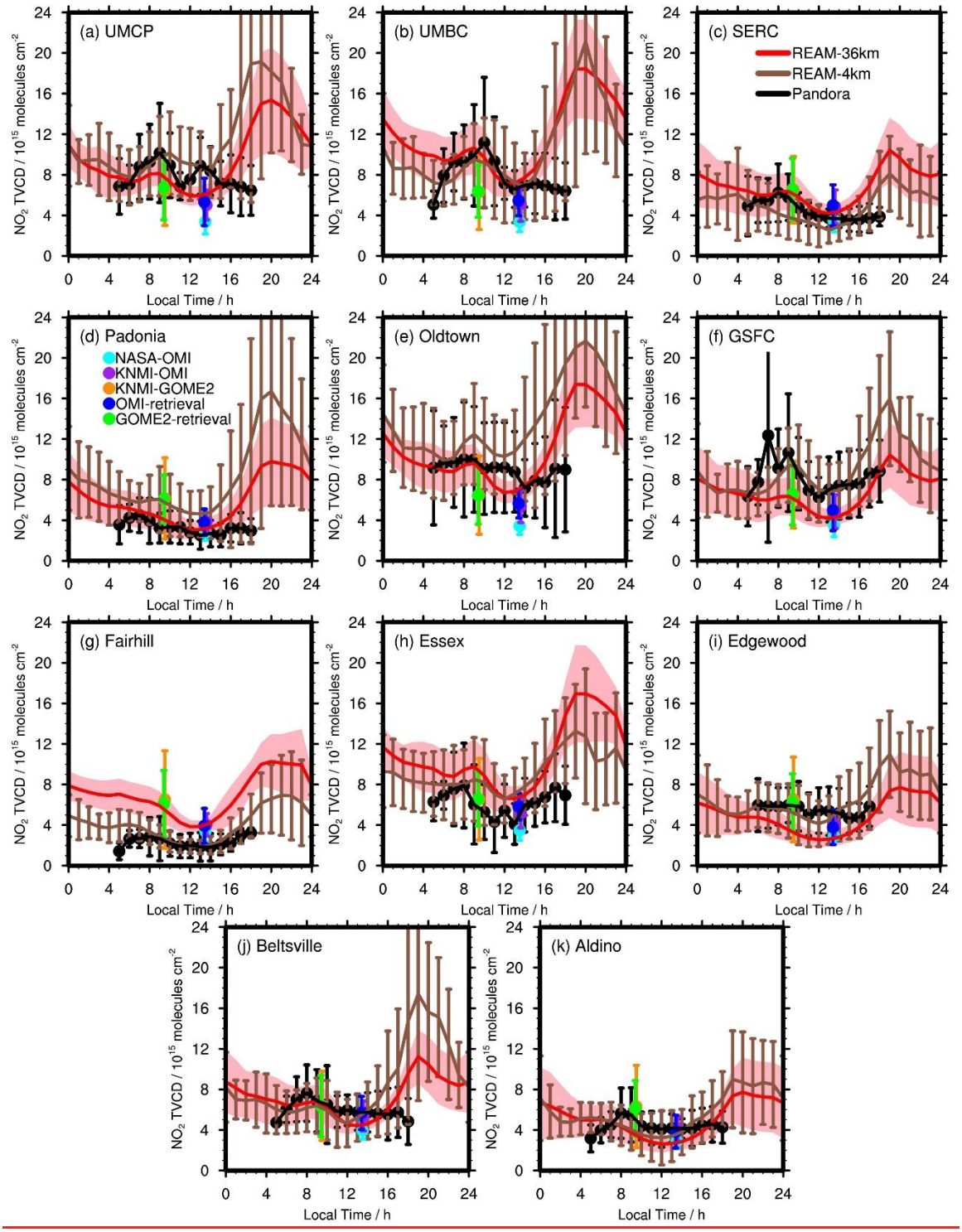

175

176 **Figure S23.** Same as Figure 10 but for individual Pandora sites on weekdays. Here we do not
177 include P-3B aircraft-derived NO_2 VCDs below 3.63 km.

178

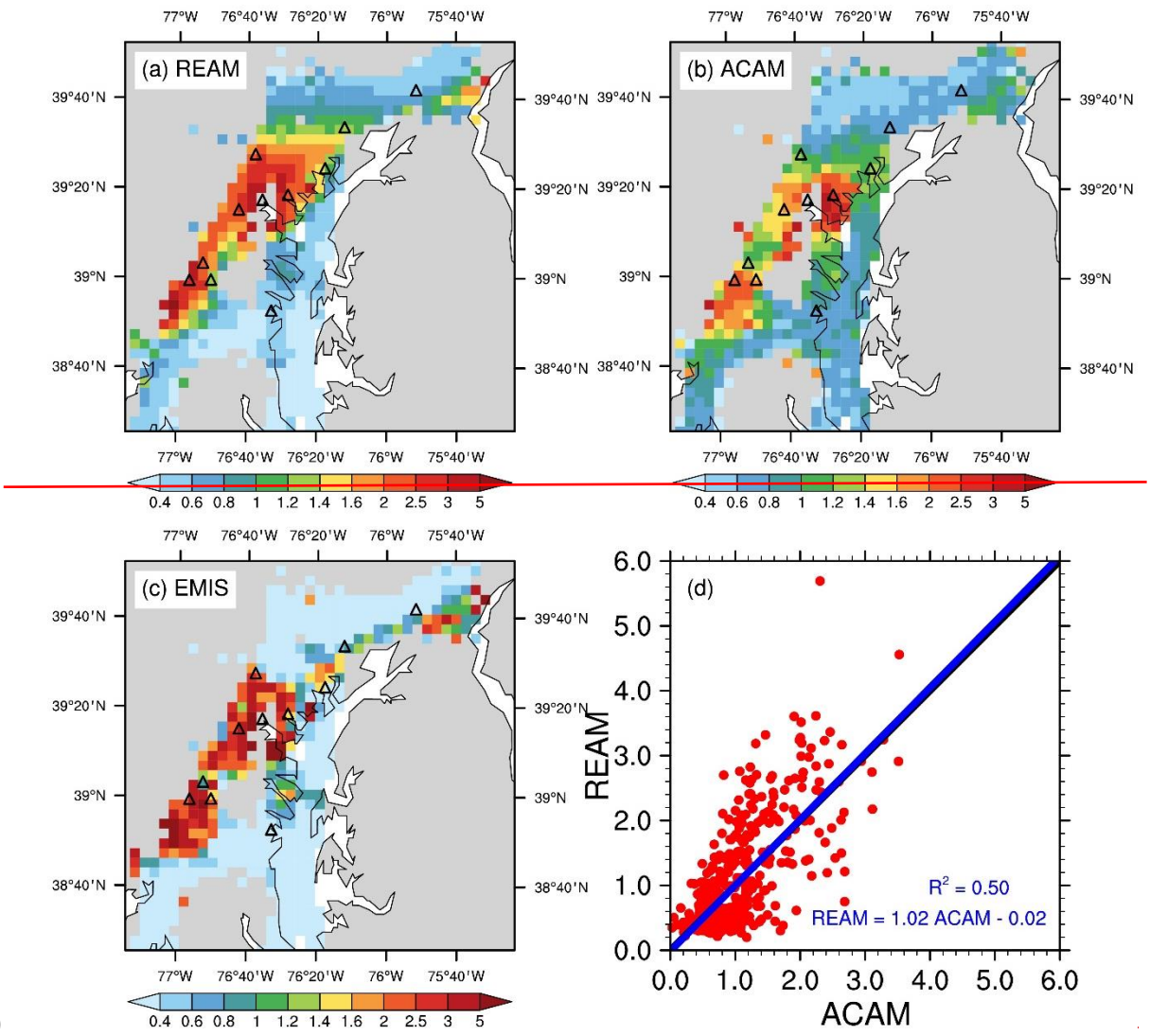
(a) REAM
(b) ACAM
(c) EMIS
(d)
77°W
76°40'W
76°20'W
76°W
75°40'W
39°40'N
39°20'N
39°N
38°40'N
0.4 0.6 0.8 1 1.2 1.4 1.6 2 2.5 3 5
REAM
ACAM
R² = 0.50
REAM = 1.02 ACAM - 0.02

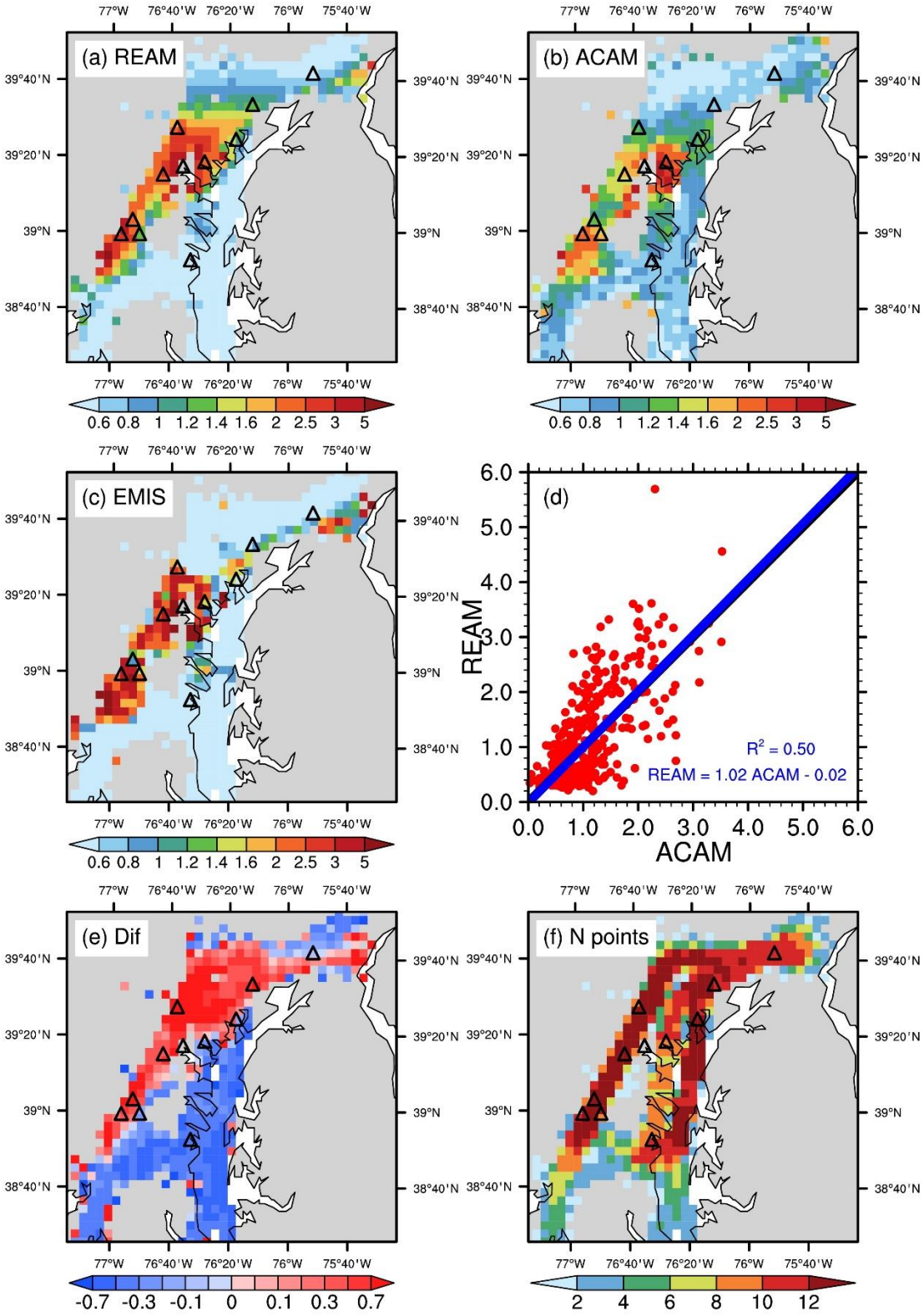

Figure S24. Same as Figure 14 but for weekends in July 2011. The domain averages of ACAM and coincident 4-km REAM NO_2 VCDs are 3.0 ± 1.7 and 3.3 ± 2.7 × 10^{15} molecules cm^{-2}, respectively.

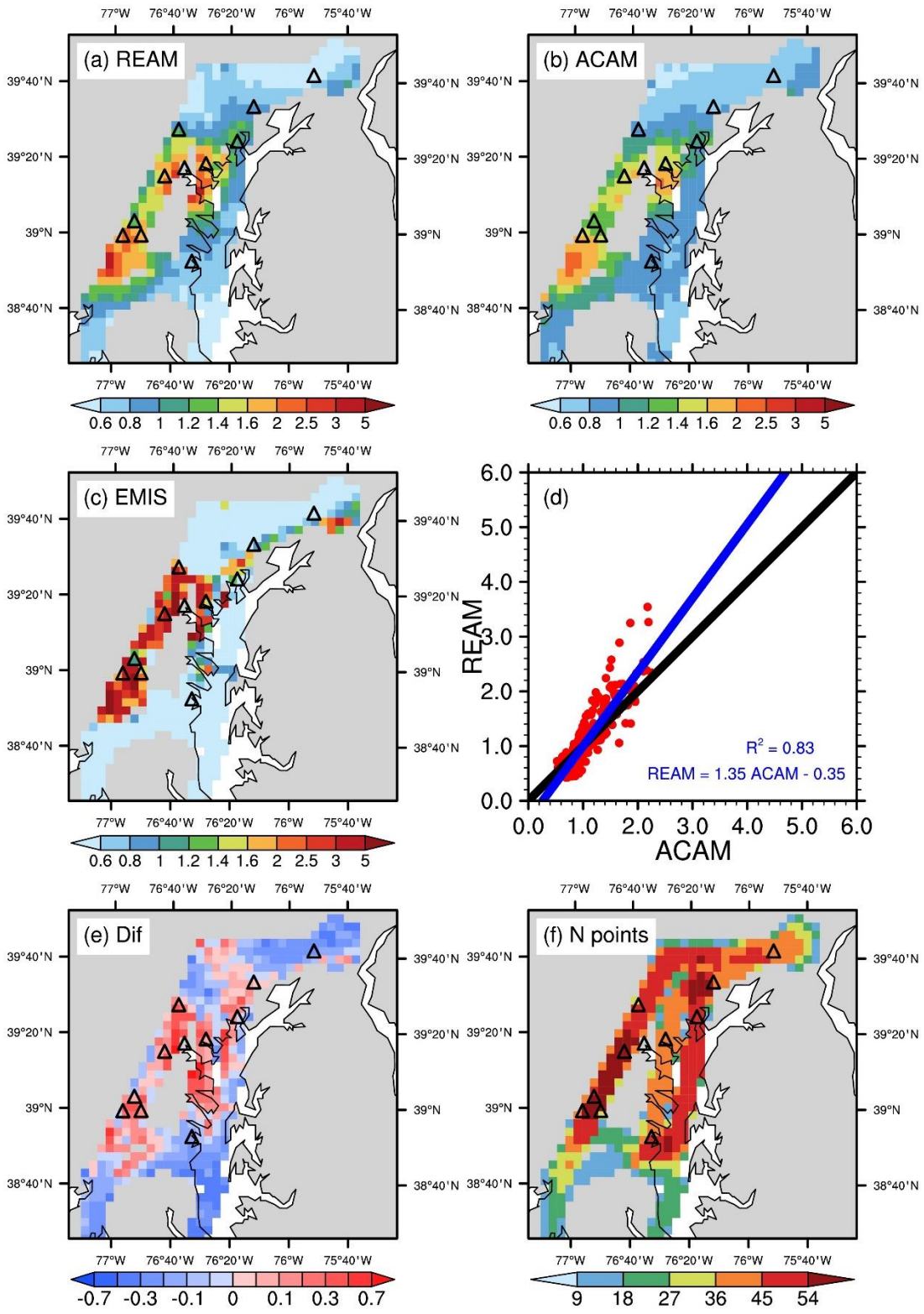

Figure S25. Same as Figure 14 but for grid cells with the number of data points ≥ 10, as shown in (f). The domain averages of ACAM and coincident 4-km REAM NO_2 VCDs are 5.3 ± 1.8 and 4.6 ± 2.4 × 10^{15} molecules cm^{-2}, respectively.

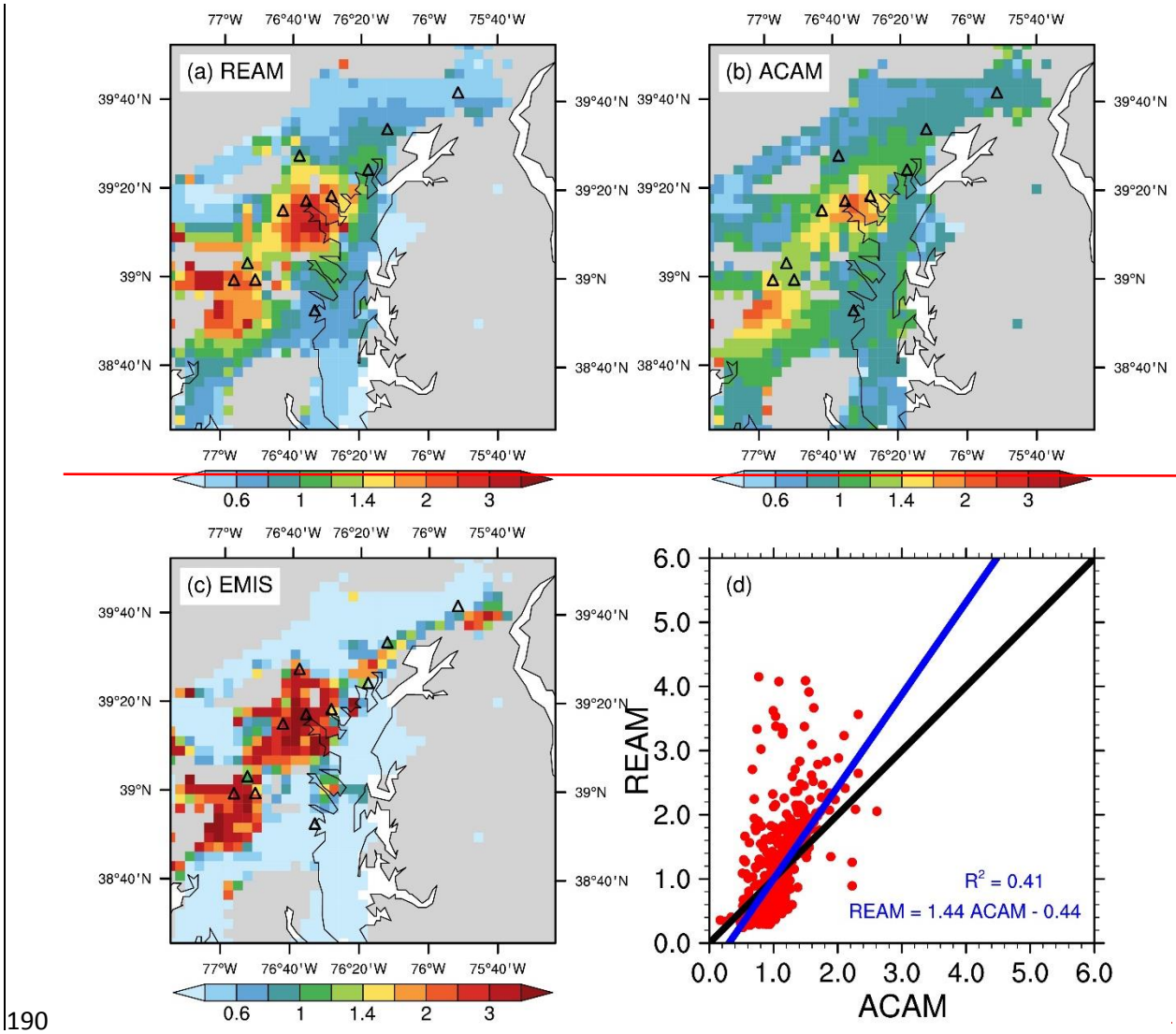
(a) REAM
(b) ACAM
(c) EMIS
(d)
77°W
76°40'W
76°20'W
76°W
75°40'W
39°40'N
39°20'N
39°N
38°40'N
0.6
1
1.4
2
3
REAM
ACAM
R^2 = 0.41
REAM = 1.44 ACAM - 0.44
0.0
1.0
2.0
3.0
4.0
5.0
6.0

190

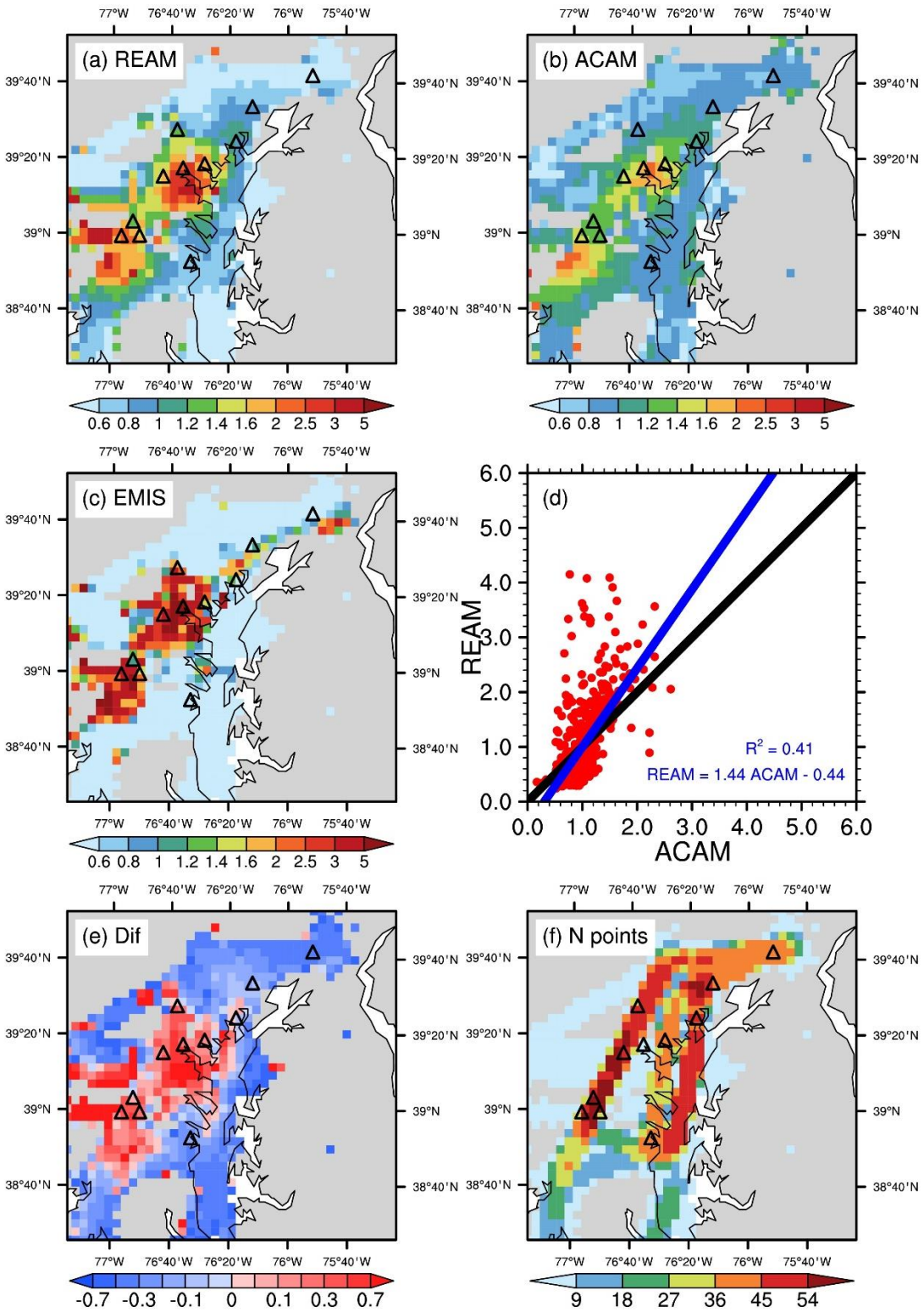

Figure S2~~65~~. Same as Figure 14 but for weekday ACAM datasets obtained from https://www-air.larc.nasa.gov/cgi-bin/ArcView/discover-aq.dc-2011?UC12=1#LIU.XIONG/ (last access: December 31, 2019). The domain averages of ACAM and coincident 4-km REAM NO_2 VCDs are 5.9 ± 1.8 and 4.6 ± 3.1 × 10^{15} molecules cm^{-2}, respectively.

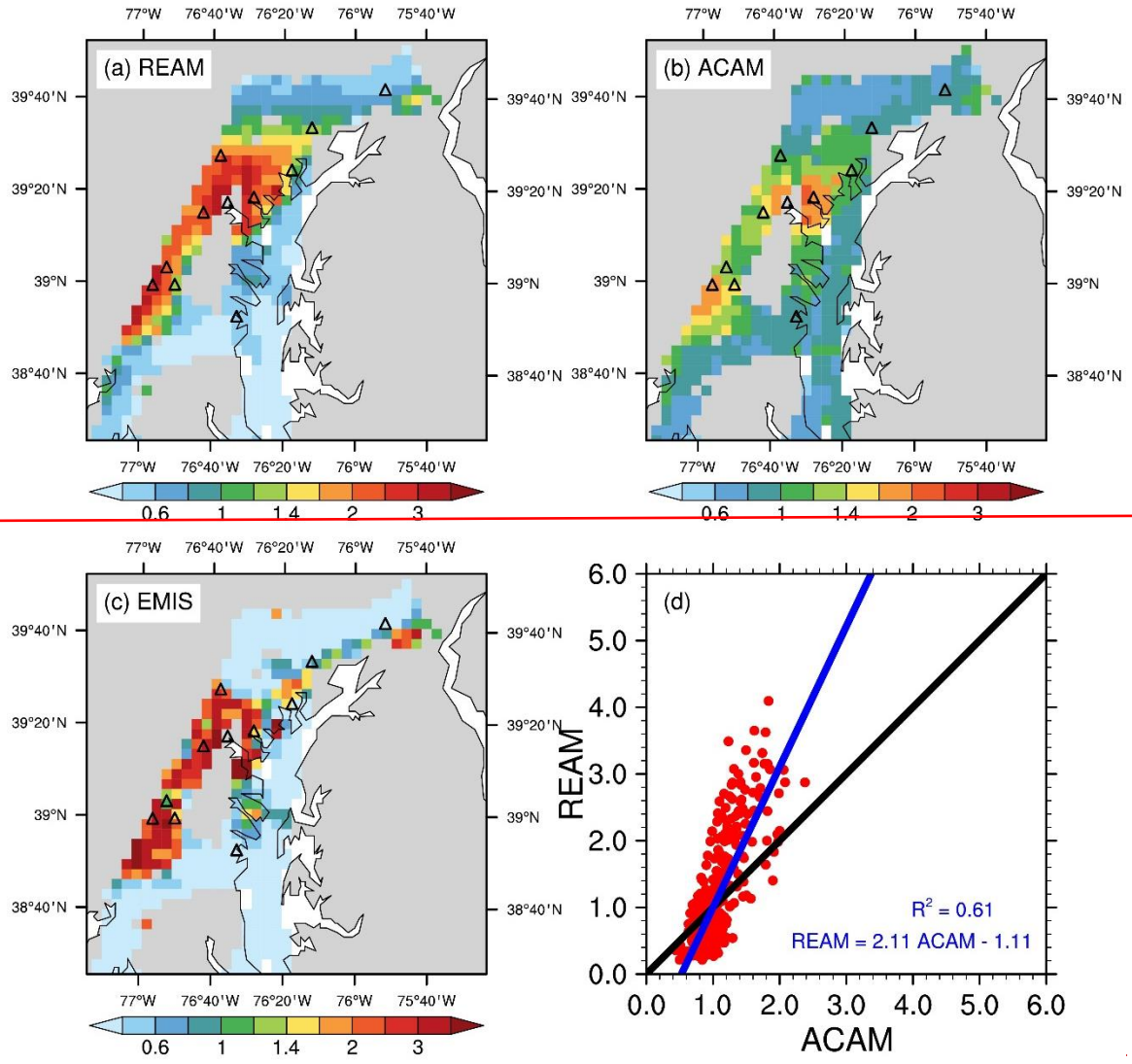
(a) REAM
(b) ACAM
(c) EMIS
(d)
77°W
76°40'W
76°20'W
76°W
75°40'W
39°40'N
39°20'N
39°N
38°40'N
0.6
1
1.4
2
3
REAM
ACAM
R^2 = 0.61
REAM = 2.11 ACAM - 1.11
0.0
1.0
2.0
3.0
4.0
5.0
6.0

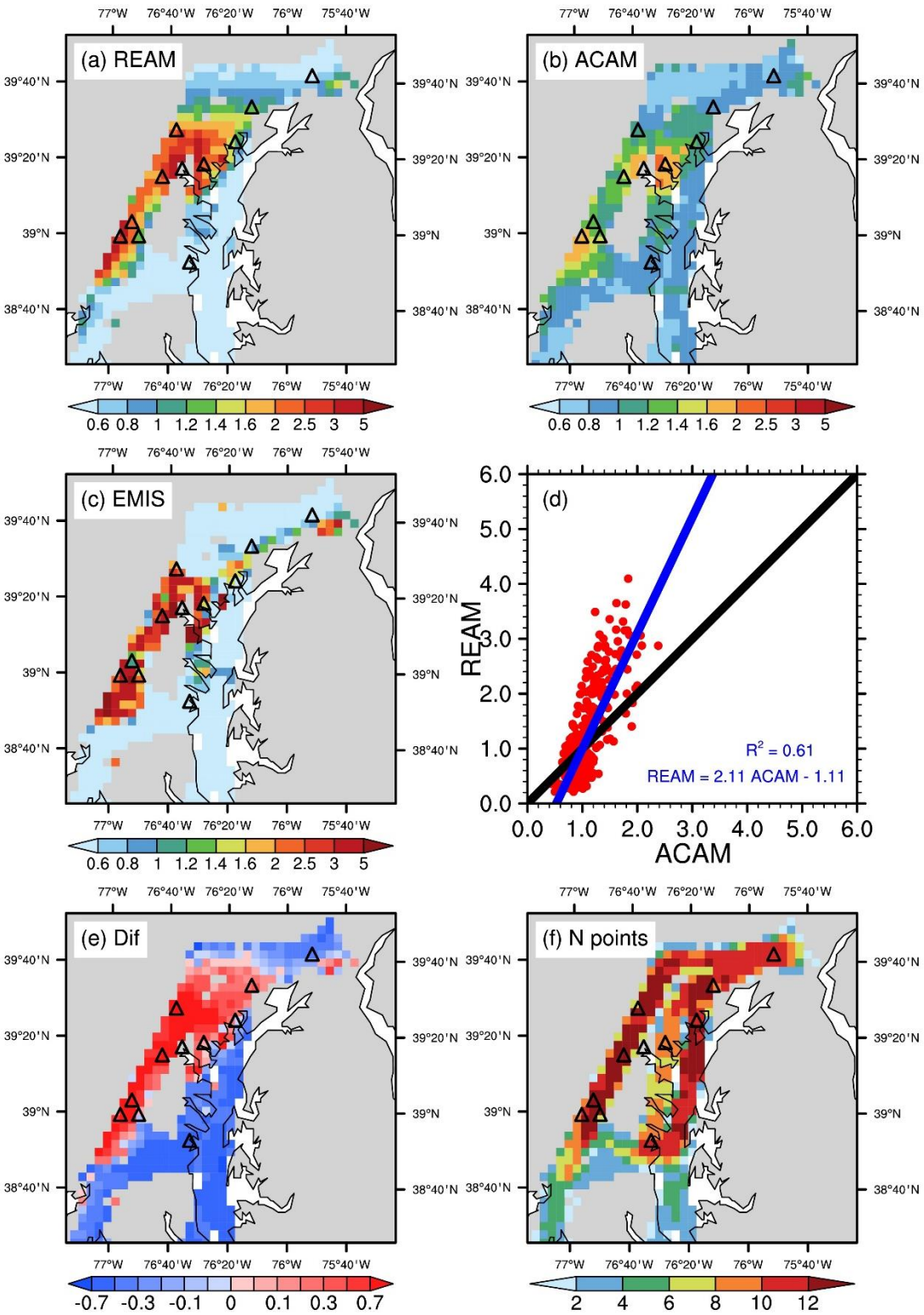

Figure S2~~6~~7. Same as Figure S2~~5~~6 but for weekend ACAM datasets obtained from https://www-air.larc.nasa.gov/cgi-bin/ArcView/discover-aq.dc-2011?UC12=1#LIU.XIONG/ (last access: December 31, 2019). The domain averages of ACAM and coincident 4-km REAM NO_2 VCDs are 4.7 ± 1.4 and 3.4 ± 2.7 × 10^{15} molecules cm^{-2}, respectively.

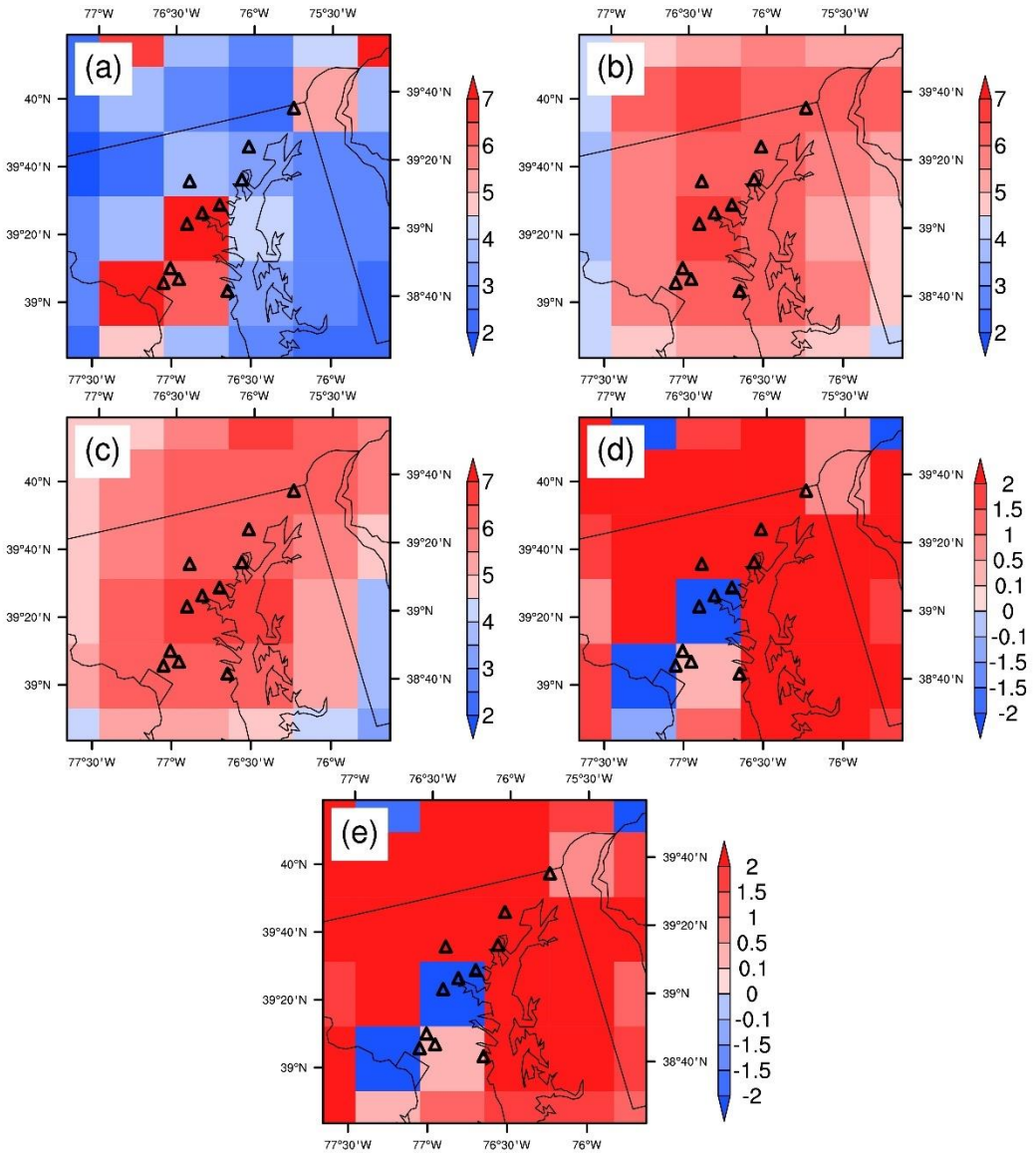

Figure S2~~8~~7. Distributions of weekday NO_2 TVCDs around the DISCOVER-AQ 2011 region for 9:30 LT in July 2011: (a) the 36-km REAM simulation results, (b) the KNMI GOME-2A product, (c) for the retrieved GOME-2A NO_2 TVCDs by using the KNMI DOMINO algorithm with corresponding 36-km REAM vertical profiles, (d) distribution of the NO_2 TVCD differences (b minus a) between KNMI GOME-2A and 36-km REAM, and (e) the difference (c minus a) between retrieved GOME-2A NO_2 TVCDs and the 36-km REAM results. The NO_2 TVCD unit is 10^{15} molecules cm^{-2}.

Supporting tables for

Comprehensive evaluations of diurnal NO_2 measurements during DISCOVER-AQ 2011: Effects of resolution dependent representation of NO_x emissions

Jianfeng Li[1, a], Yuhang Wang[1*], Ruixiong Zhang[1], Charles Smeltzer[1], Andrew Weinheimer[2], Jay Herman[3], K. Folkert Boersma[4, 5], Edward A. Celarier[6, 7, b], Russell W. Long[8], James J. Szykman[8], Ruben Delgado[3], Anne M. Thompson[6], Travis N. Knepp[9, 10], Lok N Lamsal[6], Scott J Janz[6], Matthew G Kowalewski[6], Xiong Liu[11], Caroline R. Nowlan[11]

[1]School of Earth and Atmospheric Sciences, Georgia Institute of Technology, Atlanta, Georgia, USA
[2]National Center for Atmospheric Research, Boulder, Colorado, USA
[3]University of Maryland Baltimore County JCET, Baltimore, Maryland, USA
[4]Royal Netherlands Meteorological Institute, De Bilt, the Netherlands
[5]Wageningen University, Meteorology and Air Quality Group, Wageningen, the Netherlands
[6]NASA Goddard Space Flight Center, Greenbelt, Maryland, USA
[7]Universities Space Research Association, Columbia, Maryland, USA
[8]National Exposure Research Laboratory, Office of Research and Development, U.S. Environmental Protection Agency, Research Triangle Park, NC, USA
[9]NASA Langley Research Center, Virginia, USA
[10]Science Systems and Applications, Inc., Hampton, Virginia, USA
[11]Harvard-Smithsonian Center for Astrophysics, Cambridge, Massachusetts, USA

[a]now at: Atmospheric Sciences and Global Change Division, Pacific Northwest National Laboratory, Richland, Washington, USA
[b]now at: Digital Spec, Tyson's Corner, VA, USA

[*] *Correspondence to* Yuhang Wang (yuhang.wang@eas.gatech.edu)

Table S1. Summary of information for the 11 inland Pandora sites in the DISCOVER-AQ campaign

Site #	Site name	Latitude / ° N	Longitude / ° W	Land type	NO_x emission in 36-km REAM[1] / 10^{21} molecules km^{-2} s^{-1}	NO_x emission in 4-km REAM / 10^{21} molecules km^{-2} s^{-1}	Availability of P-3B aircraft observations[2]	Availability of surface NO_y	Availability of surface NO_2
1	UMCP	38.991	76.943	urban	10.9	19.5			
2	UMBC	39.255	76.709	urban	12.9	14.8			
3	SERC	38.880	76.550	rural/coastal	5.0	0.8			
4	Padonia	39.461	76.631	suburban	2.9	12.8	Y	Y	Y
5	Oldtown	39.291	76.596	urban	12.9	33.0			Y
6	GSFC	38.993	76.840	urban/suburban	5.0	6.2			
7	Fairhill	39.701	75.860	rural	6.6	0.6	Y		
8	Essex	39.311	76.474	coastal/urban	12.9	6.4	Y		Y
9	Edgewood	39.410	76.297	coastal/urban	1.7	1.3	Y	Y	Y
10	Beltsville	39.055	76.878	suburban	5.0	4.4	Y	Y	Y
11	Aldino	39.563	76.204	rural/suburban	1.7	4.2	Y	Y	Y

[1] Here, NO_x emissions refer to the mean values in one week (Monday – Sunday). Since we scale weekend emissions based on weekday emissions in this study, the relative differences among different sites and between the 36-km REAM and the 4-km REAM are the same for weekdays and weekends.

[2] "Y" denotes that P-3B aircraft observations were available at the corresponding site during the DISCOVER-AQ campaign. And blank indicates that no aircraft observations were available. Similar to the "availability of surface NO_y" and the "availability of surface NO_2."

Table S2. Setup of the 36-km and nested 4-km WRF simulations

	36-km WRF	Nested 4-km WRF
Horizontal resolution	36 km	Nested (36 km, 12 km, 4 km)
Domain center	40° N, 97° W	38.94° N, 75.76° W
Microphysics	WRF Single-Moment 6-class scheme (WSM6)	Same as 36-km WRF
Surface layer	Revised MM5 Monin-Obukhov scheme	Same as 36-km WRF
Land surface	Unified Noah land-surface model	Same as 36-km WRF
Longwave radiation	RRTM scheme	Same as 36-km WRF
Shortwave radiation	Dudhia scheme	Same as 36-km WRF
Planetary boundary layer	Yonsei University (YSU) scheme	Same as 36-km WRF
Cumulus parameterization	Kain-Fritsch (new Eta) scheme	Kain-Fritsch scheme for outer domains (36-km and 12-km); no cumulus parameterization for the 4-km domain
Urban surface	3-category urban canopy model	Same as 36-km WRF

Table S3. Comparison of NO_2 TVCDs among different simulations and datasets during the DISCOVER-AQ campaign for 9:30 and 13:30 LT on weekdays and weekends

	Weekday		Weekend	
	9:30 LT[1]	13:30 LT	9:30 LT	13:30 LT
REAM-36km[2]	6.5 ± 1.1[3]	4.9 ± 0.6	4.7 ± 0.7	3.6 ± 0.6
REAM-4km	7.0 ± 1.9	6.3 ± 2.0	5.3 ± 1.6	4.3 ± 1.5
Pandora	6.5±1.8	5.3±1.0	4.9±0.9	3.7±0.5
Flight	5.3	5.0	4.5	3.2
KNMI-GOME2	6.3 ± 3.4		5.3 ± 1.4	
GOME2-retrieval	6.3 ± 2.5		4.1 ± 1.9	
NASA-OMI		3.3 ± 0.8		2.9 ± 0.6
KNMI-OMI		4.6 ± 1.3		3.2 ± 0.7
OMI-retrieval		4.7 ± 1.4		3.2 ± 0.7

[1] For REAM simulations, we use the average of NO_2 TVCDs at 9:00 and 10:00 LT to represent the value at 9:30 LT, similar to those at 13:30 LT.
[2] The dataset names have the same meaning as Figure 10, and the NO_2 TVCD values are the same as those shown in Figure 10.
[3] The unit is 10^{15} molecules cm^{-2}.